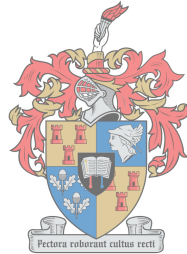


Surrogate Modelling of Performance Metrics of a Wideband Feed for the SKA Reflector Antenna

by

Ridalise Louw



UNIVERSITEIT
iYUNIVESITHI
STELLENBOSCH
UNIVERSITY

*Thesis presented in partial fulfilment of the requirements for
the degree of Master of Engineering (Electronic) in the
Faculty of Engineering at Stellenbosch University*

1918 - 2018

Supervisor: Prof. D.I.L. De Villiers

March 2018

The financial assistance of the National Research Foundation (NRF) towards this research is hereby acknowledged. Opinions expressed and conclusions arrived at, are those of the author and are not necessarily to be attributed to the NRF.

Declaration

By submitting this thesis electronically, I declare that the entirety of the work contained therein is my own, original work, that I am the sole author thereof (save to the extent explicitly otherwise stated), that reproduction and publication thereof by Stellenbosch University will not infringe any third party rights and that I have not previously in its entirety or in part submitted it for obtaining any qualification.

Date: March 2018

Copyright © 2018 Stellenbosch University
All rights reserved.

Abstract

Surrogate Modelling of Performance Metrics of a Wideband Feed for the SKA Reflector Antenna

R. Louw

*Department of Electrical and Electronic Engineering,
University of Stellenbosch,
Private Bag X1, Matieland 7602, South Africa.*

Thesis: MEng (EE)

December 2017

The focus of this thesis is on a design methodology for a pyramidal sinuous antenna for use as a wideband feed in the SKA reflector antenna system. The design objective is to maximise the receiving sensitivity of the feed, while maintaining a reflection coefficient of at most -10 dB over the entire band.

Acquiring accurate solutions of the antenna's performance metrics for each geometric variation in the design space requires a full wave solution for each possibility. This is a time consuming task. Thus, the focus in this thesis is on finding accurate surrogate models that are fast to evaluate, on which the design can be done. Surrogate models require the availability of a coarse model that is less accurate, but faster to evaluate than the fine model. Truncated models of the antenna structure that operate at the band edges of the full fine model are used. These provide a good approximation of the behaviour of the pyramidal sinuous antenna. A simple surrogate model is suggested for the sensitivity of the system, which makes use of an output space mapping technique where a second-order polynomial regression term is applied to the difference between the sensitivity of the coarse and fine models, using only a few fine model evaluations.

A rational interpolation model is used to find the input impedance of the antenna from which the reflection coefficient is calculated. Rational interpolation of high-fidelity data, acquired from the fine model, is done first. Low-fidelity data, acquired from the coarse model, are subsequently added to the rational interpolant so as to improve the accuracy of the model without the need for

adding additional high-fidelity data points. The constraint which ensures a pole-free rational interpolant restricts the solution of the model. This leads to the introduction of a blended rational interpolation method that locally models the trend of the low-fidelity data and is then blended together into a global interpolant using quadratic B-spline functions. A comparison of this model to other interpolation methods shows this blended rational interpolant to perform well.

Brief consideration is given to the application of these surrogate modelling methods on a 5:1 bandwidth pyramidal sinuous antenna. This example illustrates the significant speed-up that is achieved for the design, where a speed-up factor close to 16 is achieved.

The design of a 3:1 bandwidth is then considered with two geometric parameters as input to the design. Using very few high-fidelity data points, the blended rational interpolation method leads to a predicted region of where the reflection coefficient is less than -10 dB that has an 11.9% error. From this region, the antenna with the maximum sensitivity is identified, with the surrogate predicting an average sensitivity of $3.651 \text{ m}^2/\text{K}$. Validation of the results shows the average sensitivity to be equal to $3.7139 \text{ m}^2/\text{K}$ and a reflection coefficient below -10.52 dB over the entire band.

Opsomming

Surrogaat-Modellering van die Werksverrigtingsmaatstawwe van 'n Wyeband Voer vir die SKA Weerkaatsingsantenna

("Surrogate Modelling of Performance Metrics of a Wideband Feed for the SKA Reflector Antenna")

R. Louw

*Departement Elektries en Elektroniese Ingenieurswese,
Universiteit van Stellenbosch,
Privaatsak X1, Matieland 7602, Suid Afrika.*

Tesis: MIng (EE)

Desember 2017

Die fokus in hierdie tesis is op die ontwerp van 'n piramidiese siniese antenna vir gebruik as 'n wyeband voer in die SKA weerkaatsingsantenna. Die mikpunt vir die ontwerp is om die ontvangersensitiwiteit van die voer te maksimeer, terwyl daar gelyktydig aan 'n maksimum weerkaatskoëffisiënt van -10 dB oor die hele band voldoen word.

Om akkurate oplossings van die antenna se werksverrigtingsmaatstawwe vir elke geometriese variasie in die ontwerpsteruimte te bekom, word volgorde simulaties vir elke moontlikheid verlang. Hierdie is 'n tydrowende proses. Daarom fokus hierdie tesis daarop om akkurate surrogaatmodelle te bou wat vinnig is om te evalueer en waarop die ontwerp dan gedoen kan word. Surrogaatmodelle verlang die beskikbaarheid van 'n growwe model wat minder akkuraat is as die fyn model, maar wat vinnig is om te evalueer. Aangesnyde modelle van die antenna struktuur wat werkend is op die rante van die frekwensiebande van die volle fyn model word gebruik. Hierdie modelle gee 'n goeie afskatting van die gedrag van die piramidiese siniese antenna. 'n Eenvoudige surrogaatmodel word voorgestel vir die sensitiwiteit van die stelsel, wat gebruik maak van 'n afvoerruimtekartering tegniek waar 'n tweede-orde polinomiese regressieterm verkry is op die verskil tussen die sensitiwiteit van die growwe en fyn modelle, deur van net 'n paar fyn model evaluasies gebruik te maak.

A rasionele interpolasie model word gebruik om die intree impedansie van die antenna te vind, waarvan die weerkaatskoëffisiënt bereken word. Eerste word rasionele interpolasie van hoë-getrouheid data wat van die fyn model afkomsitg is gedoen. Dan word laë-getrouheid data by die interpolant gevoeg sodat die akkuraatheid van die model verbeter word sonder om addisionele hoë-getrouheid datapunte by te voeg. Die beperking wat toegepas word om te verseker dat die model nie pole bevat nie, perk die oplossing van die model in. Dit lei na die bekendstelling van 'n gemengde rasionele interpolasie metode wat plaaslik die tendens van die laë-getrouheid data modelleer en dan saam-gemeng word in 'n globale interpolant deur middel van kwadratiese B-spline funksies. 'n Vergelyking van hierdie model met ander interpolasiemetodes wys dat hierdie gemengde rasionele interpolant goed werk.

Die aanwending van hierdie surrogaatmodelle op 'n 5:1 bandwydte piramiediese siniese antenna word kortliks oorweeg. Hierdie voorbeeld illustreer die merkwaardige versnelling wat verkry word vir die ontwerp, met 'n tydsbesparingsfaktor naby aan 16.

Die ontwerp van 'n 3:1 bandwydte piramiede siniese antenna word oorweeg met twee geometriese parameters as intreë tot die ontwerp. Deur van net 'n paar hoë-getrouheid datapunte gebruik te maak, voorspel die gemengde rasionele interpolant 'n area waar die weerkaatskoëffisiënt onder -10 dB is met 'n 11.9% fout. Uit hierdie area word die antenna met die maksimum sensitiwiteit geïdentifiseer en die surrogaatmodel voorspel die sensitiwiteit by hierdie punt as gemiddeld $3.651 \text{ m}^2/\text{K}$. Validasie van die resultate wys dat die sensitiwiteit gelyk is aan 'n gemiddeld van $3.7139 \text{ m}^2/\text{K}$ en dat die weerkaatskoëffisiënt oor die hele bandwydte onder -10.52 dB is.

Acknowledgements

Over the past two years I was faced with many challenges and opportunities. The completion of this thesis would not have been possible without the support from the following people and organisations, to whom I am sincerely grateful:

- Prof. Dirk de Villiers, for your insight and advice on the various problems that were encountered during the course of this research project - working under your guidance has been an absolute pleasure. Thank you for your patient assistance during times that the results just didn't seem to work out and for your enthusiasm whenever they did. Thank you for generating results in GRASP and for making the arrangements for me to spend a semester researching at the University of Antwerp in Belgium.
- Prof. Annie Cuyt, for your help with the rational interpolation problems. Thanks for guiding me through this unknown territory, and also for your creative solutions to my application specific problem.
- Christophe Segers, for helping with the development of the B-Spline blended rational interpolant.
- The CMA research group at the University of Antwerp for making me feel welcome during my stay.
- My colleagues in the Radarlab and penthouse for our shared experiences as developing researchers. Special thanks to Keshav, TJ, Brandt, Nelis and Nancy for the moral support during our week at ICEAA in Verona.
- The National Research Foundation (NRF) for the financial assistance that made this project possible.
- EuroSA, for the scholarship that made my exchange program to Belgium possible.
- Thank you to the University of Stellenbosch's HPC1 (Rhasatsha), on which computations in FEKO were done.
- Mom, for being there for me when I felt like giving up and for helping me to compartmentalise the large task that stood before me. Thank you

for listening to my ICEAA presentation, and for convincing me to face the dragon.

- Etienne, for your support and understanding over the past two years. Thank you for your willingness to listen to my explanations of whatever I was struggling with, for sharing in my excitement over small victories, for checking my grammar and spelling, for your advice on the ICEAA presentation and for your genuine interest in my work.

Dedications

*To my mother, Elmarie Aberdein;
for reminding me how to eat an elephant.*

Contents

Declaration	i
Abstract	ii
Uittreksel	iv
Acknowledgements	vi
Dedications	viii
Contents	ix
List of Figures	xi
List of Tables	xvi
Nomenclature	xviii
1 Introduction	1
1.1 SKA background	1
1.2 Goal of the Project	4
1.3 Contents of the Thesis	6
2 Reflector Antenna Theory	7
2.1 Single Paraboloidal Reflector Antenna	7
2.2 Dual-Reflector System	9
2.3 Aperture Efficiency	12
2.4 Sensitivity	17
3 The Pyramidal Sinuous Antenna	24
3.1 Design Parameters	24
3.2 Design Objectives	28
3.3 Coarse Model	30
4 Fast Parametric Modeling of the Sensitivity	33
4.1 Space Mapping	33

CONTENTS

x

4.2	Simplifications to the Surrogate Model for Sensitivity Calculations	37
4.3	Comparisons of the Different Models	45
5	Rational Interpolation Scheme	47
5.1	Univariate Rational Interpolation	47
5.2	The Barycentric Formula	51
5.3	Rational Modeling of Multi-Fidelity Data	55
5.4	Getting Rid of the Poles in the Rational Approximant of the Multi-Fidelity Data	62
5.5	Pole-Free Rational Interpolation of Multi-Fidelity Data Using B-Splines	67
5.6	Multivariate Rational Interpolation	74
5.7	Comparisons of the B-Spline Blended Rational Interpolant with Other Surrogate Models	84
6	Design Examples	93
6.1	Surrogate Models of the Performance Metrics of a 5:1 Pyramidal Sinuous Antenna	93
6.2	Multi-Objective Optimisation of a 3:1 Pyramidal Sinuous Antenna	97
7	Conclusion and Further Recommendations	105
	Appendices	108
A	Results for Sensitivity Models	109
A.1	Model 1	109
A.2	Model 2	111
A.3	Model 3	113
	Bibliography	115

List of Figures

1.1	An artist's impression of the final design of the MeerKAT antenna. . . .	2
1.2	Wideband feed technologies being researched for the SKA.	3
2.1	Geometry of a paraboloidal reflector.	8
2.2	Geometry of dual-reflector antennas.	10
2.3	The concept of the equivalent parabolic surface.	11
2.4	The offset Gregorian configuration.	12
2.5	Illustration of the antenna radiation pattern and the brightness temperature of the surrounding scene.	18
2.6	Radiation patterns in dBi at 1.5 GHz.	20
2.7	Brightness temperature distribution in K for the main reflector masking approximation when pointing at zenith.	21
2.8	Radiation patterns in dBi at 500 MHz.	21
3.1	One arm of the sinuous antenna.	25
3.2	A self-complementary planar sinuous antenna.	26
3.3	The pyramidal sinuous antenna.	27
3.4	Illustration of the fine and coarse models used in FEKO simulations. (a) Fine model. (b) Coarse model at the low band edge. (c) Coarse model at the high band edge. Note that these coarse models are exaggerated for illustration purposes.	31
3.5	Figure illustrating the coarse model end effects. The black line is the fine model data. The blue line is the low band coarse model and the red line is the high band coarse model. The dashed parts of both models are not simulated as it contains end effects not present in the fine model. . .	31
4.1	Illustration of the space mapping procedure.	34
4.2	Sensitivity as a function of frequency for two different geometries. .	38
4.3	Sensitivity surrogates for Model 1.	39
4.4	Regression terms for Model 2.	41
4.5	Sensitivity surrogates for Model 2.	42
4.6	Sensitivity surrogates for Model 3.	44

5.1	Rational interpolants of the input impedance of the pyramidal sinuous antenna for variations in frequency when using equations (5.1) and (5.8) with the real and imaginary parts modeled separately. Here $\tau = 0.7825$, $\delta/\alpha = 0.6$, $\delta + \alpha = 36^\circ$ and $\theta = 53^\circ$	50
5.2	Rational interpolants of the input impedance of the pyramidal sinuous antenna for variations in frequency when using equations (5.1) and (5.8) with complex function values. Here $\tau = 0.7825$, $\delta/\alpha = 0.6$, $\delta + \alpha = 36^\circ$ and $\theta = 53^\circ$	51
5.3	Visual illustration of the barycentric rational interpolant with its blending functions $l_i(x)$. The choice of weights $w_i = (-1)^i$ ensures a pole-free region on the real line.	53
5.4	Rational interpolants of the input impedance of the pyramidal sinuous antenna for variations in frequency when using equation (5.14) with condition (5.15) used to ensure a pole-free model. $\tau = 0.7825$, $\delta/\alpha = 0.6$, $\delta + \alpha = 36^\circ$ and $\theta = 53^\circ$	54
5.5	Rational interpolants of the input impedance of the pyramidal sinuous antenna for variations in frequency when using equation (5.14) and (5.16). $\tau = 0.7825$, $\delta/\alpha = 0.6$, $\delta + \alpha = 36^\circ$ and $\theta = 53^\circ$	55
5.6	Illustration of the fine and coarse models used to create the low- and high-fidelity data.	56
5.7	Illustration of the low- and high-fidelity data.	57
5.8	Spline interpolant through the difference between the HF and LF data points used to calibrate the LF data.	58
5.9	Data LF_c found by calibrating the LF data. Note that for each interpolation point, f_k^H and $f_k^{L_c}$ coincides.	59
5.10	Rational interpolants of the input impedance of the pyramidal sinuous antenna for variations in frequency when using equations (5.20) and (5.23) with the real and imaginary parts modelled separately. $\tau = 0.7825$, $\delta/\alpha = 0.6$, $\delta + \alpha = 36^\circ$ and $\theta = 53^\circ$	61
5.11	Rational interpolants of the input impedance of the pyramidal sinuous antenna for variations in frequency when using equations (5.20) and (5.23) on the complex data sets. $\tau = 0.7825$, $\delta/\alpha = 0.6$, $\delta + \alpha = 36^\circ$ and $\theta = 53^\circ$	62
5.12	Rational interpolants of the input impedance of the pyramidal sinuous antenna for variations in frequency when using equations (5.20) and (5.23) with the constraint (5.25) used to ensure a pole-free model. Real and imaginary parts are modelled separately. $\tau = 0.7825$, $\delta/\alpha = 0.6$, $\delta + \alpha = 36^\circ$ and $\theta = 53^\circ$	64
5.13	Rational interpolants of the input impedance of the pyramidal sinuous antenna for variations in frequency when using equations (5.20) and (5.23) with the constraint (5.25) used to ensure a pole-free model. Models are on the complex data sets. $\tau = 0.7825$, $\delta/\alpha = 0.6$, $\delta + \alpha = 36^\circ$ and $\theta = 53^\circ$	65

5.14	Solutions to the weights w_2 and w_3 when the sufficient condition of equation (5.25) to ensure a pole-free model is applied (blue dot) compared to when the necessary condition of equation (5.15) to ensure a pole-free model is applied (yellow dot). The green area indicates the possible solution space of equation (5.15), while the red area indicates the possible solution space of equation (5.25).	66
5.15	The first four B-Spline functions.	68
5.16	Illustration of a Bèzier curve for approximation of data on an interval between $[0, 1]$.	69
5.17	Illustration of the quadratic B-Spline blending functions and the local models $p_k(x)$. The dashed parts are multiplied by zero and thus do not contribute to the interpolant.	70
5.18	Rational interpolants of the input impedance of the pyramidal sinuous antenna for variations in frequency when using equations (5.36) and (5.39) with the constraint that $w_k > 0$, ensuring a pole-free model. Real and imaginary parts are modelled separately. $\tau = 0.7825$, $\delta/\alpha = 0.6$, $\delta + \alpha = 36^\circ$ and $\theta = 53^\circ$.	72
5.19	Rational interpolants of the input impedance of the pyramidal sinuous antenna for variations in frequency when using equations (5.36) and (5.39) with the constraint that $w_k > 0$, ensuring a pole-free model. Models were applied directly to the complex data sets. $\tau = 0.7825$, $\delta/\alpha = 0.6$, $\delta + \alpha = 36^\circ$ and $\theta = 53^\circ$.	73
5.20	Illustration of Bèzier interpolation in two dimensions.	75
5.21	Rational interpolants of the input impedance of the pyramidal sinuous antenna for variations in τ and frequency when using equations (5.46) and (5.39) on the complex data. $\delta/\alpha = 0.6$, $\delta + \alpha = 36^\circ$ and $\theta = 53^\circ$.	77
5.22	Rational interpolants of the input impedance of the pyramidal sinuous antenna for variations in δ/α and frequency when using equations (5.46) and (5.39) on the complex data. $\tau = 0.825$, $\delta + \alpha = 36^\circ$ and $\theta = 53^\circ$.	78
5.23	Rational interpolants of the input impedance of the pyramidal sinuous antenna for variations in $\delta + \alpha$ and frequency when using equations (5.46) and (5.39) on the complex data. $\tau = 0.825$, $\delta/\alpha = 0.6$ and $\theta = 53^\circ$.	79
5.24	Rational interpolants of the input impedance of the pyramidal sinuous antenna for variations in θ and frequency when using equations (5.46) and (5.39) on the complex data. $\tau = 0.825$, $\delta/\alpha = 0.6$ and $\delta + \alpha = 36^\circ$.	80
5.25	Worst case of the reflection coefficient for variations in τ determined from the rational approximants of Figure 5.21.	81
5.26	Worst case of the reflection coefficient for variations in δ/α determined from the rational approximants of Figure 5.22.	81
5.27	Worst case of the reflection coefficient for variations in $\delta + \alpha$ determined from the rational approximants of Figure 5.23.	82
5.28	Worst case of the reflection coefficient for variations in θ determined from the rational approximants of Figure 5.24.	82

5.29	Comparisons of the AEE for the models listed in Table 5.6 as a function of the number of HF frequency points for the different geometric parameters.	87
5.30	Comparisons of the MAX for the models listed in Table 5.6 as a function of the number of HF frequency points for the different geometric parameters.	88
5.31	Comparisons of the AEE for the models listed in Table 5.6 as a function of the number of HF geometry points for the different geometric parameters.	89
5.32	Comparisons of the MAX for the models listed in Table 5.6 as a function of the number of HF geometry points for the different geometric parameters.	90
5.33	Comparisons of the AEE for the models listed in Table 5.6 as a function of the total number of HF points for the different geometric parameters. For clarity, the B-Spline blended rational interpolant is indicated by the red dots, and the model which compared the best is shown in blue, with all other models shown as black dots.	91
5.34	Comparisons of the MAX for the models listed in Table 5.6 as a function of the total number of HF points for the different geometric parameters. For clarity, the B-Spline blended rational interpolant is indicated by the red dots, and the model which compared the best is shown in blue, with all other models shown as black dots.	92
6.1	Rational interpolants of the input impedance of a 5:1 pyramidal sinuous antenna for variations in τ and frequency when using equations (5.46) and (5.39) on the complex data. $\delta/\alpha = 0.6$, $\delta + \alpha = 36^\circ$ and $\theta = 53^\circ$. . .	94
6.2	Worst case of the reflection coefficient for variations in τ determined from the rational approximants of Figure 6.1.	95
6.3	Sensitivity surrogate for Model 3a) with variations in τ	96
6.4	Worst case of the reflection coefficient for variations in τ and δ/α determined from the rational approximants.	98
6.5	Error values for the worst case of the reflection coefficient for variations in τ and δ/α	99
6.6	Regions where the worst case of the reflection coefficient for variations in τ and δ/α are less than -10 dB.	99
6.7	Comparison of regions where the worst case of the reflection coefficient for variations in τ and δ/α are less than -10 dB. The orange region indicates the true region below -10 dB and the red region indicates where the prediction is below -10 dB. The white areas are where the true region is below -10 dB, but the predicted value is not.	100
6.8	Sensitivity surrogate for Model 3a) with variations in τ and δ/α . Fine model validation data is indicated by black dots, coarse model data is indicated by stars and the training set for the regression term is shown encircled over a star distribution. The coloured surface indicates the surrogate model.	101
6.9	Reflection coefficient of the optimal design. $\tau = 0.87375$, $\delta/\alpha = 0.63$, $\delta + \alpha = 36^\circ$ and $\theta = 53^\circ$	102

6.10	Reflection coefficient of the optimal design when renormalised to an input impedance of $237\ \Omega$. $\tau = 0.87375$, $\delta/\alpha = 0.63$, $\delta + \alpha = 36^\circ$ and $\theta = 53^\circ$. .	103
6.11	Sensitivity as a function of frequency for the optimal design. $\tau = 0.87375$, $\delta/\alpha = 0.63$, $\delta + \alpha = 36^\circ$ and $\theta = 53^\circ$. The average sensitivity is $3.7139\ \text{m}^2/\text{K}$	104
A.1	Sensitivity surrogates for Model 1 of the objective function $U^{(b)}$	109
A.2	Sensitivity surrogates for Model 1 of the objective function $U^{(c)}$	110
A.3	Sensitivity surrogates for Model 2 of the objective function $U^{(b)}$	111
A.4	Sensitivity surrogates for Model 2 of the objective function $U^{(c)}$	112
A.5	Sensitivity surrogates for Model 3 of the objective function $U^{(b)}$	113
A.6	Sensitivity surrogates for Model 3 of the objective function $U^{(c)}$	114

List of Tables

1.1	Frequency bands for SKA1-mid.	2
1.2	Performance metrics of the corrugated horn used in the MeerKAT system.	3
1.3	Performance metrics of the QRFH used for Band 1 of SKA1-mid.	4
3.1	Design parameters for the pyramidal sinuous antenna.	28
3.2	Design objectives.	30
3.3	Input parameters for the design space exploration.	30
3.4	Comparison of fine and coarse models.	32
4.1	Overview of the difference between the different surrogate models.	37
4.2	Percentage errors for Model 1.	39
4.3	Number of fine model points required for Model 1.	40
4.4	Percentage errors for Model 2.	42
4.5	Number of points required for Model 2.	43
4.6	Percentage errors for Model 3.	44
4.7	Number of points required for Model 3.	45
4.8	Summary of the different models which were described.	45
4.9	Percentage errors for the different models.	46
4.10	CPU time required for the different models for variations in $\delta + \alpha$	46
5.1	Error values for interpolants of Figures 5.12 and 5.13.	67
5.2	Error values for interpolants of Figures 5.18 and 5.19	73
5.3	Grids on which interpolants are built for every geometric parameter.	76
5.4	Error values for interpolants of Figures 5.21 - 5.24.	83
5.5	Error values for the reflection coefficient of Figures 5.25 - 5.28.	83
5.6	Surrogate models used in the comparison study.	86
6.1	Error values for the rational interpolation model of a 5:1 pyramidal sinuous antenna.	95
6.2	Error values for the sensitivity surrogate model of a 5:1 pyramidal sinuous antenna.	96
6.3	CPU time required for the different models for of a 5:1 pyramidal sinuous antenna.	97
6.4	Grid on which interpolants are built in three dimensions.	97

6.5	Error values from the rational interpolation models built on the grid in Table 6.4.	98
6.6	Percentage of the area that has a reflection coefficient less than -10 dB.	100
6.7	Error values for the sensitivity surrogate models for variations in τ and δ/α	101
A.1	Percentage errors for Model 1.	110
A.2	Percentage errors for Model 2.	112
A.3	Percentage errors for Model 3.	114

Nomenclature

Abbreviations

AEE	Average Euclidean Error
ARE	Average Relative Error
CEM	Computational Electromagnetic
CMB	Cosmic Microwave Background
CPU	Central Processing Unit
GO	Geometrical Optics
HF	High-fidelity
LF	Low-fidelity
LS	Least Squares
MAX	Maximum Average Error
MF	Multi-fidelity
MLE	Maximum Likelihood Estimation
MOM	Method-of-Moments
MRE	Maximum Relative Error
PO	Physical Optics
PTD	Physical Theory of Diffraction
QRFH	Quad-ridged flared horn
QSC	Quasi-self-complementary
RFI	Radio Frequency Interference
RMSE	Root Mean Squared Error
RRSE	Root Relative Squared Error
SBO	Surrogate Based Optimization
SKA	Square Kilometre Array
SM	Space Mapping
UWB	Ultra wideband
XPOL	Cross-polarisation

Definitions

Fine Model	An accurate model of the problem that is expensive to evaluate.
Coarse Model	A less accurate model of the problem which is cheap to evaluate.
Surrogate Model	A model that is evaluated using only a few fine model data points. Coarse model data points may be used to supplement the surrogate, so that a more accurate solution is obtained.
HF Data	Data points sampled from the fine model.
LF Data	Data points sampled from the coarse model.

Chapter 1

Introduction

1.1 SKA background

The Square Kilometre Array (SKA) project is a massive scientific and engineering undertaking to construct the world's largest radio interferometer, about 50 times more sensitive than any currently in existence [1]. It will see farther and wider into the universe than currently possible and aims to answer questions such as, among others [2]:

- "how old is the universe?"
- "what is dark matter?"
- "when did the first stars form?"
- "what are gravitational waves?"

In order to do this, it is necessary for extensive research into a wide range of engineering fields, which includes, but are not limited to, wideband feeds, low-cost dish antennas, shielding of component radio frequency interference (RFI), mitigation of external RFI, and low-cost, reliable remote operation of the telescope [3]. The SKA is divided into two site entities, one in Western Australia and one in Southern Africa, namely SKA1-mid. A precursor to SKA1-mid is the MeerKAT [3], which is currently under construction in the Karoo, about 90 km from the town of Carnarvon in the Northern Cape. It consists of 64 offset Gregorian dish antenna structures each with a 13.5 m effective diameter main reflector and a 3.8 m diameter subreflector. The equivalent F/D ratio is 0.55 which is equal to a 48.9° subtended half angle [4]. Figure 1.1 shows an illustration of the final design.



Figure 1.1: An artist's impression of the final design of the MeerKAT antenna.
SOURCE: Figure 2a) [5].

MeerKAT will be integrated into SKA1-mid, along with a further 133 dishes. Each dish is capable of handling five cryo-cooled receiver packages, each of which can be moved to the focal position. The 5 different frequency bands for SKA1-mid is listed in Table 1.1.

Table 1.1: Frequency bands for SKA1-mid.

Band	Range [GHz]	Bandwidth
1	0.35 - 1.05	3:1
2	0.95 - 1.76	1.85:1
3	1.65 - 3.05	1.85:1
4	2.80 - 5.18	1.85:1
5	4.6 - 13.8	3:1

For the narrower bands, a wide flare angle axially corrugated conical horn was designed in [6] and further optimised for sensitivity in [7]. Table 1.2 lists some of the key performance metrics of this corrugated horn.

Table 1.2: Performance metrics of the corrugated horn used in the MeerKAT system [7], [6].

Metric	Value
Reflection Coefficient	< -18 dB
Aperture efficiency	$> 74\%$
Sensitivity	> 4.7 m ² /K
Second sidelobe level	< -25 dB
XPOL (-1 dB main beam contour)	< -25 dB
XPOL (-3 dB main beam contour)	< -30 dB

The 3:1 bands are already wideband compared to conventional octave band horns. Furthermore, the development of an ultra wideband (UWB) feed that could cover a much wider bandwidth than the current best feeds would greatly reduce system costs, as well as having scientific benefits. Several feeds with operating bandwidths up to a decade have recently been developed around the world, but with inferior performance compared to the octave band horn used in the MeerKAT system. These include the eleven feed [8], the quad-ridged flared horn (QRFH) [9], the log-periodic antenna used in the Allen Telescope Array [10], the quasi-self-complementary (QSC) ultrawideband feed [11] and the sinuous feed [12], all shown in Figure 1.2.

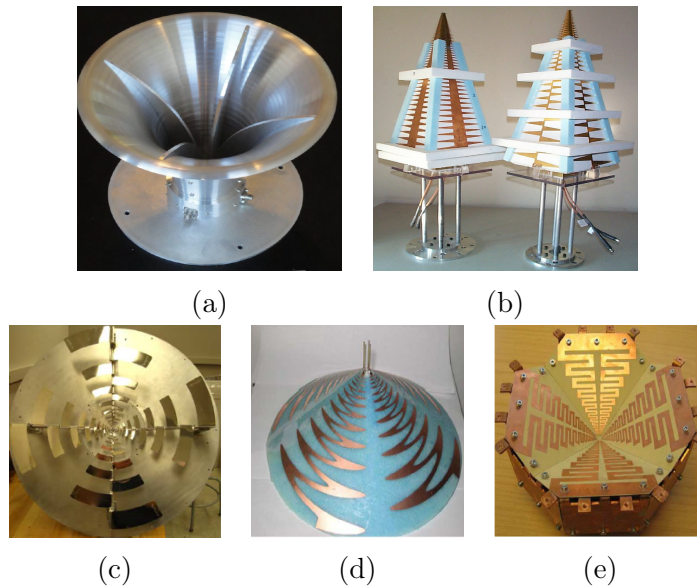


Figure 1.2: Wideband feed technologies being researched for the SKA: (a) The quad-ridged flared horn [9]; (b) The log-periodic antenna [10]; (c) The quasi-self-complementary feed [11]; (d) The sinuous feed [12]; (e) The eleven feed [13].

Feeds (b)-(e) of Figure 1.2 are all log-periodic type antennas over a ground plane. Their log-periodicity is what gives these feeds their wideband behaviour, while the ground plane ensures a uni-directional radiation pattern.

The requirements for a wideband feed are strict, including a constant beamwidth over frequency, a circularly symmetric radiation pattern, small phase center variation, low cross-polarisation levels and a low reflection coefficient in order to realise a high aperture efficiency and system sensitivity. In addition to these requirements, the feed needs to have a compact size so that it can be cooled inside a cryostat, which ensures low system noise temperature. For Band 1 of SKA1-mid an optimised design of the QRFH has been done [14]. As the horn will be too large at these frequencies, the horn itself will be at room temperature, with its electronics cryogenically cooled. Its performance is listed in Table 1.3.

Table 1.3: Performance metrics of the QRFH used for Band 1 of SKA1-mid [14].

Metric	Value
Reflection Coefficient	< -10 dB
Aperture efficiency	$> 70\%$
Sensitivity	$4.2 \text{ m}^2/\text{K}$ average

1.2 Goal of the Project

There are always trade-offs to be considered in engineering design tasks, since the improvement of a certain performance metric could lead to the degradation of another. To be a suitable candidate for the SKA, a wideband feed design must adhere to strict requirements. In this case, it is worthwhile to perform formal multi-objective optimisation on the various feeds that are considered, to ensure that the best possible solution is used. Unfortunately this becomes a very difficult task, attributed to the long simulation time of full wave electromagnetic solvers which is required for a large number of different evaluations of each antenna technology, in order to find the best candidate from a high dimensional design space. Surrogate based optimisation (SBO) is a technique which is often used to overcome such restrictions. It involves the search for a suitable coarse model, which is much faster to evaluate than the full, accurate fine model. The coarse model needs to retain the underlying physical behaviour of the fine model. A surrogate model is then constructed by aligning the coarse model to the fine model, using only a few fine model evaluations. The idea is to speed up the design process while maintaining model accuracy. In this project, the design of a pyramidal sinuous antenna is considered. A

design is sought that provides the maximum sensitivity, while simultaneously adhering to an adequate reflection coefficient over the entire band. A simple surrogate modelling method is considered which approximates the sensitivity of the feed. For the reflection coefficient, the use of rational interpolation models is explored, since rational functions are known to be well-suited for modelling the output behaviour of antenna structures as a function of frequency [15], [16], [17].

Rational interpolation methods which make use of high-fidelity (HF) data from the fine model antenna structure are considered first. In order to improve the accuracy of the models without excessively increasing the design time, consideration is given to rational interpolation models that utilise multi-fidelity (MF) data. In these cases, the low-fidelity (LF) data is found from truncated coarse model antenna structures that provide information of the output of the antenna at the band edges at a reduced computational cost. These coarse models are suitable candidates for log-periodic type structures such as the pyramidal sinuous antenna, since the geometry of the structure repeats itself log-periodically. The output from such antennas are also log-periodic.

Pole-free rational functions which ensure that the rational interpolants do not contain any unattainable points are desirable. The multi-fidelity rational interpolants are made to follow the low-fidelity data in a least-squares (LS) sense by calculating appropriate weights for the model. Applying the sufficient condition for ensuring a pole-free model to these weights leads to a restricted rational interpolant that is unable to adequately follow the trend of the low-fidelity data. This problem is overcome by the introduction of a rational interpolant that locally models the trend of the low-fidelity data with a Bèzier curve. These local models are then blended together with quadratic B-spline functions into a global rational interpolation function.

An in-depth discussion of the univariate (one-dimensional) rational interpolation methods are provided. These are then extended to the multivariate (n-dimensional) case. The blended rational interpolant which makes use of B-splines is applied to the input impedance of the antenna, first only as a function of frequency and then it is extended to include variations in the geometric parameters that describe the pyramidal sinuous antenna. The reflection coefficient of the structure is calculated from these models. The thesis concludes with a design example of the antenna over a 3:1 bandwidth which provides the maximum sensitivity, while maintaining an acceptable reflection coefficient over the entire band.

1.3 Contents of the Thesis

Chapter 2 gives an overview of reflector antennas. Approximate calculations of the aperture efficiency and noise temperature of the system are discussed. Both components are required for calculation of the sensitivity of the system.

Chapter 3 describes the pyramidal sinuous antenna, with specific attention given to its design parameters. The design objectives of the feed is discussed and the coarse models that are used to approximate the fine model is introduced.

In Chapter 4, a simple surrogate modelling method is introduced that models the sensitivity of the system. Three surrogate models with different coarse models are described. A comparison of the computation times for the fine and surrogate models are provided.

Chapter 5 provides an extensive description of rational modelling techniques and finally a method is arrived at which adequately models the input impedance of the antenna, from which the reflection coefficient is then calculated. The chapter ends off by comparing this method with other interpolation schemes.

Chapter 6 considers the design of the pyramidal sinuous antenna by using the surrogate modelling methods which are discussed in Chapters 4 and 5. An optimal design is found from a domain which simultaneously varies two of the geometric parameters of the antenna.

Chapter 7 provides conclusions which can be drawn from this thesis, as well as a discussion of possible future work that can be done to improve upon it.

Chapter 2

Reflector Antenna Theory

Reflector antenna systems consist of one or more curved reflectors which are designed to collimate an incident plane wave to a focal point. The feed is placed at this location. In transmit mode, the feed illuminates the reflector in order to generate a desired field distribution in the aperture in front of the main reflector. The emerging beams are highly directional, well-suited for low noise applications such as radio astronomy. A single reflector system will normally consist of a paraboloidal dish, while typical dual-reflector systems either utilises the Cassegrain form, which includes a hyperboloidal subreflector in addition to a paraboloidal main reflector, or the Gregorian form, which has an ellipsoidal subreflector surface. The MeerKAT system makes use of an offset Gregorian configuration, as mentioned in Chapter 1, while the SKA will make use of a shaped offset Gregorian configuration. In a shaped system, the designer has more control over the amplitude and phase of the radiation pattern produced in the aperture.

2.1 Single Paraboloidal Reflector Antenna

Reflector antenna problems are commonly analysed by two different approximation methods, namely the Physical Optics (PO) approximation, and the Geometrical Optics (GO) approximation. These are asymptotically correct for large reflector surfaces. The following approximations are made in both methods [18]:

1. There are no fields on the shadow side of the reflector.
2. The discontinuity of the current density on the rim of the reflector is not considered.
3. Direct radiation from the feed and aperture blockage by the feed are not taken into account.

In the PO approximation, the surface current at a point on a curved, perfectly conducting scatterer is considered equal to what the surface current would have been on an infinite planar surface tangent to this point, according to the formula

$$\mathbf{J}_s = 2\hat{n} \times \mathbf{H}^i \quad (2.1)$$

where \mathbf{J}_s is the surface current density, \hat{n} is a unit vector normal to the surface and \mathbf{H}^i is the incident magnetic field. This is a good approximation for a scattering surface which is large in terms of wavelengths, as the condition can be considered to be met locally. For the GO approximation, electromagnetic fields in free space are considered to propagate along straight lines or rays. The rays are reflected at the surface of the reflector according to Snell's reflection law.

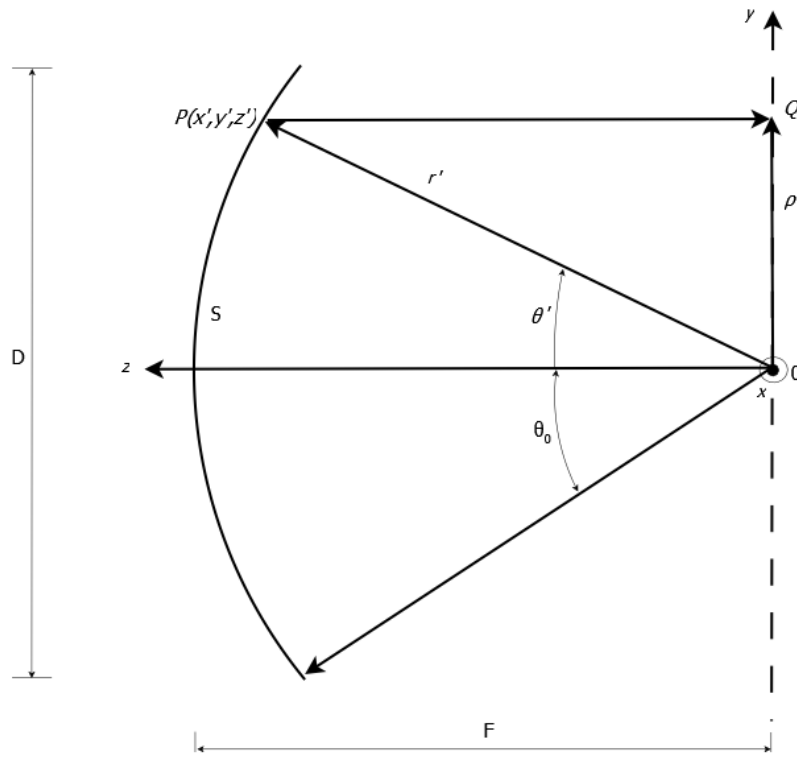


Figure 2.1: Geometry of a paraboloidal reflector.

Following the derivation in [18], with reference to Figure 2.1 and from the definition of a parabola, we have

$$OP + PQ = \text{constant} = 2F$$

where F is the focal length of the parabola. So

$$r' + r' \cos \theta' = 2F$$

and

$$r' = \frac{2F}{1 + \cos \theta'} = F \sec^2(\theta'/2) \quad \theta' \leq \theta_0$$

or in Cartesian coordinates

$$\sqrt{(x')^2 + (y')^2 + (z')^2} + z' = 2F$$

or

$$(x')^2 + (y')^2 = 4F(F - z').$$

Since $(x')^2 + (y')^2 = (\rho')^2$, this can be written as

$$(\rho')^2 = 4F(F - z') \quad \text{with} \quad 0 \leq \rho' \leq D/2.$$

D is the diameter of the paraboloid. Further useful formulas relating the geometry of the paraboloid include

$$\rho' = r' \sin \theta' = F \sec^2(\theta'/2) \sin \theta' = 2F \tan(\theta'/2) \quad (2.2)$$

and

$$d\rho'/d\theta' = F \sec^2(\theta'/2). \quad (2.3)$$

The following equations relate the variables θ_0 , F and D of the parabola, with θ_0 the subtended half-angle of the paraboloid. Since $\theta' = \theta_0$ when $\rho' = D/2$, from equation (2.2),

$$D = 4F \tan(\theta_0/2) \quad (2.4)$$

or

$$F = \left(\frac{D}{4}\right) \cot(\theta_0/2). \quad (2.5)$$

2.2 Dual-Reflector System

In a dual-reflector antenna configuration, fields emanating from the feed travel equal distances towards a subreflector and are reflected to the main reflector where it is further reflected towards the aperture as parallel rays. As mentioned, two popular configurations are the Cassegrain and Gregorian forms. Both utilise a paraboloidal main reflector, but the Cassegrain's subreflector is a hyperboloid, while the Gregorian subreflector is an ellipsoid. As illustrated in Figure 2.2, the feed is placed to coincide with one of the focal points of the ellipsoid/hyperboloid at F_1 , while the other focal point coincides with the paraboloid's focal point at F_2 .

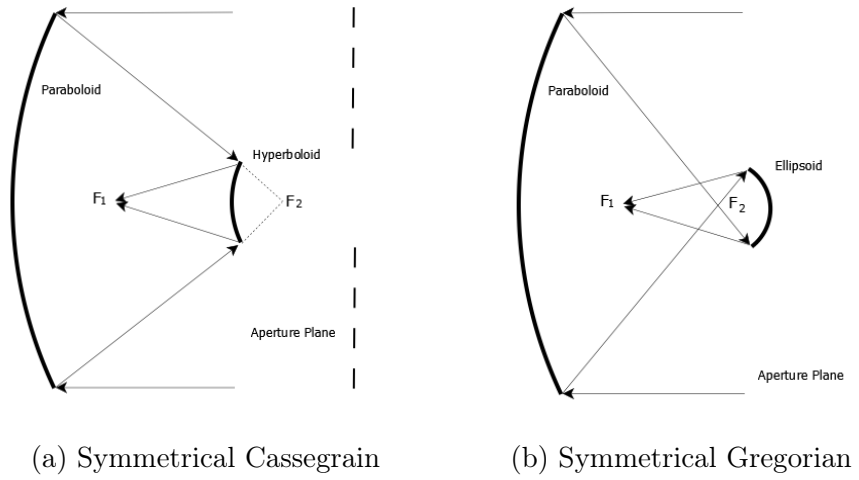


Figure 2.2: Geometry of dual-reflector antennas.

2.2.1 The Equivalent Paraboloid

A useful concept in the analysis of dual-reflector systems is that of the equivalent parabola. In this case, the subreflector acts as a magnifier, resulting in an equivalent parabolic surface with a larger effective focal distance F_e . This surface can be found through ray tracing, as illustrated in Figure 2.3 from [18]. The dual-reflector system can now be approximated by its equivalent paraboloid if blockage caused by the subreflector, as well as diffraction from its edges are taken into account.

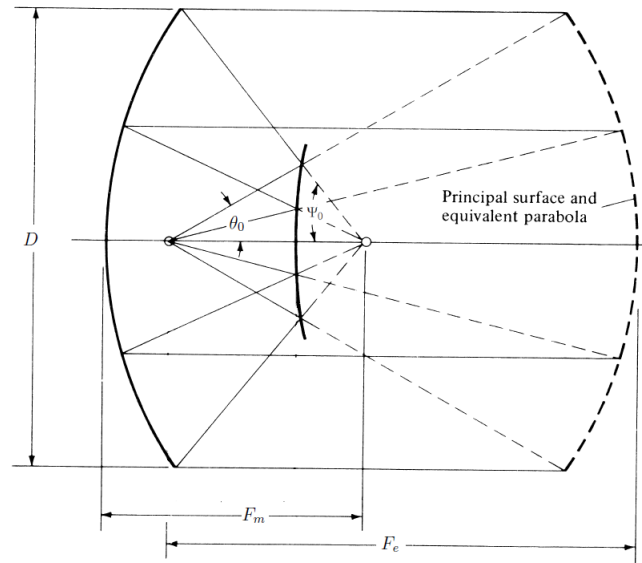


Figure 2.3: The concept of the equivalent parabolic surface.

SOURCE: Fig. 15.30, p. 931 [18] (edited).

2.2.2 Offset Gregorian Dual-Reflector Antenna

An offset configuration is beneficial as blockage from the feed, supporting struts and subreflector surface are eliminated. Figure 2.4 illustrates the offset Gregorian configuration which can be described in terms of five parameters [19] if the Mizugutch condition for minimum cross-polarisation is satisfied [20]. Since the feed is not in the path of the optical rays, multiple feeds can be installed to cover all the frequency ranges listed in Table 1.1.

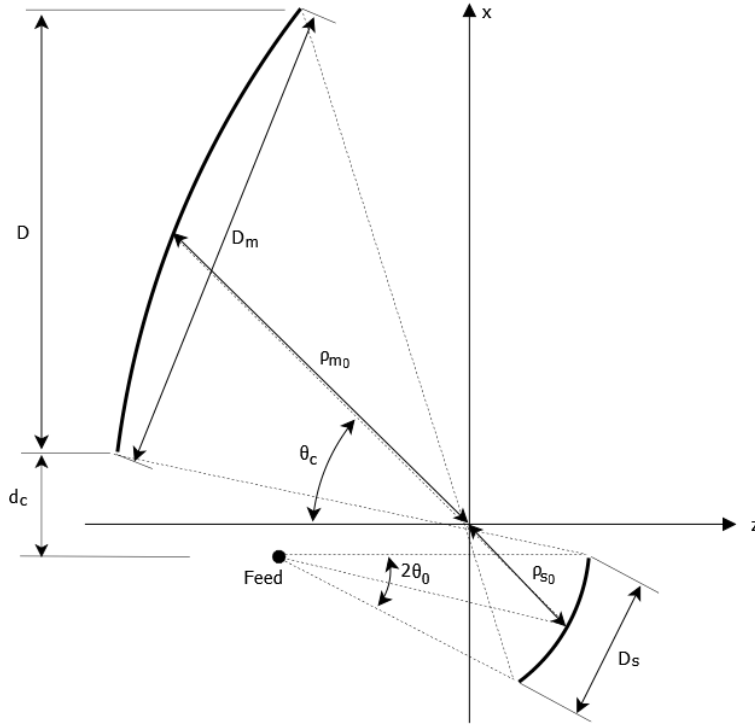


Figure 2.4: The offset Gregorian configuration.

2.3 Aperture Efficiency

An important performance metric used to characterise a reflector antenna system is the aperture efficiency. The aperture efficiency is the ratio of the radiation intensity in the desired polarisation on axis, to the radiation intensity that would be produced by an aperture radiating the same total power, but having a uniform constant phase aperture field with no cross-polarisation [21]. From this definition an effective aperture area is derived according to

$$A_{eff} = \eta_{ap} A_{ph} \quad (2.6)$$

where η_{ap} denotes the aperture efficiency and A_{ph} is the physical area of the aperture. For the case of a paraboloidal main reflector $A_{ph} = \pi \left(\frac{D}{2}\right)^2$, where D is the aperture's projected diameter. η_{ap} is dependent on the far-field radiation pattern of the feed. For an accurate measure of η_{ap} , simulations can be done using the software package GRASP [22], which uses physical optics (PO) and physical theory of diffraction (PTD). Improved accuracy is obtained by incorporating PTD, since it compensates for the discontinuity of the currents on the edges of the reflector, which is not done in PO, as mentioned previously.

The far-field radiation pattern of the feed can be expressed as

$$\mathbf{E}(r, \theta, \phi) = \frac{1}{r} e^{-jkr} \mathbf{G}(\theta, \phi) \quad (2.7)$$

where

$$\mathbf{G}(\theta, \phi) = G_\theta(\theta, \phi)\hat{\boldsymbol{\theta}} + G_\phi(\theta, \phi)\hat{\boldsymbol{\phi}} \quad (2.8)$$

and $k = \frac{2\pi}{\lambda}$. Furthermore, the ϕ -variation of the far-field function can be expanded in a Fourier series, because ϕ is periodic with a period of 2π :

$$\begin{aligned} \mathbf{G}(\theta, \phi) = & \sum_{n=0}^{\infty} [A_n(\theta)\sin(n\phi) + B_n(\theta)\cos(n\phi)]\hat{\boldsymbol{\theta}} \\ & + \sum_{n=0}^{\infty} [C_n(\theta)\cos(n\phi) - D_n(\theta)\sin(n\phi)]\hat{\boldsymbol{\phi}} \end{aligned} \quad (2.9)$$

When simulations are done or measurements are taken, the far-field function will only be available in a finite number of N ϕ -planes,

$$G_\theta(\theta, k\Delta\phi), G_\phi(\theta, k\Delta\phi), \quad k = 0, 1, \dots, N-1$$

where $\Delta\phi = \frac{2\pi}{N}$. Thus, the Fourier coefficients can be calculated with the inverse Fourier transform as

$$\begin{aligned} A_n(\theta) &= \frac{2}{N} \sum_{k=0}^{N-1} G_\theta(\theta, k\Delta\phi)\sin(kn\Delta\phi) \\ B_n(\theta) &= \frac{2}{N} \sum_{k=0}^{N-1} G_\theta(\theta, k\Delta\phi)\cos(kn\Delta\phi) \\ C_n(\theta) &= \frac{2}{N} \sum_{k=0}^{N-1} G_\phi(\theta, k\Delta\phi)\cos(kn\Delta\phi) \\ D_n(\theta) &= \frac{2}{N} \sum_{k=0}^{N-1} G_\phi(\theta, k\Delta\phi)\sin(kn\Delta\phi) \end{aligned} \quad (2.10)$$

with $n = 0, \dots, (N-1)/2$ [23].

If an accurate solution of the far-field radiation pattern is available, for example, after simulating the system in GRASP, then the aperture efficiency is calculated by taking the ratio of on-axis gain to the maximum possible gain which is available for an aperture antenna, given as

$$|G|_{\max}^2 = \frac{4\pi}{\lambda^2} A = \left(\frac{\pi D}{\lambda} \right)^2, \quad (2.11)$$

and then

$$(\eta_{ap})_{\text{dB}} = 20 \log \left(\frac{|\mathbf{G}(0, 0)|}{|G|_{\max}} \right). \quad (2.12)$$

To calculate η_{ap} by using the GO approximation, the aperture efficiency is broken up into sub-efficiency factors to account for different losses as [24]

$$\eta_{ap} = \eta_{BOR1} \eta_{sp} \eta_{ill} \eta_{ph} \eta_{pol} \eta_d \quad (2.13)$$

where η_{BOR1} is the Body of Revolution Type-1 (BOR₁) efficiency, η_{sp} is the spillover efficiency, η_{ill} is the illumination or taper efficiency, η_{ph} is the phase efficiency, η_{pol} is the polarisation efficiency and η_d is the diffraction efficiency. Note that losses caused from aperture blockage by the feed and struts are ignored. This is valid for the offset Gregorian configuration.

BOR₁ Efficiency

Many antennas are mechanically rotationally symmetric or bodies of revolution (BOR), such as paraboloidal reflector antennas. When only the $n = 1$ ϕ -variation of (2.9) is excited, the antenna is referred to as a BOR₁ antenna and the $n = 1$ terms are referred to as the BOR₁ component [25]. For any antenna, only the $n = 1$ terms of the Fourier ϕ -series contributes to on-axis radiation, while the higher order ϕ -modes represent power lost in sidelobes. Thus

$$\eta_{BOR1} = \frac{\int_0^{2\pi} \int_0^\pi [|G_{\theta 1}|^2 + |G_{\phi 1}|^2] \sin\theta d\theta d\phi}{\int_0^{2\pi} \int_0^\pi [|G_\theta(\theta, \phi)|^2 + |G_\phi(\theta, \phi)|^2] \sin\theta d\theta d\phi} \quad (2.14)$$

where

$$G_{\theta 1} = A_1(\theta) \sin(\phi) + B_1(\theta) \cos(\phi)$$

$$G_{\phi 1} = C_1(\theta) \cos(\phi) - D_1(\theta) \sin(\phi).$$

The calculation of the BOR₁ efficiency implies that the antenna can be excited for at most 2 polarisations orthogonal to the axis of symmetry. For a linear y-polarisation, B_1 and D_1 will be zero. Similarly for an x-polarised antenna, A_1 and C_1 will be zero. For the y-polarised case

$$\mathbf{E}(r, \theta, \phi) = \frac{1}{r} e^{-jkr} \left(A_1(\theta) \sin\phi \hat{\boldsymbol{\theta}} + C_1(\theta) \cos\phi \hat{\boldsymbol{\phi}} \right) \quad (2.15)$$

whereas for the x-polarised case

$$\mathbf{E}(r, \theta, \phi) = \frac{1}{r} e^{-jkr} \left(B_1(\theta) \cos(\phi) \hat{\boldsymbol{\theta}} - D_1(\theta) \sin(\phi) \hat{\boldsymbol{\phi}} \right). \quad (2.16)$$

The y-polarised case is considered here. A useful relationship exists between the co- and cross-polarised radiation functions in the $\phi = 45^\circ$ plane, and the radiation functions in the E- ($A_1(\theta)$) and H-plane ($C_1(\theta)$). Using Ludwig's third definition [26], the unit vectors for the co- and cross-polar directions for a y-polarised antenna are

$$\hat{\mathbf{u}}_{co} = \sin\phi \hat{\boldsymbol{\theta}} + \cos\phi \hat{\boldsymbol{\phi}}$$

$$\hat{\mathbf{u}}_{cx} = \cos \phi \hat{\boldsymbol{\theta}} - \sin \phi \hat{\boldsymbol{\phi}}$$

which gives the co- and cross-polar components of the radiation field as

$$G_{CO} = \mathbf{G}(\theta, \phi) \cdot \hat{\mathbf{u}}_{co} = CO(\theta) - XP(\theta)\cos(2\phi) \quad (2.17)$$

$$G_{XP} = \mathbf{G}(\theta, \phi) \cdot \hat{\mathbf{u}}_{xp} = CO(\theta)\sin(2\phi) \quad (2.18)$$

where

$$CO(\theta) = \frac{A_1(\theta) + C_1(\theta)}{2} \quad (2.19)$$

$$XP(\theta) = \frac{A_1(\theta) - C_1(\theta)}{2} \quad (2.20)$$

are seen to be the co- and cross-polar patterns in the $\phi = 45^\circ$ plane. The BOR₁ notations for the far-field are advantageous, since for further efficiency factors the ϕ -integral does not need to be evaluated.

Spillover Efficiency

The spillover efficiency is a measure of how much of the radiated power from the feed is captured by the reflector surface, i.e. the power within the subtended half-angle θ_0 . This is a very important metric, as the amount of power which goes past the reflector surface increases the system noise temperature, as explained in the next section. It is given by

$$\eta_{sp} = \frac{\int_0^{\theta_0} [|CO(\theta)|^2 + |XP(\theta)|^2] \sin\theta d\theta}{\int_0^\pi [|CO(\theta)|^2 + |XP(\theta)|^2] \sin\theta d\theta}. \quad (2.21)$$

Illumination Efficiency

The illumination efficiency is sometimes called the taper efficiency and is a measure of the uniformity of the amplitude distribution of the field over the surface of the reflector.

$$\eta_{ill} = 2\cot^2(\theta_0/2) \frac{\left[\int_0^{\theta_0} |CO(\theta)| \tan(\theta/2) d\theta \right]^2}{\int_0^{\theta_0} |CO(\theta)|^2 \sin\theta d\theta}. \quad (2.22)$$

Note that there is a trade-off between the illumination and spillover efficiencies, since a more uniformly illuminated reflector surface implies that more power will be spilled past the reflector surface. For a given half-angle θ_0 , there is a unique solution to the edge taper which gives the optimal combined illumination and spillover efficiency factors.

Polarisation Efficiency

Polarisation efficiency is defined as the power of the co-polar field relative to the total power within θ_0 and for linear polarisation is given as

$$\eta_{pol} = \frac{\int_0^{\theta_0} [|CO(\theta)|^2 + \frac{1}{2}|XP(\theta)|^2] \sin\theta d\theta}{\int_0^{\theta_0} [|CO(\theta)|^2 + |XP(\theta)|^2] \sin\theta d\theta}. \quad (2.23)$$

Phase Efficiency

Phase efficiency is a measure of the uniformity of the field's phase over the aperture plane, given by

$$\eta_{ph} = \frac{\left| \int_0^{\theta_0} CO(\theta) \tan(\theta/2) d\theta \right|^2}{\left[\int_0^{\theta_0} |CO(\theta)| \tan(\theta/2) d\theta \right]^2}. \quad (2.24)$$

This is the only sub-efficiency which is dependent on the feed's location relative to the focal point of the reflector. The phase center of the feed is uniquely defined as the feed location which maximises the phase efficiency.

Diffraction Efficiency

For dual-reflector systems it is necessary to account for the effects of diffraction from the edges of the subreflector. The subreflector is typically much smaller than the main reflector, thus diffraction from its edges become notable. An analytical expression is provided in [27] for a far-field function approximated by the expression

$$G(\theta) = (n+1) \cos^{2n}(\theta/2). \quad (2.25)$$

The value of n can be determined by fitting $G(\theta)$ onto the simulated far-field function, up to the subtended half-angle θ_0 . The diffraction efficiency can then be calculated as

$$\eta_d = \left| 1 + \frac{n \sin^2(\theta_0/2) \cos^n(\theta_0/2)}{1 - \cos^n(\theta_0/2)} \frac{(j-1) \Delta\rho}{\sqrt{2\pi} D} \right|^2 \quad (2.26)$$

where D is the projected aperture's diameter and

$$\Delta\rho = \sqrt{\frac{\lambda \rho_{m_0} + \sigma \rho_{s_0}}{\pi} \left| \frac{\rho_{m_0}}{\rho_{s_0}} \right|}, \quad (2.27)$$

with ρ_{m_0} and ρ_{s_0} the distances along the central ray from the virtual focal point to the main and sub- reflectors, respectively. These are indicated in Figure 2.4, where the virtual focal point corresponds to the origin and the central ray is indicated by θ_c . In equation (2.27), λ refers to the wavelength and the value of σ is set to 1 for Gregorian systems and to -1 for Cassegrain systems.

2.4 Sensitivity

The sensitivity is a measure of the minimum detectable signal that the system can receive. For the SKA, the primary objective is to maximise the sensitivity over multiple octave bandwidths for all the feed antennas to be used. Since radio astronomy sources are light years away, they are particularly difficult to detect. For a radio interferometer composed of multiple reflector antenna systems, the sensitivity of the entire system is dependent on the sensitivity of each reflector antenna system. Thus by increasing the sensitivity of each single system, even if only by a few percent, fewer reflector antenna systems are required to achieve the same total sensitivity, leading to large cost savings.

The sensitivity of the system is defined as the ratio of the effective aperture area to the system noise temperature, i.e.

$$\begin{aligned} \text{Sensitivity} &= \frac{A_{eff}}{T_{sys}} \\ &= \frac{\eta_{ap} A_{ph}}{T_{sys}} \\ &= \frac{\eta_{ap} \pi (D/2)^2}{T_{sys}} \end{aligned} \quad (2.28)$$

where T_{sys} is the system noise temperature, which is a combination of the antenna and the receiver noise, i.e.

$$T_{sys} = T_A + T_{rec}. \quad (2.29)$$

The SKA will make use of cryogenic cooling to ensure a low receiver noise. For the purposes of this thesis, it assumes a fixed value of $T_{rec} = 25$ K. For the antenna noise temperature T_A , the derivation and notation from [28] is followed. This requires integration of the product of the radiation pattern of the antenna $P(f, \theta, \phi | \hat{\mathbf{r}}_0)$ (at a frequency f and when pointing in the direction $\hat{\mathbf{r}}_0$) with the surrounding scene brightness temperature $T_b(f, \theta, \phi)$ over the entire 4π steradian sphere. This is normalised by the total power to give the antenna noise temperature. The calculation of $T_b(f, \theta, \phi)$ is as suggested in [29], supplemented by the approximation referred to as Model 3 in [28]. Sensitivity calculations were implemented from in-house code available at Stellenbosch University.

The antenna noise temperature is given by

$$T_A(f | \hat{\mathbf{r}}_0) = \frac{\iint_{4\pi} N(f, \theta, \phi | \hat{\mathbf{r}}_0) \sin \theta d\theta d\phi}{\iint_{4\pi} P(f, \theta, \phi) \sin \theta d\theta d\phi}, \quad (2.30)$$

where

$$N(f, \theta, \phi | \hat{\mathbf{r}}_0) = T_b(f, \theta, \phi) P(f, \theta, \phi | \hat{\mathbf{r}}_0). \quad (2.31)$$

The brightness temperature distribution of the scene surrounding the antenna is illustrated in Figure 2.5 from [29].

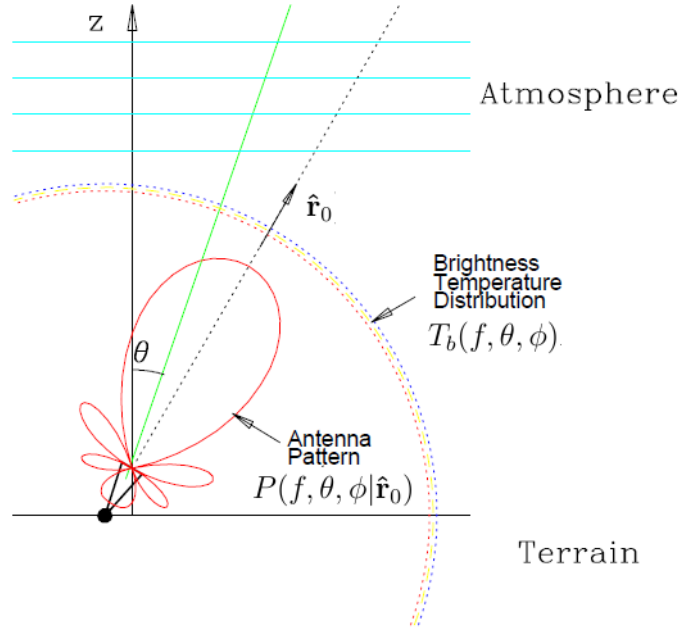


Figure 2.5: Illustration of the antenna radiation pattern and the brightness temperature of the surrounding scene. SOURCE: Figure 1, p. 1 [29] (edited).

To account for different pointing directions of the antenna, the brightness temperature model is rotated around a horizontal angle by the tipping angle θ_p . It can now be described in terms of the rotated coordinates $\theta'(\theta_p, \theta, \phi)$. The brightness temperature model is rotationally symmetric and therefore independent of ϕ . Equation (2.31) can be separated into contributions from the sky and the ground, where the ground contribution is a polarisation dependent process. Thus

$$N(f, \theta, \phi | \hat{\mathbf{r}}_0) = \begin{cases} T_b^{sky}(f, \theta') P(f, \theta, \phi), & \theta' \in [0, \pi/2] \\ T_{b\parallel}(f, \theta') P_{\parallel}(f, \theta, \phi) + T_{b\perp}(f, \theta') P_{\perp}(f, \theta, \phi), & \theta' \in [\pi/2, \pi]. \end{cases} \quad (2.32)$$

The contribution from the sky is calculated as

$$T_b^{sky}(f, \theta') = T_{bo}(f) e^{-\tau_{f, \theta'}(0, s_a)} + \int_0^{s_a} \frac{\kappa_a(f, z') T(z') e^{-\tau_{f, \theta'}(0, z')}}{\sqrt{1 - (\sin \theta' / (1 + (z'/r_e)))^2}} dz' \quad (2.33)$$

which includes the effects of absorption by water vapor and oxygen as

$$\kappa_a(f, z) = \kappa_{H_2O}(f, z) + \kappa_{O_2}(f, z) \quad (2.34)$$

and where atmospheric variations in pressure and temperature with altitude are implicitly included from the z -variation in (2.33). The background brightness temperature $T_{bo}(f)$ consists of emission from the cosmic microwave background (CMB) and a directional averaged emission from the galaxy, so

$$T_{bo}(f) = T_{CMB} + T_{go}(f_0/f)^\beta \quad (2.35)$$

where $T_{CMB} = 2.73$ K, $T_{go} = 20$ K, $f_0 = 408$ MHz and $\beta = 2.75$, as suggested in [29]. The opacity of the medium, compensated for a curved earth, is calculated as

$$\tau_{f,\theta'}(0, z) = \frac{1}{\sqrt{1 - (\sin \theta' / (1 + (s_a/r_e)))^2}} \int_0^z \kappa_a(f, \zeta) d\zeta \quad (2.36)$$

with the integral taken over the path length through the atmosphere at the angle θ' . As in [28], a curved earth model with an earth radius of $r_e = 6370.95$ Km and an atmosphere height of $s_a = 100$ Km is assumed. Any convenient standard atmospheric temperature profile $T(z)$ can be used as well as for the pressure $\kappa_a(f, z)$. In order to speed up the calculation, interpolants were extracted for the sky temperature, as was done in [29]. The polarisation dependence of the ground temperature contribution due to scattering and emission is expanded as

$$\begin{aligned} T_{b\parallel}(f, \theta') &= T_{\parallel}^{sky} + T_{\parallel}^{gnd} \\ &= \Gamma_{\parallel}(\theta_1) T_b^{sky}(f, \theta_1) + [1 - \Gamma_{\parallel}(\theta_1) T_{gnd}] \\ T_{b\perp}(f, \theta') &= T_{\perp}^{sky} + T_{\perp}^{gnd} \\ &= \Gamma_{\perp}(\theta_1) T_b^{sky}(f, \theta_1) + [1 - \Gamma_{\perp}(\theta_1) T_{gnd}] \end{aligned} \quad (2.37)$$

where $\theta_1 = \pi - \theta'$, and the reflection coefficients are

$$\begin{aligned} \Gamma_{\parallel}(\theta_1) &= \left| \frac{\cos \theta_1 - \sqrt{\epsilon_2 - \sin^2 \theta_1}}{\cos \theta_1 + \sqrt{\epsilon_2 - \sin^2 \theta_1}} \right|^2 \\ \Gamma_{\perp}(\theta_1) &= \left| \frac{\epsilon_2 \cos \theta_1 - \sqrt{\epsilon_2 - \sin^2 \theta_1}}{\epsilon_2 \cos \theta_1 + \sqrt{\epsilon_2 - \sin^2 \theta_1}} \right|^2 \end{aligned} \quad (2.38)$$

with $\epsilon_2 \approx 3.5$ for dry land. Here, \parallel and \perp refer to the parallel and perpendicular polarisations with respect to the plane of incidence at the surface interaction. The ground temperature is assumed to be $T_{gnd} = 270$ K. The simplification of the brightness temperature model, presented as Model 3 in [28], is valid for unpolarised sources and a high-gain antenna not pointing at the ground. A polarisation-averaged reflection coefficient is defined as

$$\bar{\Gamma}(\theta_1) = \frac{\Gamma_{\parallel}(\theta_1) + \Gamma_{\perp}(\theta_1)}{2} \quad (2.39)$$

which simplifies (2.31) to

$$N(\dots) = \begin{cases} T_b^{sky} P, & \theta' \in [0, \pi/2] \\ \left[(1 - \bar{\Gamma}) T_{gnd} + \bar{\Gamma} T_b^{sky} \right] P, & \theta' \in [\pi/2, \pi] \end{cases} \quad (2.40)$$

where the frequency and angular dependencies are understood to be similar as in (2.31).

Main Reflector Masking

Imbriale suggested an approximation method for rapid calculation of the antenna noise temperature of offset Gregorian reflector systems in [30] which was refined in [28]. The idea consists of removing the main reflector from the calculation domain. Since the main reflector is electrically large, its removal significantly speeds up the calculation time. This approximation method assumes that all the energy scattered towards the main reflector is reflected into the main beam and thus towards the cold sky. Figure 2.6 from [28] illustrates the radiation patterns of the full system in 2.6a) compared to the pattern when only the feed and subreflector is included in the calculation domain in 2.6b).

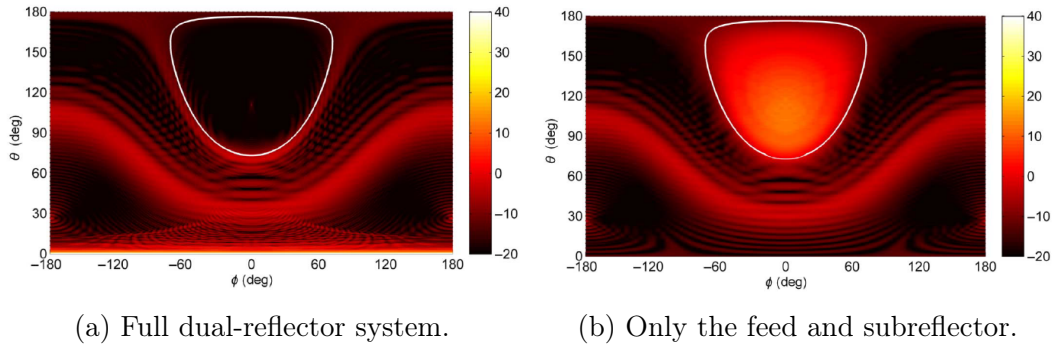


Figure 2.6: Radiation patterns in dBi at 1.5 GHz. The region inside the white line corresponds to the main reflector region. SOURCE: Figures 5 and 6, p. 1567 [28].

Note that the radiation behind the main reflector is not suppressed in Figure 2.6b) and also that the main beam in Figure 2.6a) around $\theta = 0^\circ$ is missing. Figure 2.7 shows the brightness temperature distribution when using Model 3 from [28]. Since multiplication of the brightness temperature distribution with the radiation pattern of Figure 2.6b) will force the fields in the main reflector region to zero, it gives a good approximation to the fields shown in Figure 2.6a). Note that this is a far-field approximation, even though the main reflector is normally in the near field of the subreflector.

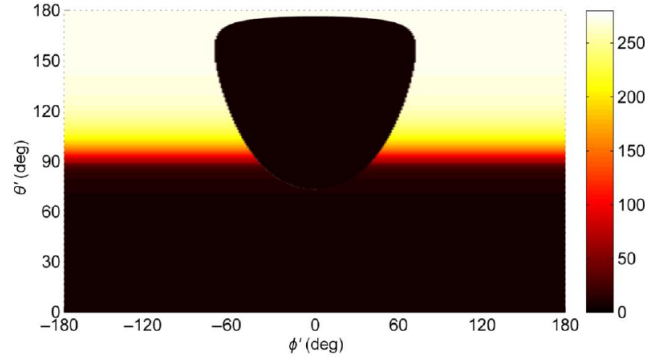


Figure 2.7: Brightness temperature distribution in K for the main reflector masking approximation when pointing at zenith. SOURCE: Figure 7, p. 1567 [28].

The accuracy of this approximation method can be further improved by taking edge diffraction effects into account. This is important when the electrical size of the system is reduced, as illustrated by the radiation pattern in Figure 2.8 which is at 500 MHz and where an increase in the energy density behind the main reflector can be seen. This happens as a result of edge diffraction from the main reflector, which causes energy to be spilled towards its shadow side that is typically pointed towards the hot ground. Thus, the approximation that all the energy in the main reflector region is reflected towards the main beam which points at the cold sky, becomes invalid.

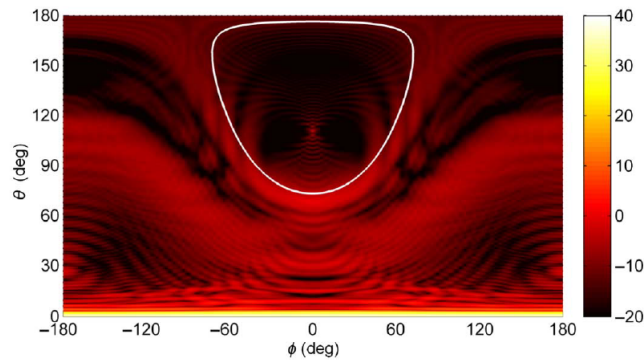


Figure 2.8: Radiation patterns in dBi at 500 MHz. The region inside the white line corresponds to the main reflector region. SOURCE: Figure 8, p. 1568 [28].

Since the main reflector is omitted in the simulation, information about the diffracted energy is not available. In [28], this is compensated for in an average sense by defining a correction factor $\alpha(f, \theta_p) \in [0, 1]$, which is a small positive number that allows some of the brightness temperature distribution from the hot ground behind the main reflector to be added to the approximate

masked model where it is assumed that the energy reflected towards the main reflector will be reflected into the main beam and thus towards the cold sky. The derivation to follow, from [28], shows that in order to find α , a solution for the antenna noise temperature T_A is required. Since this is not available, T_A is evaluated at a few frequency points only, after which an approximate solution for α is formulated.

The effective brightness temperature $T^\alpha(f, \theta_p)$ for all the energy which propagates towards the main reflector mask, can be defined as

$$T^\alpha = [1 - \alpha(f, \theta_p)]T^r + \alpha(f, \theta_p)\bar{T}^d \quad (2.41)$$

with

$$\bar{T}^d = \frac{T_{\parallel}^d + T_{\perp}^d}{2}. \quad (2.42)$$

T^d is the approximate brightness temperature behind the main reflector

$$T_{\parallel}^d(f, \theta_p) = T_{b\parallel}(f, \theta_d) \quad (2.43)$$

$$T_{\perp}^d(f, \theta_p) = T_{b\perp}(f, \theta_d) \quad (2.44)$$

with θ_p the tipping angle and $\theta_d = \theta_p + \pi$, and T^r is the brightness temperature in the direction of the main beam, i.e.

$$T^r(f, \theta_p) = T_b^{sky}(f, \theta_p). \quad (2.45)$$

Equation (2.32) can be separated to account for the masked and unmasked region as

$$N = P[MT^\alpha + WT_b] \quad (2.46)$$

where the frequency and angular dependence is implied and M indicates the masked region, so

$$M(\theta, \phi) = \begin{cases} 1, & \text{inside main reflector mask} \\ 0, & \text{outside main reflector mask} \end{cases} \quad (2.47)$$

and $W(\theta, \phi) = 1 - M(\theta, \phi)$. As before in equation (2.40)

$$T_b = \begin{cases} T_b^{sky}, & \theta' \in [0, \pi/2] \\ [(1 - \bar{\Gamma})T_{gnd} + \bar{\Gamma}T_b^{sky}], & \theta' \in [\pi/2, \pi]. \end{cases} \quad (2.48)$$

Substituting equation (2.41) into (2.46) gives

$$N = P[MT^\alpha = [1 - \alpha(f, \theta_p)]T^r + \alpha(f, \theta_p)\bar{T}^d + WT_b] \quad (2.49)$$

which can then be substituted into equation (2.30). From this a solution for α is found as

$$\alpha(f, \theta_p) = \frac{T_A I_t - I_w - I_r}{I_d - I_r} \quad (2.50)$$

where

$$\begin{aligned}
 I_t(f, \theta_p) &= \iint_{4\pi} P \sin \theta d\theta d\phi \\
 I_w(f, \theta_p) &= \iint_{4\pi} W P T_b \sin \theta d\theta d\phi \\
 I_r(f, \theta_p) &= \iint_{4\pi} M P T^r \sin \theta d\theta d\phi \\
 I_d(f, \theta_p) &= \iint_{4\pi} M P \bar{T}^d \sin \theta d\theta d\phi.
 \end{aligned} \tag{2.51}$$

As noted above, equation (2.50) is evaluated at a few frequency points only in order to find an approximation for α . In [28], T_A is evaluated at the lowest frequency point of interest f_1 , thereby minimising the calculation time. An approximate solution $\alpha'(f, \theta_p) \approx \alpha(f, \theta_p)$ is then found by letting

$$\alpha'(f, \theta_p) = \alpha(f_1, \theta_p) \left(\frac{f_1}{f} \right) \tag{2.52}$$

with f_1 chosen as the lowest frequency point of interest. An improvement to this approximation method is introduced in [31] where three frequency points are used to give an approximation α''' . The frequency points are chosen at the beginning, middle and end of the frequency band. Then

$$\alpha'''(f, \theta_p) = \alpha(f_1, \theta_p) \left(\frac{f_1}{f} \right)^{n(f)}, \tag{2.53}$$

with

$$n(f) = \frac{n_1 - n_2}{f_2 - f_3} f + \frac{f_2 n_2 - f_3 n_1}{f_2 - f_3}, \tag{2.54}$$

where

$$n_1 = \frac{\log \left(\frac{\alpha(f_2, \theta_p)}{\alpha(f_1, \theta_p)} \right)}{\log \left(\frac{f_1}{f_2} \right)} \tag{2.55}$$

and

$$n_2 = \frac{\log \left(\frac{\alpha(f_3, \theta_p)}{\alpha(f_1, \theta_p)} \right)}{\log \left(\frac{f_1}{f_3} \right)}. \tag{2.56}$$

Thus, α''' is found from the calculation of T_A at three frequency points f_1, f_2 and f_3 , which is then used in (2.41) for the effective brightness temperature in the masked region M , and then N is calculated from equation (2.46) in order to find the approximated antenna noise temperature T_A''' from (2.30). Once again, note that in-house code was used to realise the above calculations.

Chapter 3

The Pyramidal Sinuous Antenna

3.1 Design Parameters

The log-periodic sinuous antenna was first introduced by DuHamel in 1987 [32]. Sinuous antennas are suitable for UWB applications, since they are frequency independent structures in the infinite size and self-complementary limits. The condition for a frequency independent antenna can be understood from the principle of frequency scaling which is used in model measurements, where a decrease in the model size of the antenna leads to a proportional increase in the operating frequency. For a wideband antenna, a structure that can be its own scale model is required [33]. This is done by removing any characteristic length of the antenna by specifying it in terms of angles only [34], leading to an infinite structure. Practically, a wideband antenna must be truncated with little effect on the radiation pattern over the operating bandwidth. The sinuous antenna can be specified by two angles, two dimensions and a scaling factor which determines the geometric progression of elements of a similar shape. Since its shape is not solely specified by angles, it is not truly frequency independent. Rather, its radiation characteristics, such as the impedance, pattern, directivity, beamwidth and sidelobe levels, vary periodically with the logarithm of frequency [18]. The antenna can be designed to make these variations sufficiently small, resulting in a wideband antenna.

The sinuous curve is defined by

$$\phi(r) = (-1)^P \alpha \sin \frac{\pi \ln \frac{r}{r_P}}{\ln \tau} \quad (3.1)$$

with ϕ and r the spherical coordinates of any point along the curve. The angular width of the curve is defined by α . The curve is then rotated by $\pm\delta$ to form the sinuous arm illustrated in Figure 3.1. The arm is then rotated in $360/N$ degree increments to form an N -arm antenna, each consisting of P

radiating cells. τ defines the growth rate from cell to cell, i.e. $\tau = r_p/r_{p+1}$. r_P is the maximum radius, which determines the antenna's low cut-off frequency.

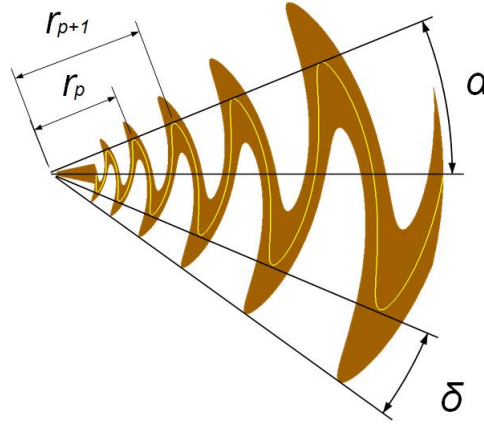


Figure 3.1: One arm of the sinuous antenna.

The radiation characteristics are periodic, where two frequencies that are a period apart are related by [18]:

$$\tau = \frac{f_1}{f_2} \quad (3.2)$$

where $f_2 > f_1$. Practically, all log-periodic type antennas display finite bandwidth performance with degradation at the band edges due to physical truncation of the structure. This is known as the "end effect". The antenna should be designed so that there exists three regions, the definitions of which can be found in [35]:

- The Transmission-Line Region: In this region the elements do not radiate, since its size is much smaller than the wavelength at a frequency f . These elements function as a transmission line.
- The Active Region: This is the region where the elements radiate at a frequency f . The active region passes from the shorter to the longer elements as the frequency decreases.
- The Stop Region: This is the region after the active region where the elements do not radiate at a frequency f , even though its size is comparable to the wavelength at that frequency. The current on the elements in the stop region vanishes, since the current passed through the previous element and the current induced by mutual couplings from the active radiating elements are of the same amplitude and 180° out of phase [36]. The effect of these elements on the radiation pattern and reflection coefficient should be as low as possible.

The active region at a frequency f , corresponding to a wavelength λ , is where the path length is equal to $\lambda/2$ [18]. This occurs where

$$r(\alpha + \delta) = \lambda/4. \quad (3.3)$$

The minimum and maximum values of the projected radius r_1 and r_P (where P is the total number of sinuous cells) can thus be derived, determined from the required bandwidth as

$$r_1 = \frac{\lambda_H}{8(\alpha + \delta)} \quad (3.4)$$

and

$$r_P = \frac{1.2\lambda_L}{4(\alpha + \delta)} \quad (3.5)$$

with λ_H and λ_L the respective wavelengths at the high and low cut-off frequencies. These values ensure that the end effects are small.

Mushiake [37] has shown that an antenna that is a self-complementary structure has a constant input impedance that is independent of the frequency and shape of the structure. A self-complementary structure is one that remains unchanged when the metallic and dielectric parts are interchanged. The planar self-complementary antenna from [32], shown in Figure 3.2, has a constant beamwidth, fixed phase center, constant input impedance, low loss and dual uncoupled orthogonal senses of linear polarisation.

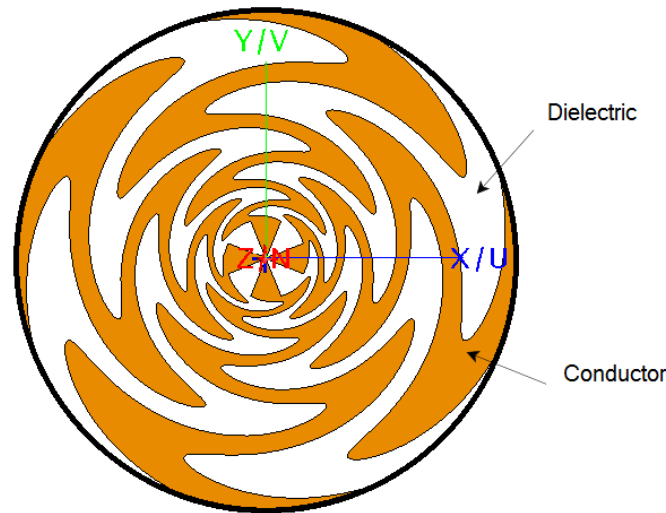


Figure 3.2: A self-complementary planar sinuous antenna.

The input impedance of one arm of the planar self-complementary sinuous antenna with respect to ground was given by Deschamps [38] as

$$Z_m = \frac{30\pi}{\sin\left(\frac{180m}{N}\right)} \quad (3.6)$$

where m is the excitation mode and N is the number of arms. The planar sinuous antenna gives a bi-directional radiation pattern. The requirement for a self-complementary antenna is that $2\delta + \alpha = \pi/2$ [39]. In addition, for an N -arm sinuous structure the requirement is $\delta = \pi/2N$ [32] and thus $\alpha = \pi/2 - \pi/N$. Design procedures are often relatively simple in that the only parameters involved are the truncation sizes which controls the bandwidth, since all the angles are fixed to provide a self-complementary structure. When the self-complementary constraint is relaxed, uni-directional radiation patterns may be achieved. Projecting the sinuous antenna onto a suitable geometry, such as a cone or pyramid, allows it to be used as a wideband reflector antenna feed, where the addition of a ground plane ensures a stable phase center in addition to a relatively frequency stable uni-directional radiation pattern [12], [40]. The cost of this relaxation is increased design complexity, since typically all the angular and truncation parameters of the antenna now become free design variables.

In this thesis the focus is on a 4-arm structure mounted onto a square pyramid over a ground plane which forms the pyramidal sinuous antenna shown in Figure 3.3. θ defines the angle of the pyramid's elevation and h the distance to the ground plane. A realistic feeding network is not considered, since the added layer of complexity is beyond the scope of this thesis, therefore an ideal feed port is used in all simulations.

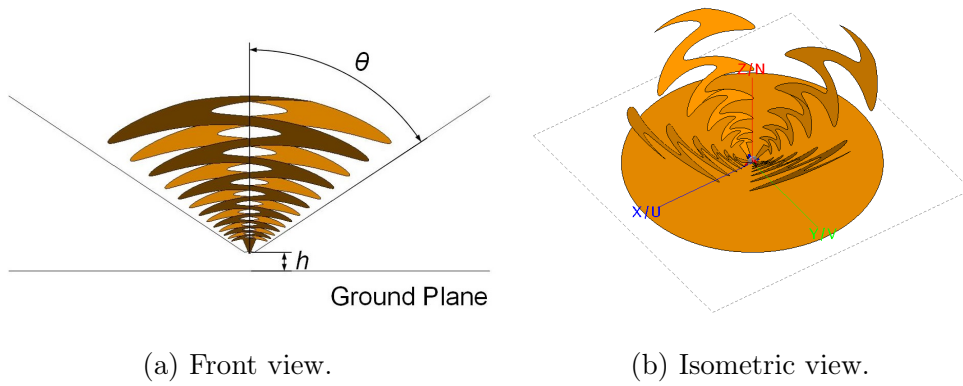


Figure 3.3: The pyramidal sinuous antenna.

The 4-arm antenna allows two orthogonal senses of polarisation on each opposing pairs of arms [39]. If the cross-polarisation is sufficiently low, the

antenna allows separate reception or transmission of each polarisation. Table 3.1 lists the design parameters of the antenna.

Table 3.1: Design parameters for the pyramidal sinuous antenna.

Design Parameters	
τ	Growth rate ratio
α	Angular width of sinuous curve
δ	Rotation angle
θ	Elevation angle of pyramid
h	Distance between the arms and ground plane

3.2 Design Objectives

Sensitivity

As noted previously, often the main objective in the design of a radio interferometer such as the SKA, is to maximise the receiving sensitivity. Doing so can lead to huge cost savings, while still maintaining system performance. Since optimisation of antenna systems over a large parameter space becomes computationally prohibitively expensive when using full wave electromagnetic solvers, a simple method to approximate the average sensitivity as a function of the geometrical input parameters is presented in Chapter 4. This method is broken down into three different models of varying computational cost. In engineering design problems, it is often the case that optimising different performance metrics simultaneously leads to a trade-off in the design. Since maximisation of the receiving sensitivity is of the utmost importance in this case, bounds can be placed on the rest of the performance metrics which provides a minimally acceptable design. The complexity of the design increases along with the number of simultaneous conditions that must be met. In this thesis only one other performance metric is considered, namely the reflection coefficient of the feed.

Reflection Coefficient

In transmit mode the reflection coefficient of an antenna provides a measure of how much of the power that is transmitted from a port is reflected back into that port, caused by a mismatch of the impedance between the antenna and the feeding network. Since the input impedance of the wideband pyramidal sinuous antenna to be considered varies over frequency, it becomes difficult to

match it to the feeding network over the entire band. The reflection coefficient in decibels (dB) is calculated from the impedance of the antenna as follows:

$$S_{11}(f) = 20 \log \left(\frac{Z(f) - Z_0}{Z(f) + Z_0} \right) \quad (3.7)$$

with the input impedance taken as $Z_0 = 267 \, \Omega$. This value is chosen from Deschamps' formula in (3.6), in other words, it is the value of the input impedance of two arms of a self-complementary sinuous antenna. As noted before, relaxation of the self-complementary constraint leads to variation in the input impedance of the antenna as a function of frequency. For an acceptable design, a maximum cut-off value of -10 dB is specified for the reflection coefficient of the antenna, which corresponds to 10% of the transmitted power being reflected back into the port. For different geometries, the value of Z_0 that provides the optimal reflection coefficient over the entire band will vary. However, since the specific value of Z_0 which accomplishes this is not available when accurate values for $Z(f)$ are only available over a sparse sample space, the constant value of $Z_0 = 267 \, \Omega$ is used for all geometries. Note however that after a specific design is chosen, the best input impedance value for that geometry can be found, leading to a possible improvement in the reflection coefficient of the chosen design.

To ensure that the maximum of $S_{11}(f)$ is below -10 dB, accurate values of $Z(f)$ is required over the entire band of interest. This is expensive to generate, thus a technique is sought which approximates $Z(f)$ with sufficient accuracy when using only a few full wave evaluations. For this purpose, use is made of rational interpolation methods, which is discussed in Chapter 5. Electromagnetic wave equations naturally lead to pole series in the frequency domain. This arises from complex-frequency resonances, however, the response is not necessarily described by pole terms alone, as discussed in [15]. A general rational function may be well-suited for fitting the input impedance of the antenna as a function of frequency, since it is related to the physics of the problem. In [15], the Padé rational function is used for curve fitting of various electromagnetic responses in the frequency domain. The extension of this technique to the spatial domain is presented in [16]. In [17], Thiele continued fractions are used along with an adaptive sampling technique to create accurate models of microwave circuits. An adaptive sampling algorithm achieves a specified model accuracy with a minimum number of interpolation points by iteratively choosing each consecutive sample point at the point of maximum error, according to some predefined error function. In Chapter 5 of this work, the formulation of a rational function that is well-suited to the application at hand is presented. Sampling is done over a grid of interpolation points, however, it would be highly beneficial for this method to be extended for use in an adaptive sampling scheme.

For convenience, the design objects are summarised in Table 3.2.

Table 3.2: Design objectives.

Performance Metric	Objective
Reflection coefficient	A maximum value of -10 dB over the entire band.
Sensitivity	Maximise given the constraint on the reflection coefficient.

The design space to be explored is listed in Table 3.3. The distance of the antenna to the ground plane is kept constant at $h = 5$ mm throughout. This value was found in [40] to yield favourable results for the reflection coefficient.

Table 3.3: Input parameters for the design space exploration.

Parameter	Range
τ	0.75 - 0.9
δ/α	0.4 - 0.8
$\delta + \alpha$	28 - 44°
θ	47 - 59°

3.3 Coarse Model

Accurate simulations of the antenna requires a full wave computational electromagnetic (CEM) solver, such as FEKO [41]. In order to find an optimal design, exploration of a large parameter space over a wide frequency band is considered. This becomes very expensive in terms of time and computational complexity. Therefore, there is a need for a design strategy which speeds up the optimisation process. Surrogate based optimization (SBO) is used for this purpose, where a coarse model is sought that approximates the behaviour of the full fine model. The coarse model must be quicker to evaluate than the fine model. In this case it is based on the physical structure of the expensive fine model, so it provides information about it. The fine model is the full antenna over a 3:1 bandwidth, from 350 - 1050 MHz, with solutions found in FEKO. Since the sinuous antenna is a complicated structure, the coarse model also utilises solutions from FEKO. These are found from truncated antennas at the band edges over a 2:1 bandwidth. Thus, one antenna is truncated to operate from 350 - 700 MHz, while the other antenna is truncated to operate from 525 - 1050 MHz. In addition to operating over a narrower band, these models are electrically smaller, so the number of CEM unknowns are decreased as illustrated in Figure 3.4.

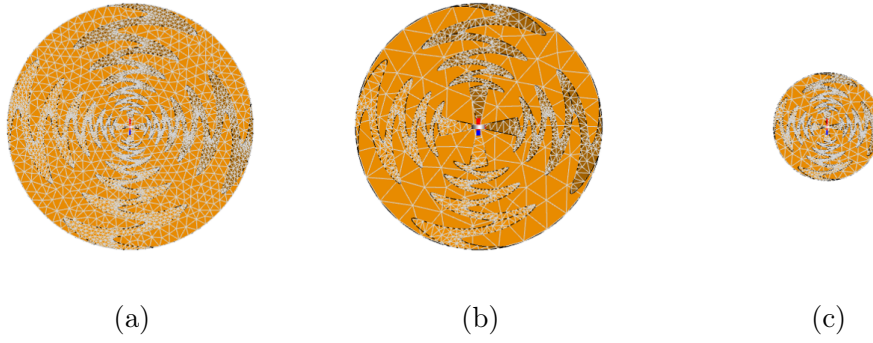


Figure 3.4: Illustration of the fine and coarse models used in FEKO simulations. (a) Fine model. (b) Coarse model at the low band edge. (c) Coarse model at the high band edge. Note that these coarse models are exaggerated for illustration purposes.

Reducing the coarse model bandwidth to lower than 2:1 causes significant end effects and make the models highly inaccurate. However, even these models introduce end effects which would not be present in the full fine model, as shown for the reflection coefficient in Figure 3.5. Thus, for the low band coarse model, the values from 525 - 700 MHz are highly inaccurate, similarly for the high band coarse model, the values from 525 - 787,5 MHz are unusable. This means that the coarse model only provides information at the band edges, however, a log-periodic behaviour is expected in between these edges.

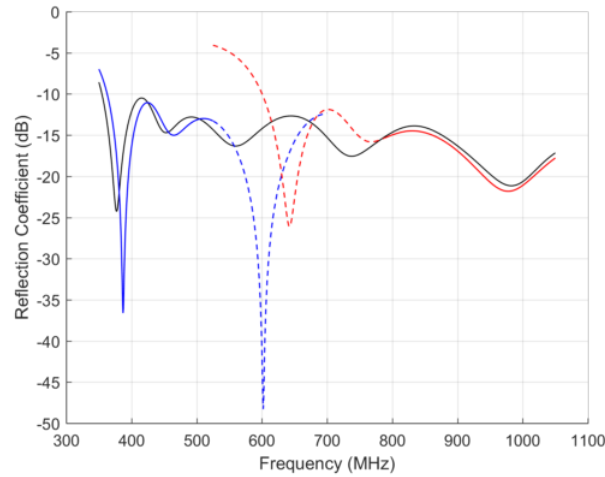


Figure 3.5: Figure illustrating the coarse model end effects. The black line is the fine model data. The blue line is the low band coarse model and the red line is the high band coarse model. The dashed parts of both models are not simulated as it contains end effects not present in the fine model.

Regarding the FEKO simulations, the Method-of-Moments solver was used in all cases. For the fine model, an adaptive solver was used to acquire an accurate solution, whereas for the low band coarse model, 36 frequency points were evaluated, linearly spaced over the band of interest from 350 - 525 MHz. The upper half of the band does not require simulation, since it does not represent the fine model behaviour. Similarly, the high band coarse model was evaluated at 53 frequency points, linearly spaced over the band from 790 - 1050 MHz.

The mesh sizes of the antenna was determined from a concurrent study in [42]. Since the inner cells of the antenna operate at higher frequencies than the outer cells, it is possible to use a coarser mesh for the outer cells. A transition boundary for the mesh sizes was placed at the radius of the active region at the geometrical mean frequency, giving by

$$f_{mean} = \sqrt{f_L f_H} \quad (3.8)$$

where f_L is the low cut-off frequency of 350 MHz and f_H is the high cut-off frequency of 1050 MHz. This results in $f_{mean} = 606.2$ MHz. This boundary was used in the fine model and the coarse models. For the inner conducting cells, a mesh element size of $\lambda_H/20$ was used and for the outer cells a mesh element size of $\lambda_H/16$ was used. For the ground plane, a coarser mesh element size of $\lambda_H/8$ was sufficient.

In addition to the models operating over a smaller bandwidth, the number of CEM unknowns are also decreased. The combined effect is that the two coarse models in combination requires less CPU time than the full fine model. A comparison of a representative sample is shown in Table 3.4. Here $\tau = 0.8, \delta = 22.5^\circ, \alpha = 13.5^\circ$ and $\theta = 53^\circ$.

Table 3.4: Comparison of fine and coarse models.

Model	Frequency (MHz)	Mesh (#triangles)	CPU time (hours)
Fine	350 - 1050	4716	15.985
Coarse (Low)	350 - 700	3677	1.275
Coarse (High)	525 - 1050	3553	2.890

Even for this modest bandwidth design a significant speed-up is observed for the coarse model evaluation - implying 4 coarse model samples can be obtained for each fine model sample. When the bandwidth of the fine model is increased this improvement factor rapidly grows since the number of CEM unknowns in the fine model scales with bandwidth squared, while the coarse model simulation time remains constant.

Chapter 4

Fast Parametric Modeling of the Sensitivity

In this chapter different simplifications which can be used to model the sensitivity of the antenna are considered. Surrogate based modelling is used for this purpose. The fine model radiation pattern of each antenna feed is found from FEKO. This is then imported into GRASP in order to find the full radiation pattern of the total reflector antenna system. The fine model for the sensitivity is then calculated as explained in Chapter 2, which corresponds to using equation (2.12) for the efficiency calculation and Model 3 from [28] for the calculation of the noise temperature where the main reflector is omitted from the calculation domain. A coarse model of the sensitivity is introduced that removes the need for the dish antenna system to be simulated and only requires integration of the antenna feed patterns. Three distinct surrogate models of the sensitivity are developed and compared.

4.1 Space Mapping

4.1.1 Overview

The goal is to find the optimal sensitivity over a large parameter space, namely the domain indicated in Table 3.3. Since accurate computation of the sensitivity at each point in the parameter space is expensive, space mapping (SM) is utilised as a design framework to find the surrogate models. SM was first introduced in 1994 by Bandler, et al. [43]. Since that time considerable research has been done to expand the method for various applications, for example, in the design of non-radiating microwave systems [44], [45], [46], radiating microwave systems [47], [48] and more recently in the design of reflector antenna systems [49], [50]. In the SM design framework, solutions from the low-fidelity (LF) coarse model is aligned to the high-fidelity (HF) fine model solution in sub-regions of the design space by using a suitable mapping. From this mapping a

surrogate is found which combines the fast simulation time of the coarse model to the accuracy contained in the fine model. Thus, design space exploration and optimisation can be done reasonably quickly with reasonable accuracy. Figure 4.1 illustrates the procedure. It is up to the designer to specify an acceptable level of accuracy and design time. Note that there are several forms of the SM framework that can be applied, including input SM, output SM, implicit SM, and a combination of these. The general concepts of the output SM framework follow. Thereafter, 3 different models of varying complexity and cost are introduced which the designer can choose from in order to explore the sensitivity of the system.

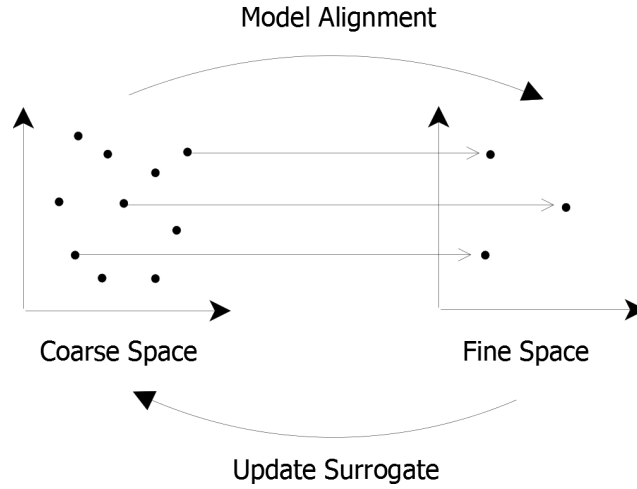


Figure 4.1: Illustration of the space mapping procedure.

4.1.2 Design Framework for Output Space Mapping

Output SM applies a correction term to the coarse model in order to find a surrogate which matches perfectly at the available fine model points. This correction factor can be multiplicative or additive. In this case the surrogate is found by adding a polynomial regression function to the coarse model.

Let $\mathbf{R}_f : X_f \rightarrow \mathbb{R}^m, X_f \subseteq \mathbb{R}^n$ denote the response vector of the fine model and $\mathbf{R}_c : X_c \rightarrow \mathbb{R}^m, X_c \subseteq \mathbb{R}^n$ denote the response vector of the coarse model, where \mathbb{R} is the set of real numbers. Then the goal is to solve

$$\mathbf{x}_f^* = \arg \min_{\mathbf{x} \in X_f} U(\mathbf{R}_f(\mathbf{x})) \quad (4.1)$$

where U is an objective function. Since many coarse model evaluations are normally available compared to the number of fine model evaluations, a surrogate is constructed from

$$R_s = R_c(\mathbf{x}) + r(\mathbf{x}) \quad (4.2)$$

where \mathbf{x} is a vector of the design parameters. The procedure in [51] is followed, where the correction term $r(\mathbf{x})$ is found by fitting a second order polynomial regression term on the residuals of the coarse and fine models, sampled over a star distribution from the full parameter space. Thus there is a training set \mathbf{x}_i where fine model evaluations are available and

$$r_i(\mathbf{x}_i) = R_f(\mathbf{x}_i) - R_c(\mathbf{x}_i), \quad (4.3)$$

with

$$r(\mathbf{x}) = a_0 + \sum_{n=1}^N [a_n x_n + b_n x_n^2] \quad (4.4)$$

trained in a least squares sense on \mathbf{x}_i to find the coefficient vectors \mathbf{a} and \mathbf{b} . The regression model $r(\mathbf{x})$ assumes independent input variables. In order to include coupled variables, the number of samples from the fine model would need to be increased.

4.1.3 "The 5% Problem"

An important aspect to consider when constructing different surrogate models is the choice of error function to be used for evaluating the model accuracy. There are two categories of error functions, namely absolute and relative. Engineers normally prefer relative errors over absolute errors, since it is unit-free and thus more intuitive to interpret. It is often simply stated that the required model accuracy is 5%, however, in practice this is not always straightforward to implement. This has become known as "the 5% problem", which Gorissen, et al. discussed in length in [52]. Care must be taken when interpreting a value like "5% percent", since different error functions have different characteristics, and even though a relative error is unit-free, it is not context-free. Lin [53] also noted that an error value on its own cannot necessarily give information about how well a model is performing - error functions can, however, be used to compare the accuracy of different models. A discussion of a few of the options which are available for the choice of error function follows, which highlights some advantages and disadvantages of each.

Absolute Errors

The most popular absolute error measure is the Root Mean Squared Error, defined as

$$\text{RMSE}(y, \tilde{y}) = \sqrt{\frac{\sum_{i=1}^n (y_i - \tilde{y}_i)^2}{n}} \quad (4.5)$$

where y_i is the real response value, \tilde{y}_i is the predicted response value from the surrogate model and n is the number of response values which are available. The RMSE is one \sqrt{n} -th of the true arithmetic average euclidean distance

between the prediction \tilde{y} and the true value y , thus the Average Euclidean Error is preferred, defined as

$$\text{AEE}(y, \tilde{y}) = \frac{1}{n} \sum_{i=1}^n \sqrt{(y_i - \tilde{y}_i)^2}. \quad (4.6)$$

Both the RMSE and the AEE are known as pessimistic error functions, since large errors are penalised severely, while small errors are virtually ignored. This is the main disadvantage of their use. The advantage of their use is that they are simple to interpret. Average errors can often be misleading, since there may be areas where the prediction is very poor. Thus it is useful to specify the maximum absolute error, i.e.

$$\text{MAX}(y, \tilde{y}) = \max |y_i - \tilde{y}_i| \quad i = 1, \dots, n. \quad (4.7)$$

For design space exploration purposes, average errors are useful since it gives an idea of the overall accuracy of the model. When optimisation is the goal, the maximum error may give a better idea of the local accuracy of the model.

Relative Errors

Relative errors are often preferred, since they are unit-free and thus seemingly easier to interpret. The Average Relative Error is defined as

$$\text{ARE}(y, \tilde{y}) = \frac{1}{n} \sum_{i=1}^n \frac{|y_i - \tilde{y}_i|}{|y_i|} \quad (4.8)$$

and the corresponding Maximum Relative Error is

$$\text{MRE}(y, \tilde{y}) = \max \left(\frac{|y_i - \tilde{y}_i|}{|y_i|} \right) \quad i = 1, \dots, n. \quad (4.9)$$

Note that if y_i is very small then the ARE will tend to infinity, giving a biased result. In these cases the ARE should not be used. Another option is the Root Relative Squared Error, defined as

$$\text{RRSE}(y, \tilde{y}) = \sqrt{\frac{\sum_{i=1}^n (y_i - \tilde{y}_i)^2}{\sum_{i=1}^n (y_i - \bar{y})^2}} \quad (4.10)$$

where \bar{y} is the mean over all true values y . The RRSE gives a measure of how much better a model fits the data when compared to the mean. In this chapter, the ARE and the MRE are used to compare the different models. In [52] it was noted that the only true, unbiased way to assess the accuracy of a model is to compare it with a very dense test set of expensive data, however, this is not always readily available. The figures shown in the next section can be used along with these error metrics to give insight into each model's accuracy.

4.2 Simplifications to the Surrogate Model for Sensitivity Calculations

In this section, the three different surrogate models are described that model the sensitivity. Table 4.1 gives an overview of the differences between the models, as well as that of the fine model.

Table 4.1: Overview of the difference between the different surrogate models.

Model	Radiation Pattern	Sensitivity	Surrogate
Fine	Full antenna.	Calculated in GRASP with main reflector masking technique.	N.A.
1	N.A.	N.A.	Fits a polynomial to a star distribution of the fine model.
2	Full antenna.	Approximate calculation from equation (4.12).	Fits a polynomial as correction term over a star distribution of the difference between the coarse and fine models.
3	Truncated antennas at the band edges.	Approximate calculation from equation (4.12).	Fits a polynomial as correction term over a star distribution of the difference between the coarse and fine models.

Model 1

For Model 1, a surrogate is produced by applying a functional approximation directly to the fine model data. Thus no coarse model is evaluated for Model 1. A polynomial is applied to a star distribution of the fine model data, thus

$$R_s = a_0 + \sum_{n=1}^N [a_n x_n + b_n x_n^2] \quad (4.11)$$

where \mathbf{a} and \mathbf{b} are found from training the surrogate in a least squares sense over the function values $R_f(\mathbf{x}_i)$. The design parameters are $\mathbf{x} = [\tau, \delta/\alpha, \alpha + \delta, \theta]^T$. When only one parameter is varied, at least 3 fine model evaluations are required. Three different objective functions $U^{(a)}$, $U^{(b)}$ and $U^{(c)}$ are considered. In each case the average sensitivity over variations of the tipping angle are first found and then the objective functions to be considered are

- a) the average over frequencies larger than 650 MHz,
- b) the average over the entire frequency band and
- c) the worst case over frequency, i.e. the minimum sensitivity over the entire band.

Figure 4.2 indicates why $U^{(a)}$ is chosen as the average over frequencies larger than 650 MHz. It is seen that the sensitivity decreases rapidly for frequencies smaller than this value. This happens as a result of increased sky noise at the low frequency end caused by the inverse relation in equation (2.35). Since the sky noise dominates at these frequencies, variations in the antenna radiation pattern due to geometric parameter variations no longer leads to significant changes in sensitivity. Including these values in the calculation of the average sensitivity will flatten the resulting average values, thus making optimisation more difficult. It is thus preferred to discard these values. Surrogate models were built for $U^{(a)}$, $U^{(b)}$ and $U^{(c)}$, however, since $U^{(a)}$ is used for further design purposes, its results are presented here, with the results for $U^{(b)}$ and $U^{(c)}$ included in Appendix A. Figure 4.3 shows the results for Model 1.

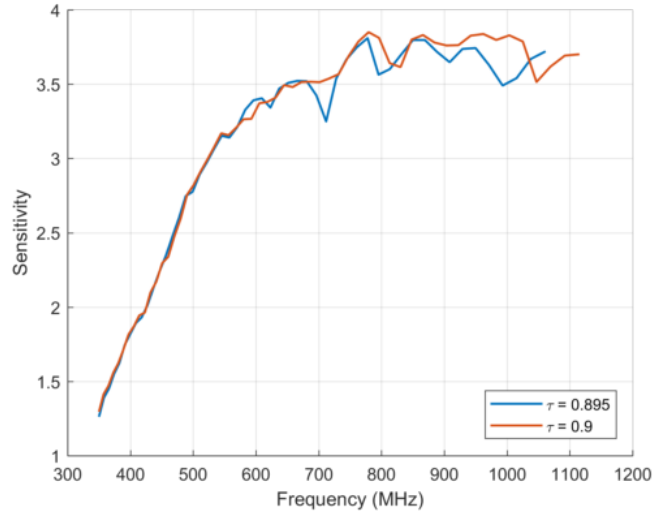


Figure 4.2: Sensitivity as a function of frequency for two different geometries.

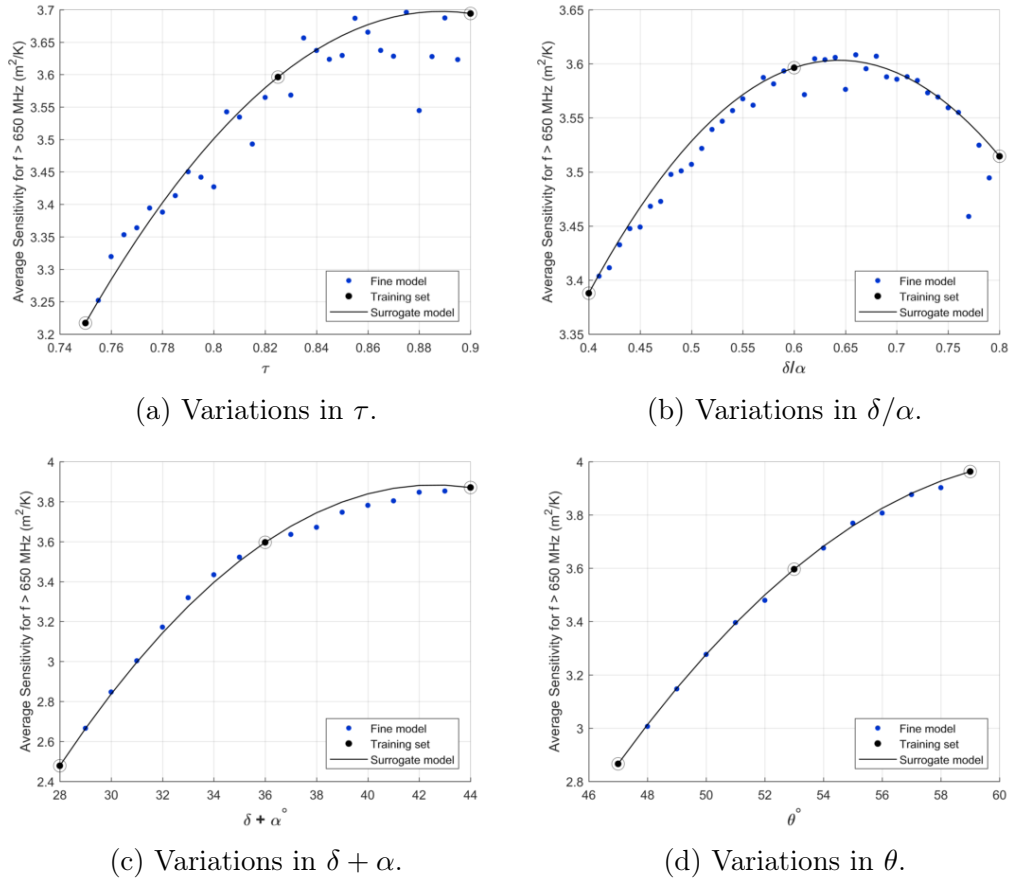


Figure 4.3: Sensitivity surrogates for Model 1.

The ARE and MRE of each model is listed in Table 4.2 and the total number of fine model points which were evaluated for each parameter over the entire band is listed in Table 4.3.

Table 4.2: Percentage errors for Model 1.

Parameter	ARE [%]	MRE [%]
τ	0.86	4.26
δ/α	0.30	2.50
$\delta + \alpha$	0.81	1.97
θ	0.20	0.63

Table 4.3: Number of fine model points required for Model 1.

Parameter	#points
τ	108
δ/α	93
$\delta + \alpha$	93
θ	93

Model 2

Model 2 makes use of a coarse model for the sensitivity calculation. The radiation pattern from the feed is once again calculated from the full fine model of the pyramidal sinuous antenna. So

$$\text{Sensitivity}_c(\mathbf{x}) = \frac{(\eta_{ap})_c A_{ph}}{(T_{sys})_c}(\mathbf{x}) \quad (4.12)$$

where once again $\mathbf{x} = [\tau, \delta/\alpha, \alpha + \delta, \theta]^T$ and the same objective functions as in Model 1 are considered. Here $(\eta_{ap})_c$ makes use of the GO approximation from equation (2.13), but with the diffraction efficiency ignored, i.e.

$$(\eta_{ap})_c = \eta_{BOR1} \eta_{sp} \eta_{ill} \eta_{ph} \eta_{pol}, \quad (4.13)$$

with all sub-efficiencies as explained in Section 2.3 and the system noise temperature is approximated as

$$(T_{sys})_c = \eta_{sp}(T_{sky})_c + (1 - \eta_{sp})(T_{gnd})_c \quad (4.14)$$

with

$$(T_{sky})_c = T_{CMB} + T_{go}(f_0/f)^\beta \quad (4.15)$$

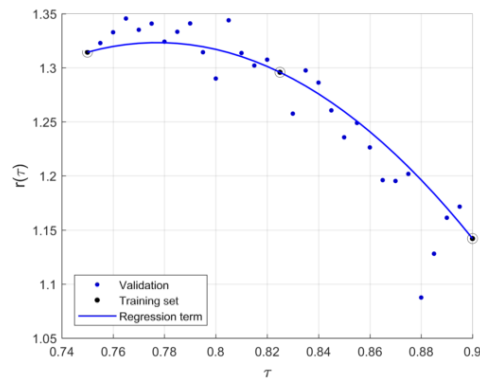
where, as before, $T_{CMB} = 2.73$ K, $T_{go} = 20$ K, $f_0 = 408$ MHz and $\beta = 2.75$, and

$$(T_{gnd})_c = 270 \text{ K}. \quad (4.16)$$

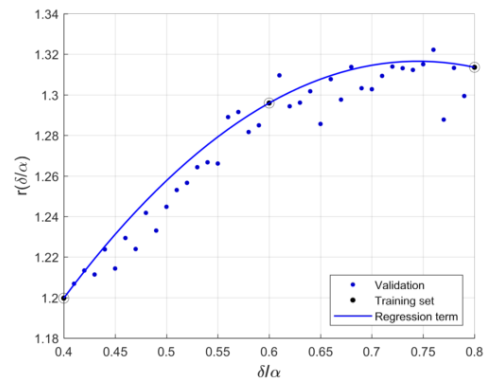
The surrogate is found as explained in Section 4.1.2 by evaluation of the difference of the coarse and fine model points over a star distribution for each parameter (in other words, 3 points are required when only one parameter is varied) and then a second order polynomial regression term is fitted through it, to be used as a correction factor. So

$$\text{Sensitivity}_s(\mathbf{x}) = \text{Sensitivity}_c(\mathbf{x}) + r(\mathbf{x}), \quad (4.17)$$

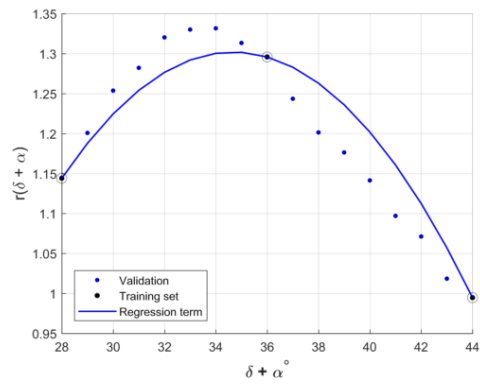
with $r(\mathbf{x})$ found as in equation (4.4). The regression terms for Model 2 are shown in Figure 4.4 and surrogates are shown in Figure 4.5.



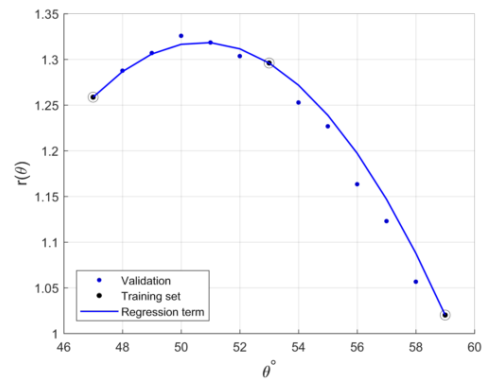
(a) Variations in τ .



(b) Variations in δ/α .



(c) Variations in $\delta + \alpha$.



(d) Variations in θ .

Figure 4.4: Regression terms for Model 2.

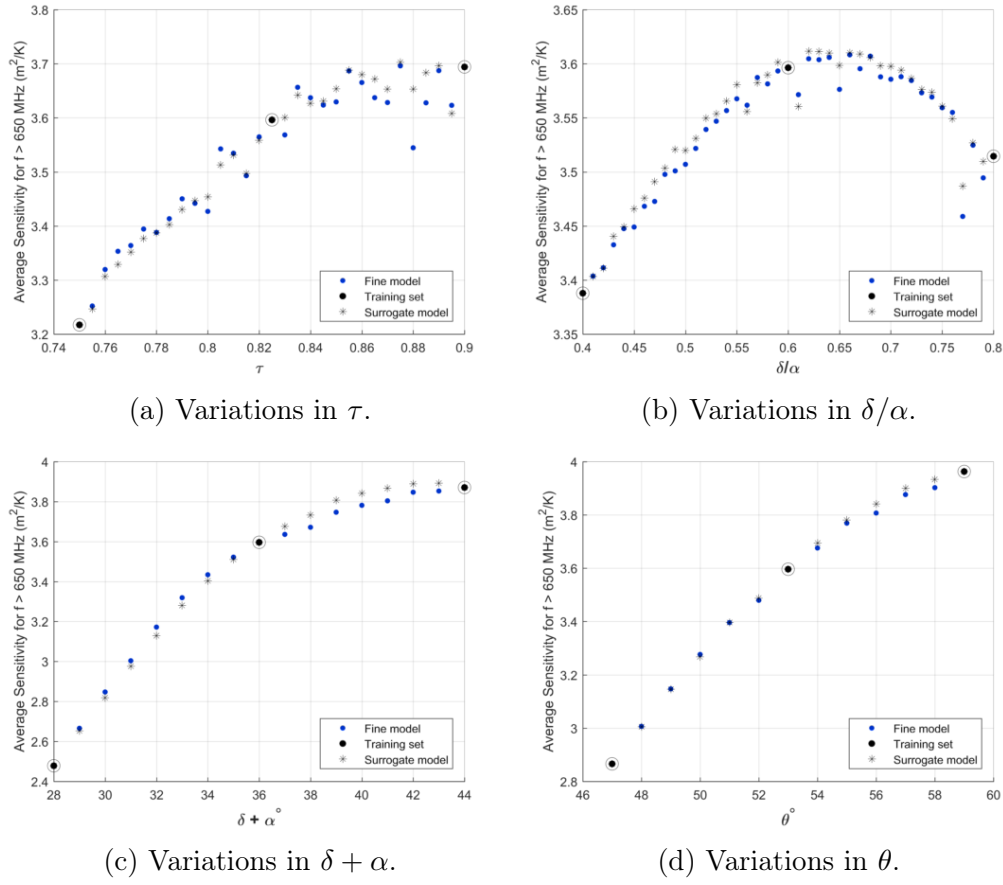


Figure 4.5: Sensitivity surrogates for Model 2.

Note that the surrogate is only available where coarse model evaluations were done. Table 4.4 lists the error values for Model 2 and Table 4.5 indicates the number of fine and coarse model points which were evaluated.

Table 4.4: Percentage errors for Model 2.

Parameter	ARE [%]	MRE [%]
τ	0.49	3.07
δ/α	0.33	0.81
$\delta + \alpha$	0.94	1.68
θ	0.29	0.89

Table 4.5: Number of points required for Model 2.

Parameter	# fine points	# coarse points
τ	108	1066
δ/α	93	1271
$\delta + \alpha$	93	527
θ	93	403

Model 3

Model 3 makes use of the same surrogate model as described for Model 2, but in this case the radiation patterns are found by simulating the coarse models at the band edges in FEKO as described in Section 3.3. Since $U^{(a)}$ is found by calculating the average for frequencies larger than 650 MHz and the low band coarse model is only available up to 525 MHz, in this case only the high band coarse model feed radiation patterns are required and these averages are calculated for frequencies higher than 787,5 MHz, where the data from these models are valid. The polynomial regression function is found from evaluating the difference between the coarse and fine sensitivity models at 3 points for each parameter variation. Figure 4.6 shows the results for Model 3.

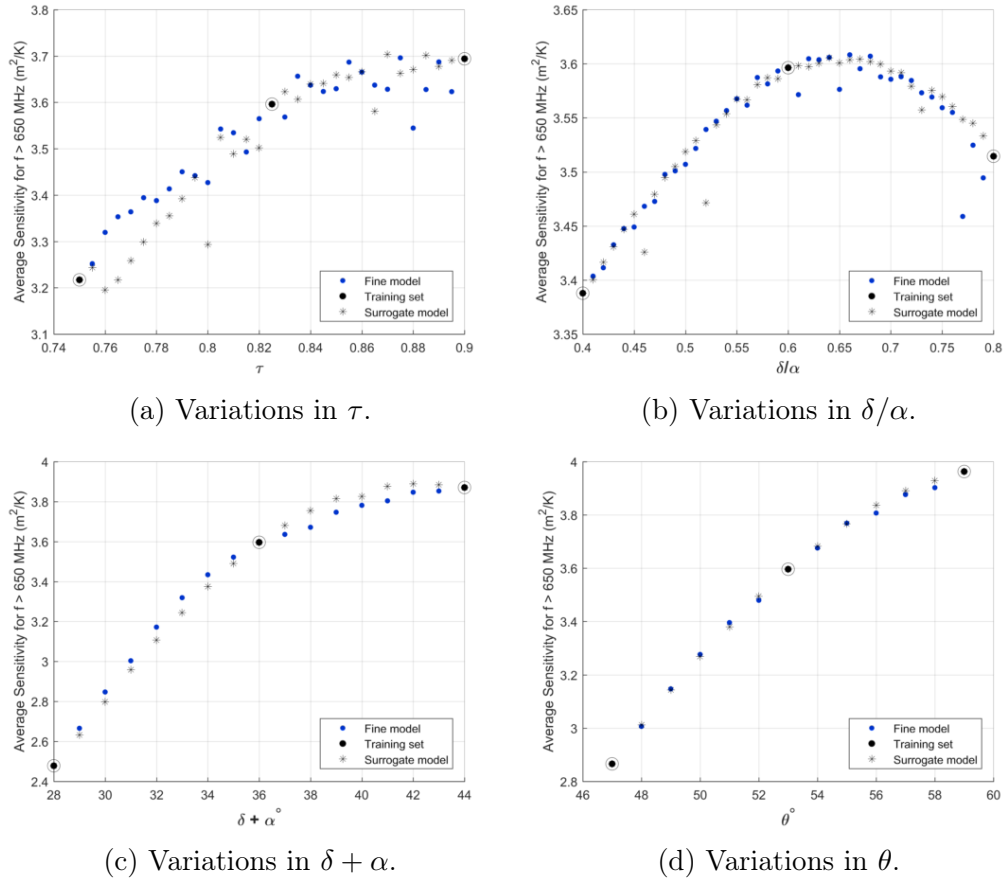


Figure 4.6: Sensitivity surrogates for Model 3.

Table 4.6 lists the ARE and the MRE for Model 3 and Table 4.7 lists the number of points which were required.

Table 4.6: Percentage errors for Model 3.

Parameter	ARE [%]	MRE [%]
τ	1.44	4.07
δ/α	0.34	2.59
$\delta + \alpha$	0.28	1.28
θ	0.27	0.78

Table 4.7: Number of points required for Model 3.

Parameter	# fine points	# coarse points
τ	108	711
δ/α	93	861
$\delta + \alpha$	93	357
θ	93	273

4.3 Comparisons of the Different Models

In this section, a comparison between the different models are made. For convenience, Table 4.8 provides a summary of the specifics of each model.

Table 4.8: Summary of the different models which were described.

Model	Description
1	Fits a second-order polynomial to the fine model data using a star distribution as support points.
2	Equation (4.14) is used to get the noise temperature, as opposed to Model 3 from [28], along with equation (4.13) for the aperture efficiency. A coarse sensitivity model is then evaluated according to equation (4.12) on the radiation patterns found from the full fine model structure of Figure 3.4a). The surrogate is built by finding the difference between the sensitivity of the coarse and fine models over a star distribution and applying a second-order polynomial regression term through these points to be used as a corrective function on the available coarse model data.
3	In this case the coarse sensitivity model of equation (4.12) is applied to the radiation patterns of the coarse model structures shown in Figures 3.4b) and 3.4c). The same correcting procedure as described for Model 2 is applied on this coarse model data.

In the designs to follow, the objective function $U^{(a)}$ is used for optimisation of the sensitivity of the system. Table 4.9 repeats the error values for this objective using the different models, so that an easier comparison can be made.

Table 4.9: Percentage errors for the different models.

Parameter	Model					
	1		2		3	
	ARE [%]	MRE [%]	ARE [%]	MRE [%]	ARE [%]	MRE [%]
τ	0.86	4.26	0.49	3.07	1.44	4.07
δ/α	0.30	2.50	0.33	0.81	0.34	2.59
$\delta + \alpha$	0.81	1.97	0.94	1.68	0.28	1.28
θ	0.20	0.63	0.29	0.89	0.27	0.78

For further comparison purposes, the CPU times of a representative example is shown in Table 4.10 for variations over $\delta + \alpha$. This is broken up into the time required to simulate the radiation patterns of the feed and the time required to get the sensitivity. For fine model evaluations of the sensitivity, GRASP simulations of the reflector antenna is required, whereas the coarse model evaluations require only integral calculations.

Table 4.10: CPU time required for the different models for variations in $\delta + \alpha$.

Model	CPU time [Hours]	Feed [Hours]	Sensitivity [Hours]
Fine	117.6	108.5	9.1
1	24.3	22.7	1.6
2	110.2	108.5	1.7
3	38.7	37.0	1.7

In this thesis, Model 3 is used for design purposes, since the coarse model data is available as it is used in the rational modelling scheme, as discussed in Chapter 5. From the error values in Table 4.9, it is not clear that adding coarse model data improves the surrogate model, when compared to Model 1. However, as the number of dimensions are increased, a simple polynomial may not model the response of the sensitivity of the system as accurately, thus the coarse model data is more trustworthy.

Chapter 5

Rational Interpolation Scheme Used to Model the Input Impedance of the Pyramidal Sinuous Antenna

In this chapter the use of rational interpolation to model the input impedance of the antenna is investigated. The goal is to design the pyramidal sinuous antenna for a reflection coefficient below -10 dB. The reflection coefficient is found from the input impedance according to equation (3.7). The objective function on which designs are implemented is the worst case scenario for each geometry over the frequency range of interest, i.e. the maximum S_{11} . First the framework for rational interpolation is introduced. Improvements were required in order to obtain a sufficiently accurate model. The interpolation methods are investigated extensively in the univariate case, by keeping the geometric parameters of the antenna constant and investigating changes over frequency. Specific drawbacks of the simpler methods are discussed and models which improve upon these drawbacks are introduced. Finally, a method that combines all desired behaviours is suggested. A few of the models are then extended to the multivariate case, first in two dimensions only, thus one geometric parameter is varied along with frequency. In chapters 6 and 7, variations in more dimensions are considered. This chapter concludes with a comparison of the rational interpolation method with other available surrogate models.

5.1 Univariate Rational Interpolation

In general, for real or complex function values $f_i := f(x_i)$ given at certain points over the parameter space $\{x_0, x_1, x_2, \dots\}$, the rational interpolation prob-

lem consists of finding a function

$$r_{n,m}(x) = \frac{p(x)}{q(x)} \quad (5.1)$$

with $p(x)$ and $q(x)$ polynomials of the form

$$p(x) = \sum_{i=0}^n a_i x^i, \quad q(x) = \sum_{i=0}^m b_i x^i, \quad (5.2)$$

such that

$$f(x_i) = \frac{p}{q}(x_i), \quad i = 0, \dots, S = n + m. \quad (5.3)$$

Equation (5.3) can be solved by rewriting it as

$$p(x_i) - f(x_i)q(x_i) = 0, \quad i = 0, \dots, S = n + m. \quad (5.4)$$

This can be written in matrix form as

$$\begin{pmatrix} x_0^0 & \dots & x_0^n & -f_0 x_0^0 & \dots & -f_0 x_0^m \\ x_1^0 & \dots & x_1^n & -f_1 x_1^0 & \dots & -f_1 x_1^m \\ \vdots & & & & & \\ \vdots & & & & & \\ x_{m+n}^0 & \dots & & & & \end{pmatrix} \begin{pmatrix} a_0 \\ \vdots \\ a_n \\ b_0 \\ \vdots \\ b_m \end{pmatrix} = \begin{pmatrix} 0 \\ \vdots \\ \vdots \\ \vdots \\ 0 \end{pmatrix} \quad (5.5)$$

Equation (5.5) is a homogeneous system of $m+n+1$ equations and $m+n+2$ unknowns. It therefore always has a nontrivial solution. All solutions of the system have the same irreducible form [54]. The matrix is assumed to have full rank equal to $(m+n+1)$ and so, without loss of generality, set $b_0 = 1$ to obtain the following linear system:

$$\begin{pmatrix} x_0^0 & \dots & x_0^n & -f_0 x_0^1 & \dots & -f_0 x_0^m \\ x_1^0 & \dots & x_1^n & -f_1 x_1^1 & \dots & -f_1 x_1^m \\ \vdots & & & & & \\ \vdots & & & & & \\ x_{m+n}^0 & \dots & & & & \end{pmatrix} \begin{pmatrix} a_0 \\ \vdots \\ a_n \\ b_1 \\ \vdots \\ b_m \end{pmatrix} = \begin{pmatrix} f_0 \\ \vdots \\ \vdots \\ \vdots \\ f_{m+n} \end{pmatrix} \quad (5.6)$$

The coefficients a_i and b_i can be solved in MATLAB [55] using the ' \backslash ' operator. For real function values $f_i \in \mathbb{R}$, the coefficients are also real and for complex function values $f_i \in \mathbb{C}$, the coefficients are complex valued. Note that applying the model on the complex function values results in the computational cost halving so, in general, this is preferred.

In Equation (5.2), the monomial basis function x^i is used. To improve the conditioning and sensitivity of the problem, it is better to use orthogonal basis functions, such as the Chebyshev polynomials $T_i(x)$, defined by the recursive relationship

$$\begin{aligned} T_0(x) &= 1, \\ T_1(x) &= x, \\ T_{n+1}(x) &= 2xT_n(x) - T_{n-1}(x). \end{aligned} \tag{5.7}$$

Thus, the matrix equation to be solved becomes

$$\begin{pmatrix} T_0(x_0) & \dots & T_n(x_0) & -f_0T_0(x_0) & \dots & -f_0T_m(x_0) \\ T_0(x_1) & \dots & T_n(x_1) & -f_1T_0(x_1) & \dots & -f_1T_m(x_1) \\ \vdots & & & & & \\ \vdots & & & & & \\ T_0(x_{m+n}) & \dots & & & & \end{pmatrix} \begin{pmatrix} a_0 \\ \vdots \\ a_n \\ b_1 \\ \vdots \\ b_m \end{pmatrix} = \begin{pmatrix} f_0 \\ \vdots \\ \vdots \\ \vdots \\ f_{m+n} \end{pmatrix} \tag{5.8}$$

Rational interpolants of this form were implemented on a representative example where the independent variable x is the frequency variation, first over the low band from 350 - 525 MHz and then in the high band from 790 - 1050 MHz. This domain for the high band was chosen to ensure that sampling from FEKO can be done at equidistant points. The geometric parameters are kept constant, with $\tau = 0.7825$, $\delta/\alpha = 0.6$, $\delta + \alpha = 36^\circ$ and $\theta = 53^\circ$. Figure 5.1 illustrates the rational interpolants when two separate models were implemented for the real function values of the imaginary and real parts of the input impedance, respectively, in each frequency band, whereas Figure 5.2 illustrates the rational interpolants when the complex values of the input impedance was used.

The figures show the interpolation points $f(x_i)$ as circled black dots, the rational interpolant $r_{n,m}(x)$ calculated as explained above and shown as the black line and validation data obtained by using FEKO's adaptive solver, shown in the figures as the blue dashed line. The validation data provides a quick visual verification of how closely the rational approximant follows the true underlying physical behaviour under consideration. In all cases, the degree n of the numerator was set equal to the degree m of the denominator.

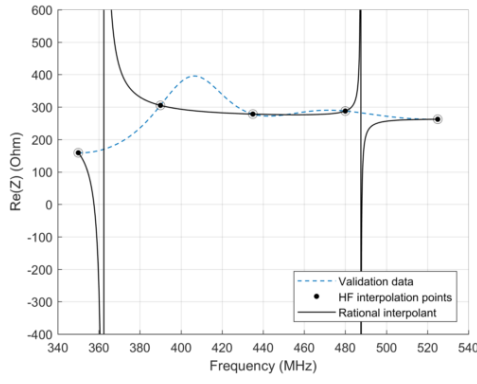
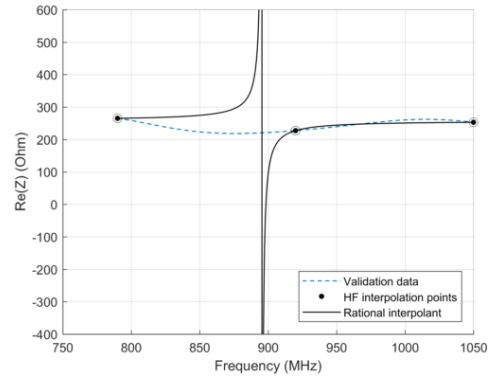
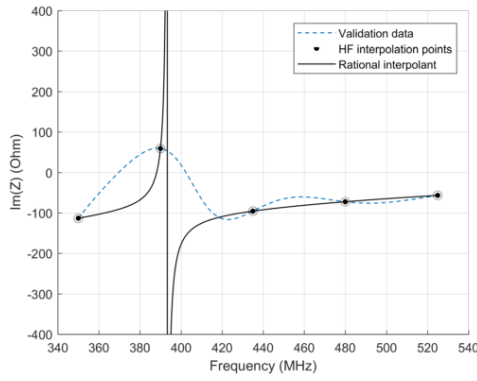
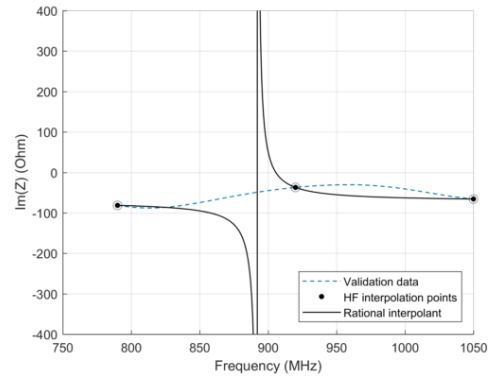
(a) $n = 2, m = 2$.(b) $n = 1, m = 1$.(c) $n = 2, m = 2$.(d) $n = 1, m = 1$.

Figure 5.1: Rational interpolants of the input impedance of the pyramidal sinuous antenna for variations in frequency when using equations (5.1) and (5.8) with the real and imaginary parts modeled separately. Here $\tau = 0.7825$, $\delta/\alpha = 0.6$, $\delta + \alpha = 36^\circ$ and $\theta = 53^\circ$.

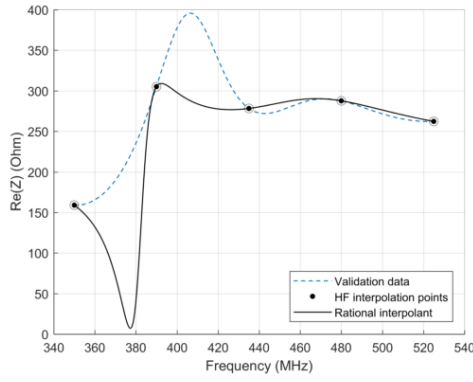
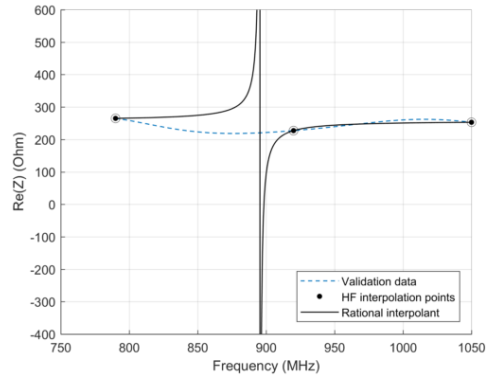
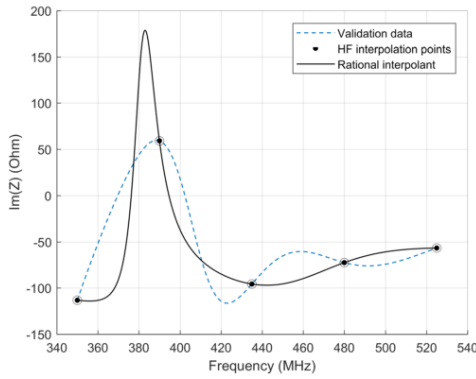
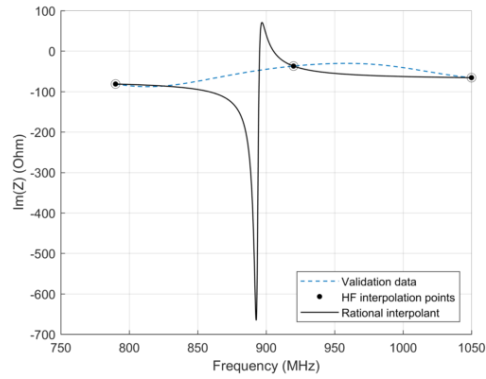
(a) $n = 2, m = 2$.(b) $n = 1, m = 1$.(c) $n = 2, m = 2$.(d) $n = 1, m = 1$.

Figure 5.2: Rational interpolants of the input impedance of the pyramidal sinusoidal antenna for variations in frequency when using equations (5.1) and (5.8) with complex function values. Here $\tau = 0.7825$, $\delta/\alpha = 0.6$, $\delta + \alpha = 36^\circ$ and $\theta = 53^\circ$.

As can be seen, the rational interpolant often contains undesirable poles. It is also possible with this formulation for certain interpolation points to become unattainable. This arises from the cancellation of a common factor $(x - x_i)$ in p and q , or in other words, where there is a common zero in the numerator and denominator at an interpolation point of the interpolant. The next section addresses these issues.

5.2 The Barycentric Formula

A polynomial of degree n that interpolates f_i at the points $\{x_0, \dots, x_n\}$ can be written in the Lagrangian representation [56] as

$$p_n(x) = \sum_{i=0}^n f_i w_i l_i(x) \quad (5.9)$$

with

$$l(x) = (x - x_0) \dots (x - x_n), \quad (5.10)$$

$$l_i(x) = l(x)/(x - x_i) \quad (5.11)$$

and

$$w_i = \frac{1}{\prod_{j \neq i} (x_i - x_j)}, \quad i = 0, \dots, n. \quad (5.12)$$

For example, the polynomial of degree 2 is

$$p_2(x) = \frac{f_0(x - x_1)(x - x_2)}{(x_0 - x_1)(x_0 - x_2)} + \frac{f_1(x - x_0)(x - x_2)}{(x_1 - x_0)(x_1 - x_2)} + \frac{f_2(x - x_0)(x - x_1)}{(x_2 - x_0)(x_2 - x_1)}.$$

It is easy to see that this is a second degree polynomial that equals f_i at x_i .

Now let the w_i equal any nonzero weights and let

$$q_n(x) = \sum_{i=0}^n w_i l_i(x), \quad (5.13)$$

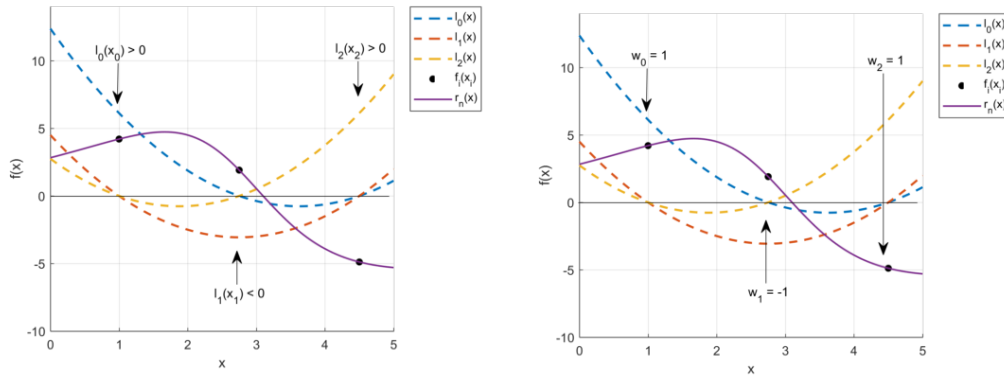
then the rational function $r_n(x) = p_n(x)/q_n(x)$ interpolates $n + 1$ mutually distinct points $\{x_0, \dots, x_n\}$ at the function values $\{f_0, \dots, f_n\}$. Thus

$$r_n(x) = \frac{\sum_{i=0}^n f_i w_i l_i(x)}{\sum_{i=0}^n w_i l_i(x)} = \frac{\sum_{i=0}^n f_i \frac{w_i}{x - x_i}}{\sum_{i=0}^n \frac{w_i}{x - x_i}}, \quad w_i \neq 0. \quad (5.14)$$

Equation (5.14) is called the barycentric rational interpolation formula. In this form, the interpolant is immune to rounding errors from the computation of the coefficients [57]. The function $l_i(x)$ can be viewed as a blending function that blends the very simple local models - the samples f_i in this case - into the global interpolation function. This is achieved by designing $l_i(x)$ to be zero at all sample points $j \neq i$, thereby ensuring the interpolation property $r_n(x_i) = f_i$. An illustration of these functions are shown in Figure 5.3. Note that $l_j(x_i) = 0$ for $j = 0, \dots, n$, $j \neq i$. Also note that the values of each consecutive function at its respective interpolation point oscillates in sign, as indicated in Figure 5.3a). Thus if $r_n(x)$ is to be pole-free on $[x_0, x_n]$, a necessary condition for the barycentric weights to satisfy is

$$w_i w_{i+1} < 0, \quad i = 0, \dots, n - 1. \quad (5.15)$$

If $x_0 < x_1 < \dots < x_n$, then the choice $w_i = (-1)^i$ ensures that $r_n(x)$ is pole-free on the entire real line, as noted in [56]. It also ensures that the problem of unattainability no longer exists, since $q_n(x_i) \neq 0$ on the entire real line. The appropriate weights are indicated in Figure 5.3b).

(a) Blending functions $l_i(x)$.

Note that $l_j(x_i) = 0$ with $j = 0, \dots, n$, $j \neq i$.

(b) Letting the weights $w_i = (-1)^i$ ensures a pole-free region on the real line.

Figure 5.3: Visual illustration of the barycentric rational interpolant with its blending functions $l_i(x)$. The choice of weights $w_i = (-1)^i$ ensures a pole-free region on the real line.

This choice was implemented for the same interpolant values as in Section 5.1 and the results are illustrated in Figure 5.4. Note that applying equation (5.14) with the constraint in (5.15) leads to exactly the same results when modelling real and imaginary parts separately, as when interpolating complex values, since the denominator is real valued and thus the rational model becomes additively separable in its real and imaginary components.

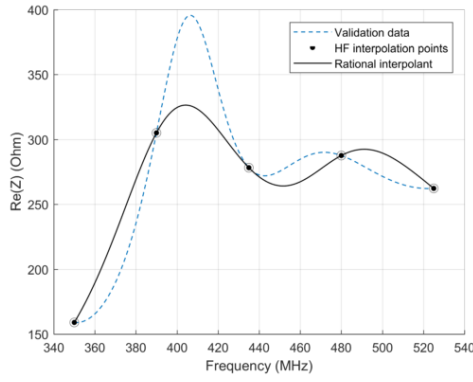
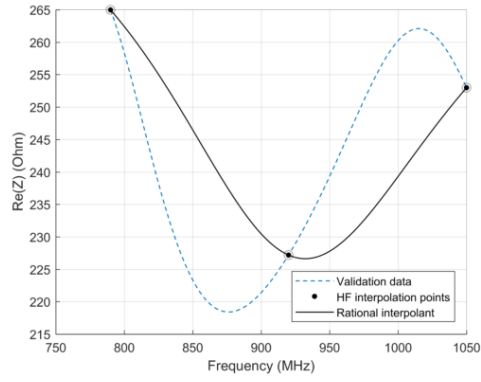
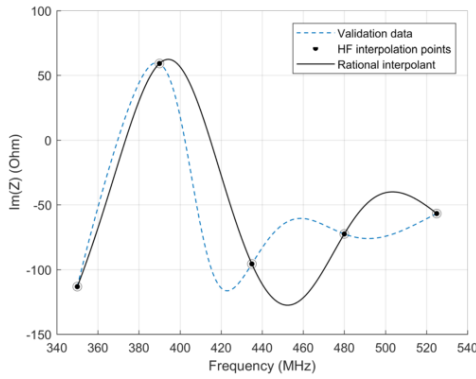
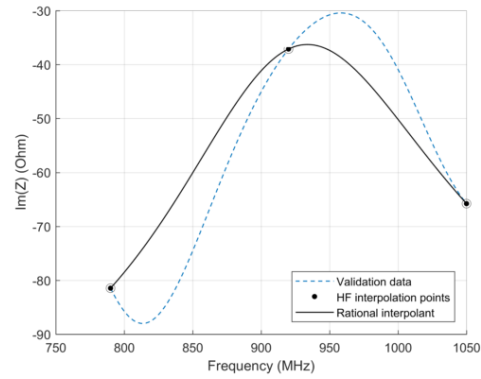
(a) $n = 5$.(b) $n = 3$.(c) $n = 5$ (d) $n = 3$.

Figure 5.4: Rational interpolants of the input impedance of the pyramidal sinuous antenna for variations in frequency when using equation (5.14) with condition (5.15) used to ensure a pole-free model. $\tau = 0.7825$, $\delta/\alpha = 0.6$, $\delta + \alpha = 36^\circ$ and $\theta = 53^\circ$.

It is possible to control the shape of the rational function by using more refined choices for the barycentric weights. See [58] for a discussion on how to control the comonotonicity as well as the coconvexity of the interpolant in addition to a pole-free region. As variations of the input impedance will be considered over frequency as well as the four geometric parameters in Table 3.3, the shape of these functions are uncertain, thus shape control for this application is superfluous.

Presented here is a different form of the barycentric weights as from [59], to illustrate how the function changes. Let $w_i = (-1)^i \sigma_i$, and

$$\sigma_i = \sum_{j=\max(i-d,0)}^{\min(i,n-d)} \binom{d}{i-j}, \quad n \geq 2d, \quad d = 1, 2, \dots \quad (5.16)$$

Figure 5.5 shows the results of using these weights. As can be seen, there is no easily identifiable advantage of the use of these weights over the previous example. The next section investigates weights that can improve the interpolant.

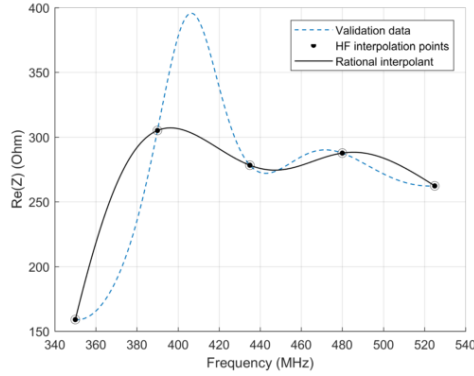
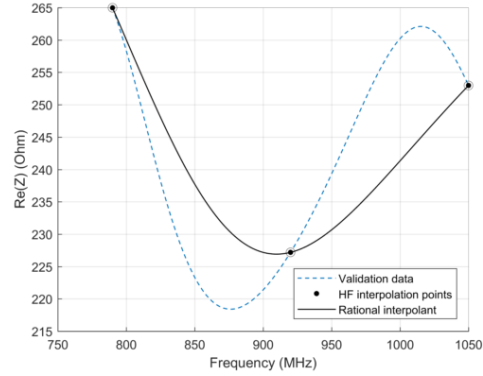
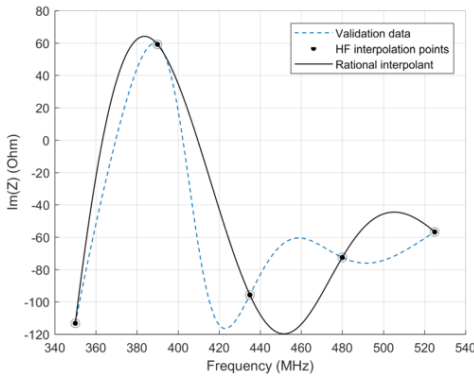
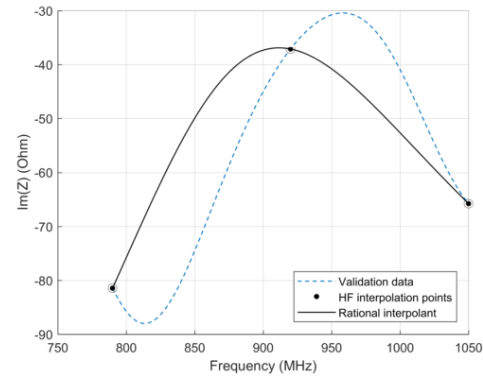
(a) $n = 5$.(b) $n = 3$.(c) $n = 5$ (d) $n = 3$.

Figure 5.5: Rational interpolants of the input impedance of the pyramidal sinuous antenna for variations in frequency when using equation (5.14) and (5.16). $\tau = 0.7825$, $\delta/\alpha = 0.6$, $\delta + \alpha = 36^\circ$ and $\theta = 53^\circ$.

5.3 Rational Modeling of Multi-Fidelity Data

This section looks at combining data with variable fidelity levels, in order to build a rational model over the entire design space. In antenna engineering problems the cost of highly accurate models is often prohibitively computationally expensive, especially when design space exploration and optimisation

are required. In these cases, lots of different antennas with varying parameters need to be simulated in order to get a clear representation of the trends followed by the different performance metrics under consideration. Because of this, it is useful to model data by combining different levels of fidelity. High fidelity (HF) data which is very accurate, but time consuming to produce, can be simulated sparsely over the parameter space, while low-fidelity (LF) data is less accurate, but it can be more densely captured over the parameter space. LF data captures the trend in the overall performance of the antenna.

The so-called fine model is the full antenna model over the entire frequency range. This was used to create the high-fidelity data. The coarse model consists of two smaller antennas simulated over a shorter frequency range, respectively at the low and high ends of the frequency spectrum, as described in Section 3.3 and illustrated in Figure 3.4. These models are used to obtain the low fidelity data. These two antennas combined take less time to simulate than the full antenna over the entire frequency range. Figure 5.6 illustrates the output of the real part of the input impedance for just one geometric variation of the antenna, namely $\theta = 53^\circ$, $\delta + \alpha = 36^\circ$, $\delta/\alpha = 0.6$ and $\tau = 0.75$.

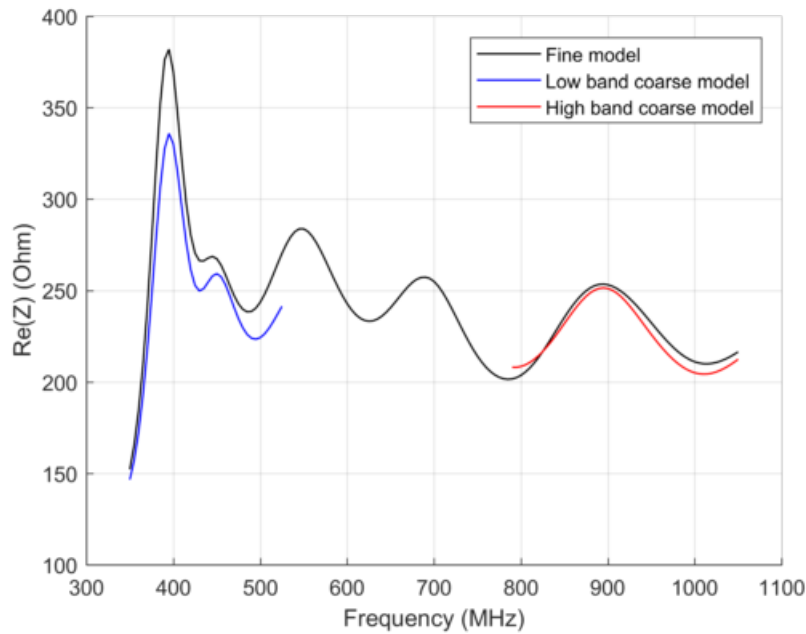


Figure 5.6: Illustration of the fine and coarse models used to create the low- and high-fidelity data.

As seen here, the coarse model data follows the trend of the fine model, but it is not completely accurate. Also, the coarse models only provide information at the band edges, however, as noted in Section 3.3, this should not affect the

results, since the outliers in S_{11} are expected to occur at either the high or low end of the frequency spectrum, with a log-periodic behaviour in the middle of the band.

Figure 5.7 provides a closer look of how the LF data follows the trend of the fine model output, with HF data sampled sparsely over the output range.

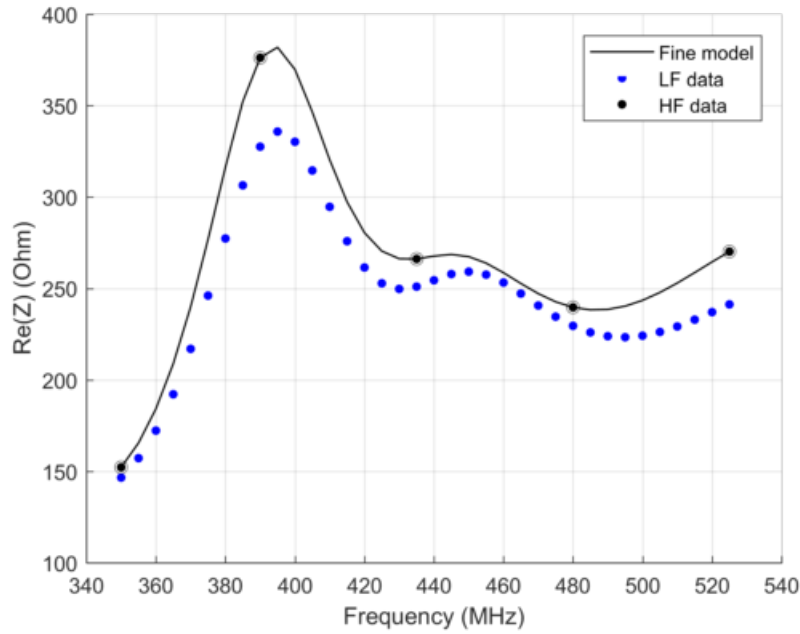


Figure 5.7: Illustration of the low- and high-fidelity data.

As seen in Figure 5.7 there are rarely points from the LF data that coincide with the HF data. Thus, the first step in building the rational model would be to calibrate the LF data so that it coincides more accurately with the HF data. This is done by calculating the difference between each HF and LF data point over the set of HF data points that are available and then interpolating this difference function with a spline in order to approximate the difference between the data where only LF data points are available.

For this purpose, two disjoint data sets are distinguished, namely

$$\text{HF} = \{x_k^H, f^H(x_k^H)\}_{k=1}^{K_H}$$

$$\text{LF} = \{x_i^L, f^L(x_i^L)\}_{i=1}^{K_L}$$

where the subset of LF data points that coincide with the domain of the HF data points are denoted as $f^L(x_k^L) \in f^L(x_i^L)$. HF is sparse when compared to LF ($K_H < K_L$) and the shorthand notation $f_k^H := f^H(x_k^H)$, $f_i^L := f^L(x_i^L)$ is

used throughout. The calibration step is performed by finding the difference function $s(x)$ by interpolating

$$s_k(x_k) = f_k^H - f_k^L, \quad k = 1, \dots, K_H \quad (5.17)$$

with a spline. In (5.17), $x_k^H = x_k^L$. Then the calibrated LF data set is found from

$$\text{LF}_c = f_i^L + s(x_i) = \{x_i^L, f^{L_c}(x_i^L)\}_{i=1}^{K_L}. \quad (5.18)$$

Note that $x_i^L \equiv x_i^{L_c}$. Figure 5.8 illustrates the process. After applying this calibration to the low fidelity data, the improved set can be seen in Figure 5.9. Note that in general, the LF data still contains inaccuracies compared to the fine model solution.

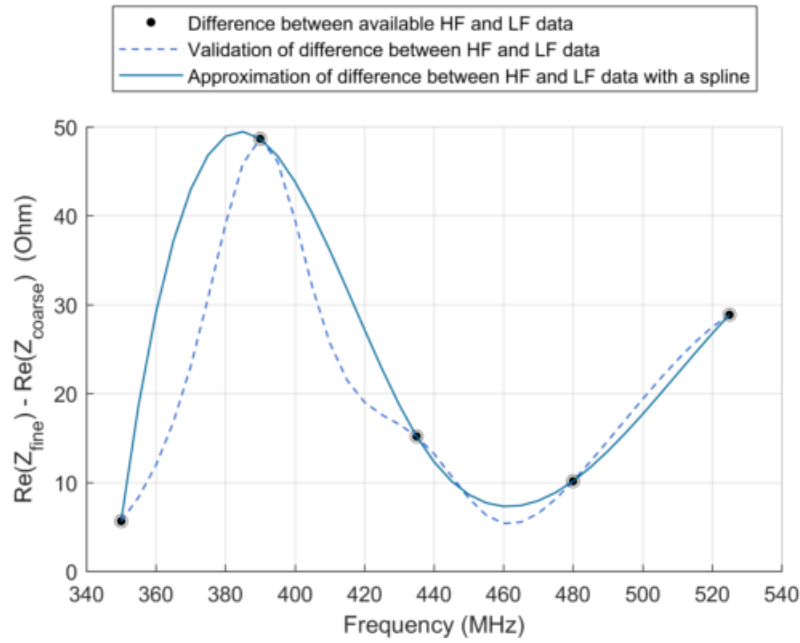


Figure 5.8: Spline interpolant through the difference between the HF and LF data points used to calibrate the LF data.

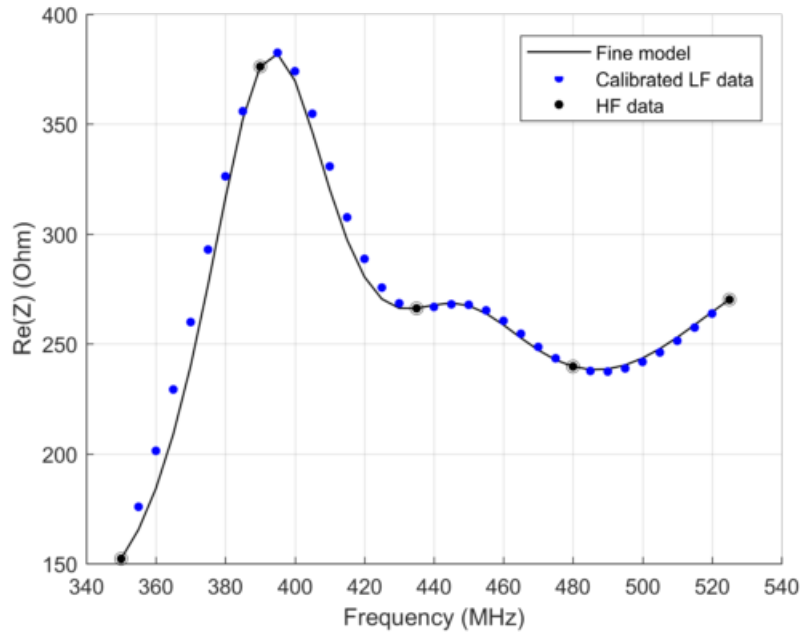


Figure 5.9: Data LF_c found by calibrating the LF data. Note that for each interpolation point, f_k^H and $f_k^{L_c}$ coincides.

The algorithm to find a rational function R , which approximates the behavioural response of a system f follows a two-step modelling approach, as suggested in [60]:

1. Use a barycentric rational model to interpolate the HF data exactly.
2. Calculate the weights of the model, w_k , such that the calibrated LF data is approximated in a least squares (LS) sense.

The rational model fixes the interpolation points of the HF model, such that $R(x_k^H) = f^H(x_k^H)$ for $k = 1, \dots, K_H$, for any non-zero barycentric weights

($\mathbf{w} = [w_k] \in \mathbb{R}^{K_H \times 1}$ with $w_k \neq 0$). Equation (5.19) is used in [60]:

$$\begin{aligned}
 R(x, \mathbf{w}) &= \frac{P(x, \mathbf{w})}{Q(x, \mathbf{w})} \\
 &= \frac{\sum_{k=1}^{K_H} \frac{w_k}{x - x_k^H} f^H(x_k^H)}{w_0 + \sum_{k=1}^{K_H} \frac{w_k}{x - x_k^H}} \\
 &= \frac{l(x) \sum_{k=1}^{K_H} \frac{w_k}{x - x_k^H} f^H(x_k^H)}{l(x) (w_0 + \sum_{k=1}^{K_H} \frac{w_k}{x - x_k^H})} \\
 &= \frac{\sum_{k=1}^{K_H} w_k l_k^H f^H(x_k^H)}{l(x) w_0 + \sum_{k=1}^{K_H} w_k l_k^H}.
 \end{aligned} \tag{5.19}$$

However, the $l(x)w_0$ term deviates from the true barycentric form in equation (5.14), thus redefine:

$$R(x, \mathbf{w}) = \frac{P(x, \mathbf{w})}{Q(x, \mathbf{w})} = \frac{\sum_{k=1}^{K_H} w_k l_k^H f^H(x_k^H)}{\sum_{k=1}^{K_H} w_k l_k^H} = \frac{\sum_{k=1}^{K_H} \frac{w_k}{x - x_k^H} f^H(x_k^H)}{\sum_{k=1}^{K_H} \frac{w_k}{x - x_k^H}}. \tag{5.20}$$

As mentioned in Section 5.2, the choice of \mathbf{w} can be exploited to enforce additional properties on the model. It is used here to approximate the LF_c data in a LS sense. In other words, that \mathbf{w} which minimises the sum of the squared residuals of the function R at each point f^{L_c} is found by solving

$$\underset{\mathbf{w}}{\operatorname{argmin}} \sum_{i=1}^{K_L} \left| \frac{P(x_i^L, \mathbf{w})}{Q(x_i^L, \mathbf{w})} - f^{L_c}(x_i^L) \right|^2. \tag{5.21}$$

However, (5.21) is a non-linear problem which is difficult to solve in a fast and accurate way. So it is preferred to solve the linear approximation

$$\underset{\mathbf{w}}{\operatorname{argmin}} \sum_{i=1}^{K_L} |P(x_i^L, \mathbf{w}) - f^{L_c}(x_i^L) Q(x_i^L, \mathbf{w})|^2 \tag{5.22}$$

which is equal to

$$\underset{\mathbf{w}}{\operatorname{argmin}} \sum_{i=1}^{K_L} \left| \sum_{k=1}^{K_H} \frac{w_k}{x - x_k^H} f^H(x_k^H) - f^{L_c}(x_i^L) \left(\sum_{k=1}^{K_H} \frac{w_k}{x - x_k^H} \right) \right|^2. \tag{5.23}$$

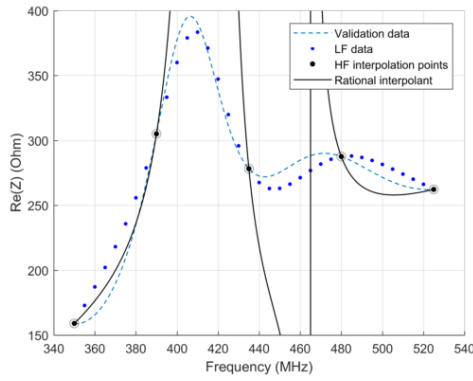
Equation (5.23) leads to a homogeneous system of the form $\mathbf{A}\mathbf{x} = \mathbf{0}$, where \mathbf{w} is found by solving the LS optimisation problem in (5.23) with the MATLAB

operator '\`' (mldivide). This is an overdetermined system, since $K_L > K_H$. The elements of the system are given by

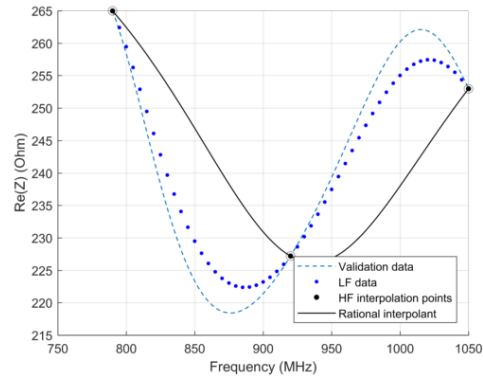
$$\mathbf{A} = [a_{ik}] \in \mathbb{C}^{K_L \times K_H} \quad \text{with} \quad a_{ik} = \frac{f^H(x_k^H) - f^{L_c}(x_i^L)}{(x_i^L - x_k^H)} \quad (5.24)$$

$$\text{and} \quad \mathbf{x} = \mathbf{w} \in \mathbb{R}^{K_H \times 1}.$$

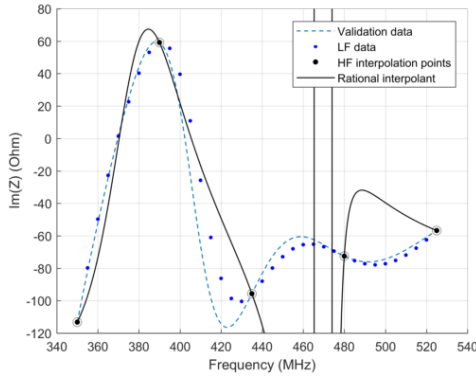
Equations (5.20) and (5.24) were implemented in MATLAB on the same data sets as previously, first on the real and imaginary data sets separately and then on the complex data sets, with results shown in Figures 5.10 and 5.11 respectively.



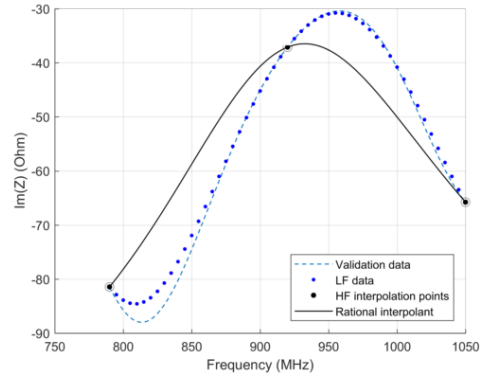
(a) $K_H = 5, K_L = 36$.



(b) $K_H = 3, K_L = 53$.



(c) $K_H = 5, K_L = 36$



(d) $K_H = 3, K_L = 53$.

Figure 5.10: Rational interpolants of the input impedance of the pyramidal sinuous antenna for variations in frequency when using equations (5.20) and (5.23) with the real and imaginary parts modelled separately. $\tau = 0.7825$, $\delta/\alpha = 0.6$, $\delta + \alpha = 36^\circ$ and $\theta = 53^\circ$.

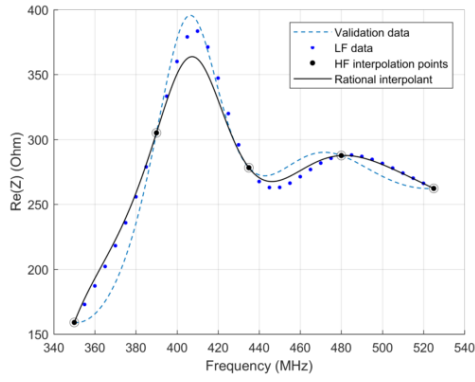
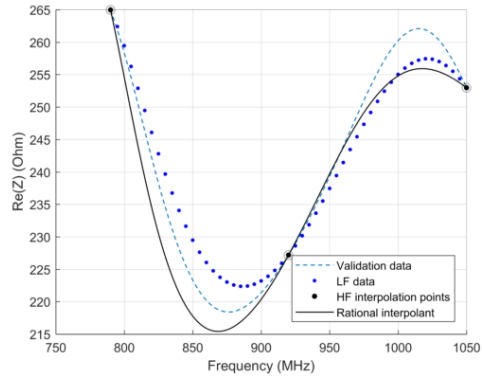
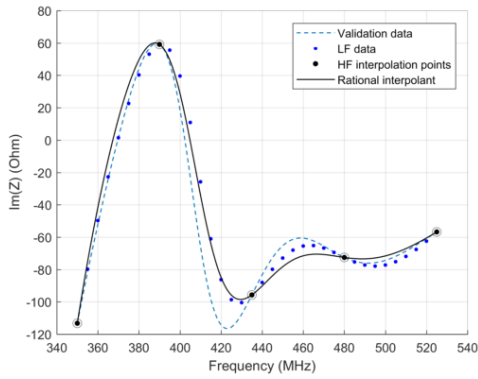
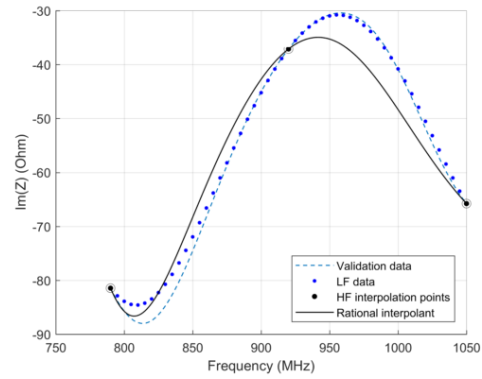
(a) $K_H = 5, K_L = 36$.(b) $K_H = 3, K_L = 53$.(c) $K_H = 5, K_L = 36$.(d) $K_H = 3, K_L = 53$.

Figure 5.11: Rational interpolants of the input impedance of the pyramidal sinuous antenna for variations in frequency when using equations (5.20) and (5.23) on the complex data sets. $\tau = 0.7825$, $\delta/\alpha = 0.6$, $\delta + \alpha = 36^\circ$ and $\theta = 53^\circ$.

As can be seen, the rational interpolant follows the calibrated LF data between the HF data points. However, Figures 5.10a) and 5.10c) indicate poles in the solutions of the rational approximants. Note that this is possible for both data sets, i.e. real and imaginary parts separately, as well as the complex data set. This is unwanted and so the next section addresses this issue.

5.4 Getting Rid of the Poles in the Rational Approximant of the Multi-Fidelity Data

In this section multi-fidelity (MF) data is used in the rational approximant, but with an additional constraint that ensures it contains no poles. In the previous section, the barycentric weights are solved by training the rational

approximant to follow the LF data in a LS sense. However, since no constraints are imposed on the model, naturally, the solution may contain poles. The sufficient condition to ensure that $R(x, \mathbf{w})$ is pole-free on $[x_0, x_n]$ is given in Section 2.3 of [58], namely that if $x_0 < x_1 < \dots < x_n$, $w_k = (-1)^k \phi_k$, $\phi_k > 0$ and $a < x_0, b > x_n$, then

$$\begin{aligned} \frac{\phi_{j-1}}{b - x_{j-1}} &< \frac{\phi_j}{b - x_j}, \quad j = 1, \dots, n, \\ \frac{\phi_j}{x_j - a} &> \frac{\phi_{j+1}}{x_{j+1} - a}, \quad j = 0, \dots, n-1. \end{aligned} \quad (5.25)$$

This constraint can be imposed on the homogeneous system of (5.24) by using MATLAB's 'lsqlin' function, however, this function cannot handle complex values, thus the real and imaginary parts of the matrix \mathbf{A} must be separated, resulting in

$$\mathbf{A} = \begin{bmatrix} \Re(a_{ik}) \\ \Im(a_{ik}) \end{bmatrix} \in \mathbb{R}^{2K_L \times K_H} \quad \text{with} \quad a_{ik} = \frac{f^H(x_k^H) - f^{Lc}(x_i^L)}{(x_i^L - x_k^H)}. \quad (5.26)$$

This is valid since

$$\begin{aligned} \left| \frac{f_k^H - f_i^{Lc}}{x_i^L - x_k^H} \right|^2 &= \left| \frac{(\Re(f_k^H) - \Re(f_i^{Lc})) + (\Im(f_k^H) - \Im(f_i^{Lc}))i}{x_i^L - x_k^H} \right|^2 \\ &= \left| \frac{\Re(f_k^H) - \Re(f_i^{Lc})}{x_i^L - x_k^H} \right|^2 + \left| \frac{\Im(f_k^H) - \Im(f_i^{Lc})}{x_i^L - x_k^H} \right|^2. \end{aligned} \quad (5.27)$$

Applying the constraints first to the real and imaginary parts separately and then on the complex valued functions lead to the results shown in Figures 5.12 and 5.13 respectively. Note that there are differences between the resulting models, however, these are very small, so in general, it is preferred to build the rational models directly on the complex valued functions.

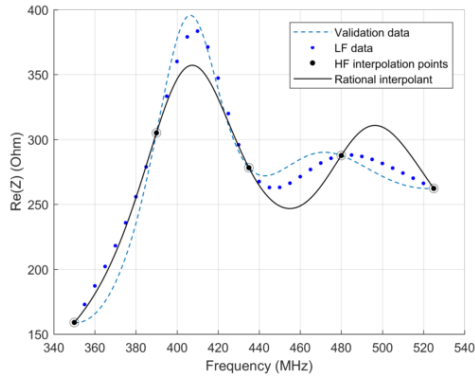
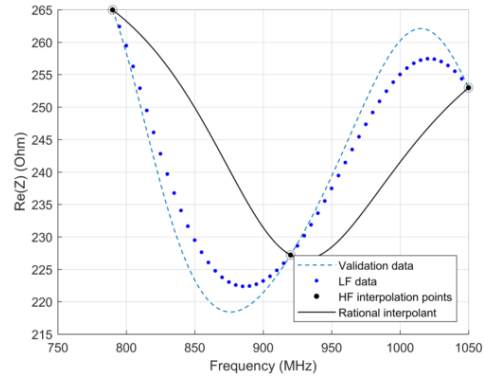
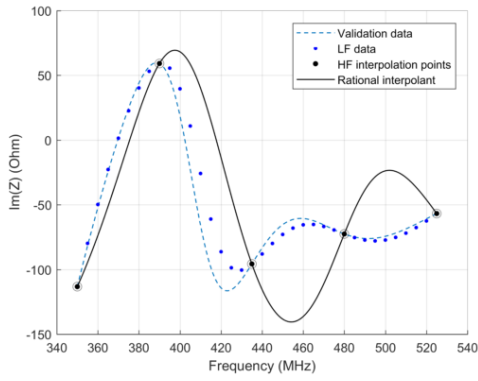
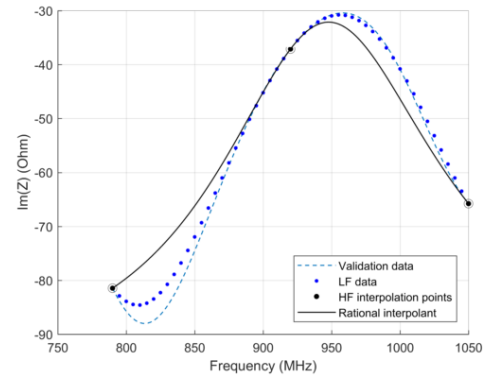
(a) $K_H = 5, K_L = 36$.(b) $K_H = 3, K_L = 53$.(c) $K_H = 5, K_L = 36$ (d) $K_H = 3, K_L = 53$.

Figure 5.12: Rational interpolants of the input impedance of the pyramidal sinuous antenna for variations in frequency when using equations (5.20) and (5.23) with the constraint (5.25) used to ensure a pole-free model. Real and imaginary parts are modelled separately. $\tau = 0.7825$, $\delta/\alpha = 0.6$, $\delta + \alpha = 36^\circ$ and $\theta = 53^\circ$.

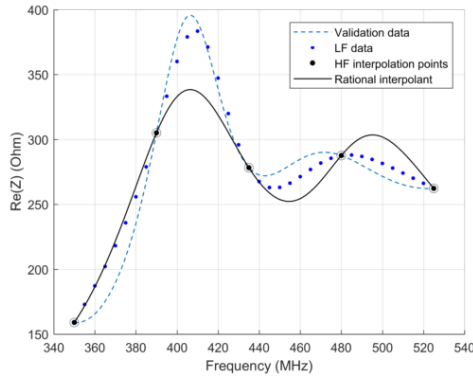
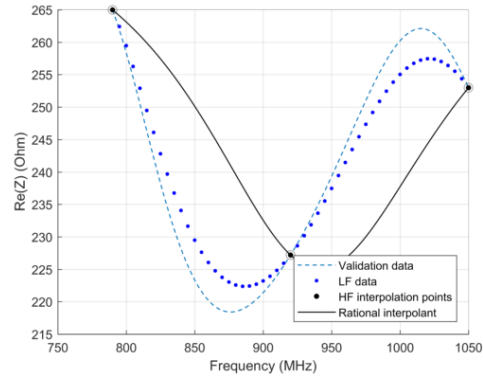
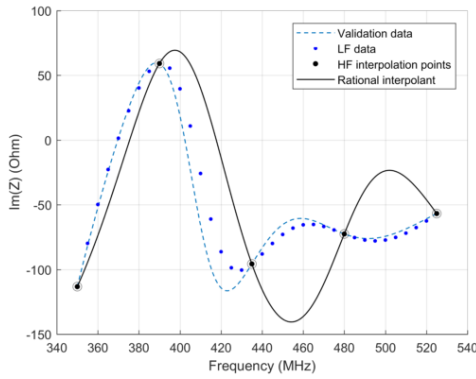
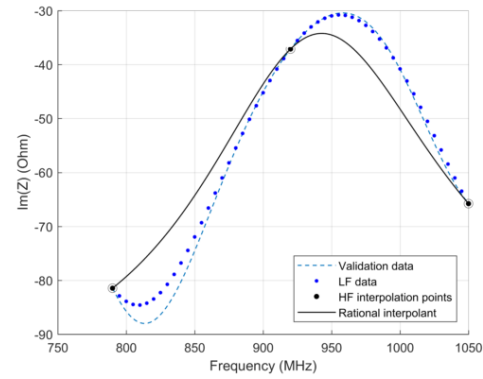
(a) $K_H = 5, K_L = 36$.(b) $K_H = 3, K_L = 53$.(c) $K_H = 5, K_L = 36$.(d) $K_H = 3, K_L = 53$.

Figure 5.13: Rational interpolants of the input impedance of the pyramidal sinuous antenna for variations in frequency when using equations (5.20) and (5.23) with the constraint (5.25) used to ensure a pole-free model. Models are on the complex data sets. $\tau = 0.7825$, $\delta/\alpha = 0.6$, $\delta + \alpha = 36^\circ$ and $\theta = 53^\circ$.

All approximants are now pole-free, as desired, however, the ability of the model to follow the LF data is poor. The constraints on the weights w_k might have become too strict to give the most useful results. An explanation for this is illustrated in Figure 5.14.

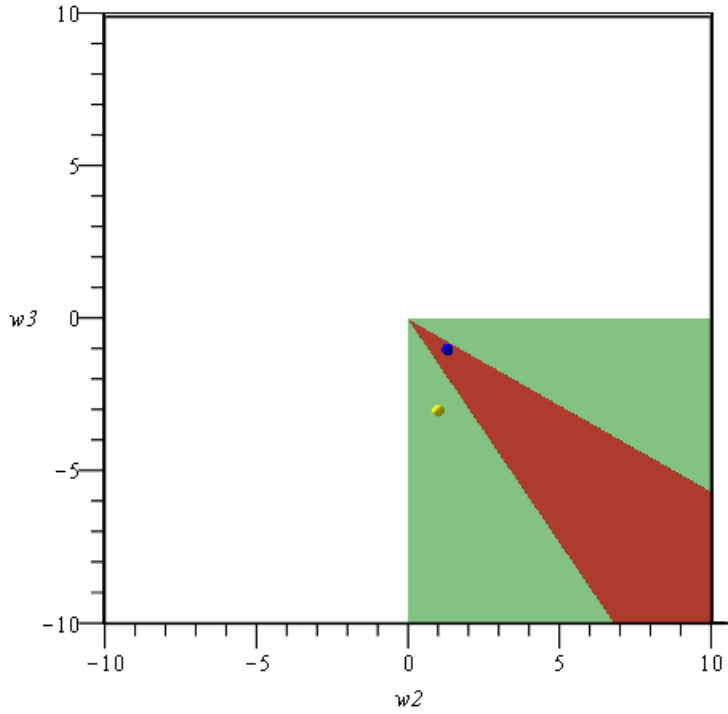


Figure 5.14: Solutions to the weights w_2 and w_3 when the sufficient condition of equation (5.25) to ensure a pole-free model is applied (blue dot) compared to when the necessary condition of equation (5.15) to ensure a pole-free model is applied (yellow dot). The green area indicates the possible solution space of equation (5.15), while the red area indicates the possible solution space of equation (5.25).

The illustration considers w_2 and w_3 only, but the principle extends to all the weights w_i . The necessary condition (5.15) for a barycentric rational interpolant free of poles is restricted to the fourth quadrant indicated by the green area where $w_2 w_3 < 0$. The sufficient condition (5.25) restricts the solution space to the area indicated in red. The yellow dot indicates the optimal solution to the least squares problem of equation (5.23) with the necessary condition applied, while the blue dot indicates the optimal solution when the sufficient condition is imposed. Thus this constraint may lead to sub-optimal results.

To assess the performance of the method, two different error measurements are associated with each interpolant: the average euclidean error and the maximum absolute error, computed on n samples of the validation data. These errors are defined in equations (4.6) and (4.7) respectively and are restated here for clarity:

$$\text{AEE} = \frac{1}{n} \sum_{j=1}^n \sqrt{(R(x_j, \mathbf{w}) - f(x_j))^2} \quad (5.28)$$

and

$$\text{MAX} = \max |R(x_j, \mathbf{w}) - f(x_j)|_{j=1}^n. \quad (5.29)$$

Table 5.1 lists these errors for the interpolants in Figures 5.12 and 5.13, where for the low band $n = 351$ and for the high band $n = 521$. For comparison purposes, the separate real and imaginary models are combined before calculating the errors.

Table 5.1: Error values for interpolants of Figures 5.12 and 5.13.

Model	AEE	MAX
(5.20) with $f(x) \in \mathbb{R}$	28.1048	116.2225
(5.20) with $f(x) \in \mathbb{C}$	29.6041	121.6738

The next section introduces an improved rational model that requires a relaxed constraint, while still guaranteeing a pole-free model.

5.5 Pole-Free Rational Interpolation of Multi-Fidelity Data Using B-Splines

B-Splines

In the previous section $l_k^H(x) = l(x)/(x - x_k^H)$ with $l(x) = (x - x_0^H) \dots (x - x_k^H)$ is used as a so-called blending function in the rational approximant $R(x, \mathbf{w})$ as in (5.20). This function changes sign at each HF (interpolation) point, and thus the weights w_k are required to oscillate in sign as well, in addition to the constraint (5.25), resulting in that the denominator never changes its sign, thus ensuring a pole-free approximant. The possible solutions of w_k under these constraints might become too limited to provide meaningful results, as illustrated in Figure 5.14. In other words, the rational approximant might not follow the LF data as well as it possibly could. In this section the quadratic B-spline function is used as an improved blending function as was done in [61]. It is always positive, and so the only constraint required for a pole-free solution is that $w_k > 0$.

The B-spline functions are defined recursively [62] as:

$$B_i^0(x) = \begin{cases} 1 & t_i \leq x < t_{i+1} \\ 0 & \text{otherwise} \end{cases} \quad (5.30)$$

and

$$B_i^k(x) = \left(\frac{x - t_i}{t_{i+k} - t_i} \right) B_i^{k-1}(x) + \left(\frac{t_{i+k+1} - x}{t_{i+k+1} - t_{i+1}} \right) B_{i+1}^{k-1}(x). \quad (5.31)$$

It is defined on the infinite set of knots $\{t_i\}$ with $\dots < t_{-2} < t_{-1} < t_0 < t_1 < t_2 < \dots$. Figure 5.15 shows the first four B-spline functions.

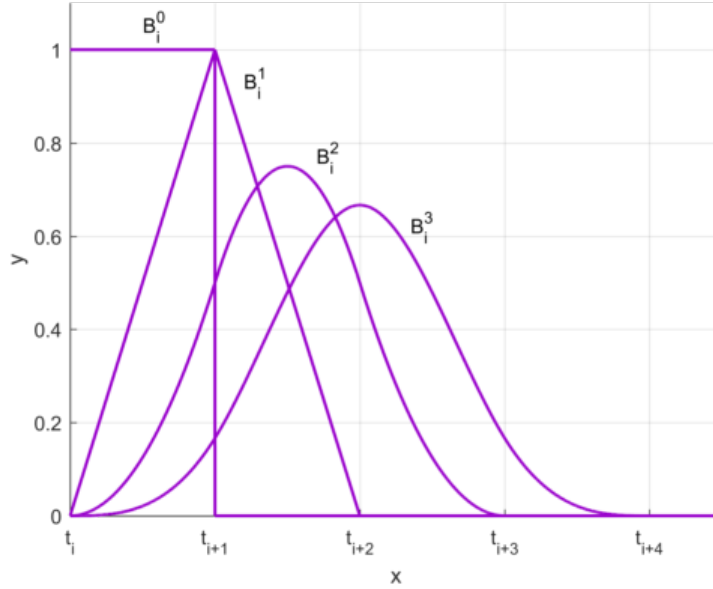


Figure 5.15: The first four B-Spline functions.

As mentioned, in this section the quadratic B-Spline function is used to replace the blending functions $l_k^H(x)$ in equation (5.20).

Bèzier Curves

In addition to using an improved blending function, firstly the HF data points $f^H(x_k^H)$ in (5.20) are replaced by a Bèzier curve which follows the trend of the $m_k - 2$ LF points between $f^H(x_k^H)$ and $f^H(x_{k+1}^H)$, while interpolating at each HF point. These local models reduce the responsibility on the weights to ensure that the models follow the trend of the LF points.

Bernstein proved in 1912 that for a continuous function $g(x)$ defined on $[0, 1]$, the sequence of polynomials

$$p_{ni}(x) = \sum_{i=0}^n g(i/n) \psi_{ni}(x) \quad (n \geq 1) \quad (5.32)$$

with

$$\psi_{ni}(x) = \binom{n}{i} x^i (1-x)^{n-i} \quad (0 \leq i \leq n). \quad (5.33)$$

converges uniformly to $g(x)$, while interpolating at the endpoints at $x = 0$ and $x = 1$. Thus, a local Bèzier curve $p_k(x)$ can be constructed on the data

points by rescaling every interval between two consecutive HF points $[x_k^H, x_{k+1}^H]$ with the $m_k - 2$ equidistant LF points in between it to $[0, 1]$. Note that equidistant LF points are required for the Bèzier curve. Thus $g(0) = f^H(x_k^H)$ and $g(1) = f^H(x_{k+1}^H)$, with the curve $p_k(x)$ following the trend of the LF points on the interval $[0, 1]$. Figure 5.16 illustrates the concept.

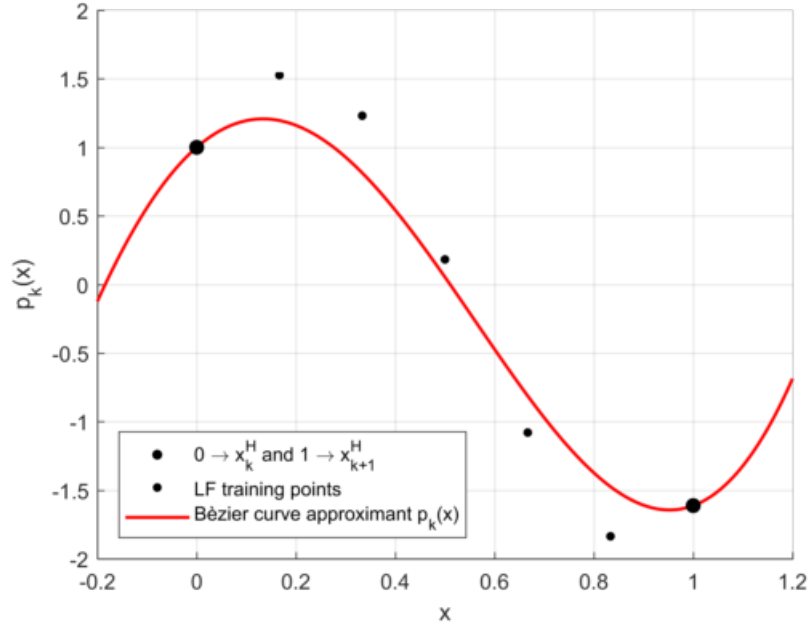


Figure 5.16: Illustration of a Bèzier curve for approximation of data on an interval between $[0, 1]$.

The Rational Interpolant

For the improved rational interpolant, define the domain of each interval I_k from every two consecutive HF points, $f^H(x_k^H)$ and $f^H(x_{k+1}^H)$, including the LF points between it. Thus

$$I_k = [x_k^H, x_{k+1}^H] = \{x_k^H = x_{k,1}^L < \dots < x_{k,m_k}^L = x_{k+1}^H\} \quad (5.34)$$

with $\sum_{k=1}^{K_H-1} (m_k - 1) = K_L - 1$. These intervals are mapped to $[0, 1]$ and then approximated by a Bèzier curve

$$\begin{aligned}
p_k(x) &= \sum_{j=1}^{m_k} f_{kj}^L \psi_{ij}(z), \\
f_{kj}^L &= f(x_{k,j}^L), \quad z = \frac{x - x_k^H}{x_{k+1}^H - x_k^H}, \\
\psi_{kj}(z) &= \binom{m_k}{j} z^j (1-z)^{m_k-j}.
\end{aligned} \tag{5.35}$$

So the improved rational expression, which now has a piecewise polynomial numerator and denominator, is defined as

$$R(x, \mathbf{w}) = \frac{P(x, \mathbf{w})}{Q(x, \mathbf{w})} = \frac{\sum_{k=1}^{K_H-1} w_k B_{k-1}^2(x) p_k(x)}{\sum_{k=1}^{K_H-1} w_k B_{k-1}^2(x)} \tag{5.36}$$

with $B_{k-1}^2(x)$ the quadratic B-spline function, supported by the two LF points outside of the interval I_k , i.e. its supports are at $[x_{k-1, m_{k-1}-1}^L, x_{k+1, 2}^L]$. Note that $B_{k-1}^2(x_k^H) = B_{k-1}^2(x_{k+1}^H)$, as evident from Figure 5.17.

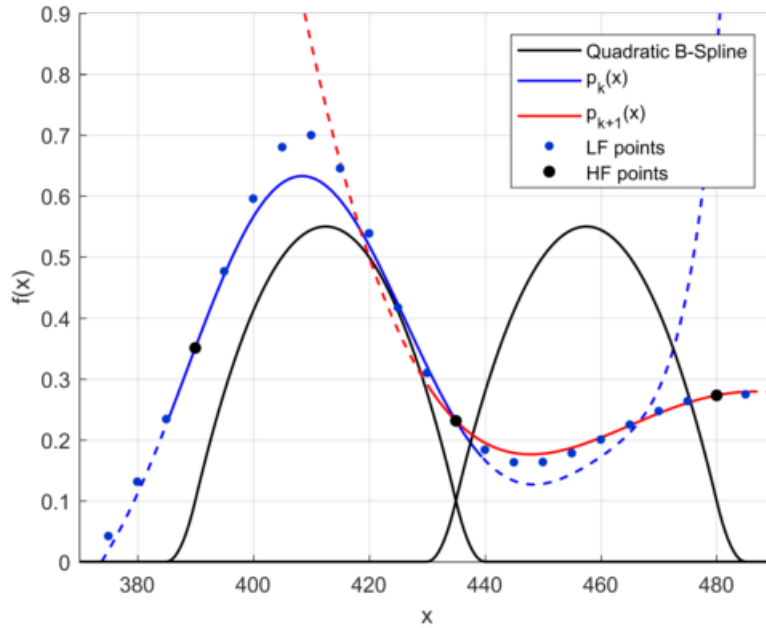


Figure 5.17: Illustration of the quadratic B-Spline blending functions and the local models $p_k(x)$. The dashed parts are multiplied by zero and thus do not contribute to the interpolant.

To see that equation (5.36) interpolates at $f(x_k^H)$, consider equations (5.37) and (5.38):

$$\begin{aligned} R(x_k^H, \mathbf{w}) &= \frac{\sum_{k=1}^{K_H-1} w_k B_{k-1}^2(x_k^H) p_k(x_k^H)}{\sum_{k=1}^{K_H-1} w_k B_{k-1}^2(x_k^H)} \\ &= \frac{w_1 B_0^2(x_k^H) p_1(x_k^H) + \dots + w_k B_{k-1}^2(x_k^H) p_k(x_k^H) + \dots + w_{K_H-1} B_{K_H-2}^2(x_k^H) p_{K_H-1}(x_k^H)}{w_1 B_0^2(x_k^H) + \dots + w_k B_{k-1}^2(x_k^H) + \dots + w_{K_H-1} B_{K_H-2}^2(x_k^H)} \end{aligned} \quad (5.37)$$

Now since all B_i^2 goes to zero at x_k^H , except for B_{k-1}^2 and B_{k-2}^2 , the above becomes

$$\begin{aligned} R(x_k^H, \mathbf{w}) &= \frac{w_{k-1} B_{k-2}^2(x_k^H) p_{k-1}(x_k^H) + w_k B_{k-1}^2(x_k^H) p_k(x_k^H)}{w_{k-1} B_{k-2}^2(x_k^H) + w_k B_{k-1}^2(x_k^H)} \\ &= \frac{w_{k-1} B_{k-2}^2 f(x_k^H) + w_k B_{k-1}^2 f(x_k^H)}{w_{k-1} B_{k-2}^2 + w_k B_{k-1}^2} \\ &= f(x_k^H). \end{aligned} \quad (5.38)$$

The weights w_k are once again found by solving the linearised LS optimisation problem from

$$\arg \min_{\mathbf{w}} \sum_{i=1}^{K_H-1} \sum_{j=1}^{m_k} \left| f_{ij}^L \sum_{k=1}^{K_H-1} w_k B_{k-1,2}^2(x_{i,j}^L) - \sum_{k=1}^{K_H-1} w_k p_k(x_{i,j}^L) B_{k-1,2}^2(x_{i,j}^L) \right|^2 \quad (5.39)$$

where the only constraint to ensure a pole-free model is that the weights must be positive, i.e. $w_k > 0$. Equation (5.39) is solved using MATLAB's 'lsqlin' function, where once again the real and imaginary parts must be separated for complex function values. Applying the newly defined $R(x, \mathbf{w})$ of equation (5.36) to the data as previously, gives the results as shown in Figure 5.18 with the real and imaginary parts modelled separately and in Figure 5.19 on the complex data.

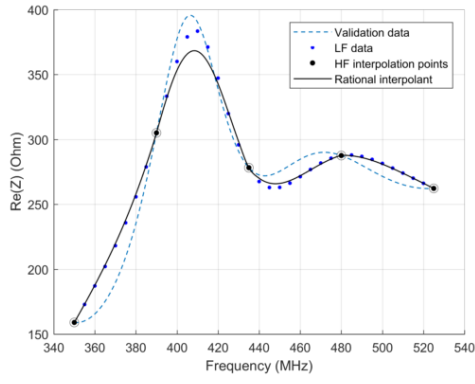
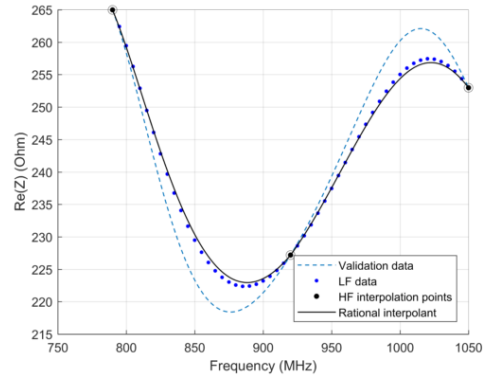
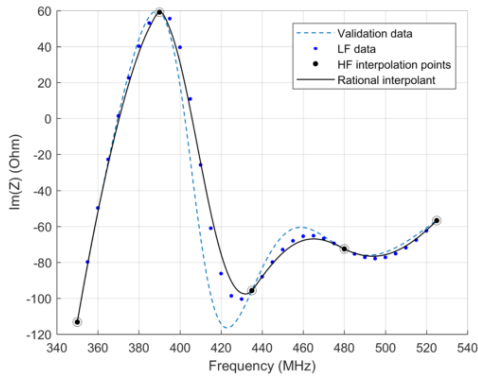
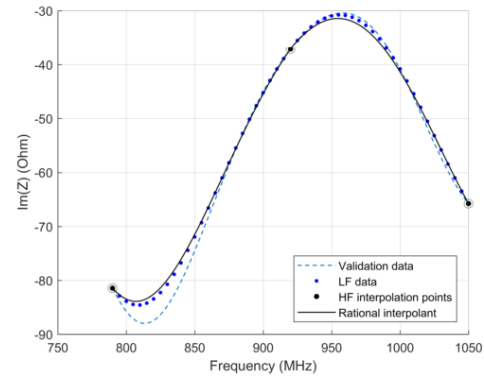
(a) $K_H = 5, K_L = 36$.(b) $K_H = 3, K_L = 53$.(c) $K_H = 5, K_L = 36$ (d) $K_H = 3, K_L = 53$.

Figure 5.18: Rational interpolants of the input impedance of the pyramidal sinuous antenna for variations in frequency when using equations (5.36) and (5.39) with the constraint that $w_k > 0$, ensuring a pole-free model. Real and imaginary parts are modelled separately. $\tau = 0.7825$, $\delta/\alpha = 0.6$, $\delta + \alpha = 36^\circ$ and $\theta = 53^\circ$.

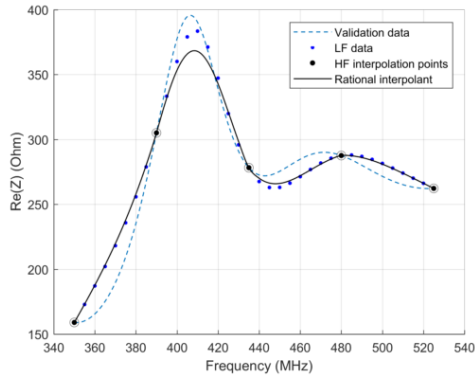
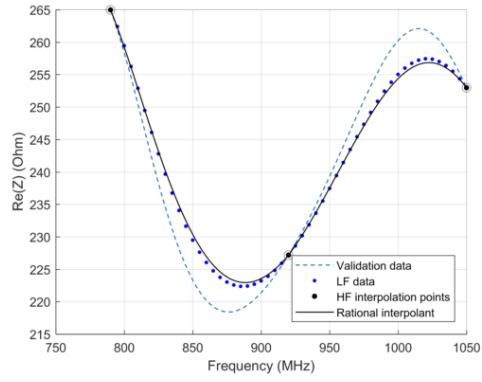
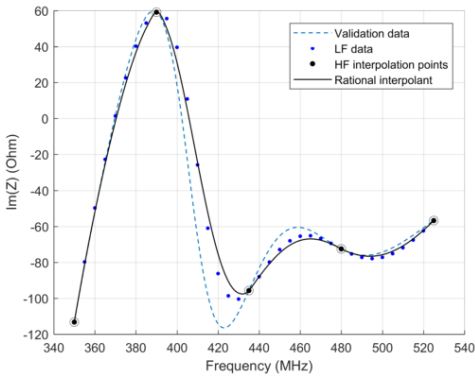
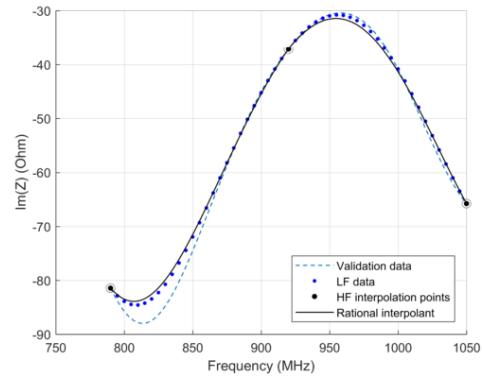
(a) $K_H = 5, K_L = 36$.(b) $K_H = 3, K_L = 53$.(c) $K_H = 5, K_L = 36$.(d) $K_H = 3, K_L = 53$.

Figure 5.19: Rational interpolants of the input impedance of the pyramidal sinuous antenna for variations in frequency when using equations (5.36) and (5.39) with the constraint that $w_k > 0$, ensuring a pole-free model. Models were applied directly to the complex data sets. $\tau = 0.7825$, $\delta/\alpha = 0.6$, $\delta + \alpha = 36^\circ$ and $\theta = 53^\circ$.

The error values for this method are listed in Table 5.2. In this case, the models performed the same when built separately as when built on the complex values, to within 10 decimal places, thus the errors for both models are the same. Once again, the low band $n = 351$ and the high band $n = 521$.

Table 5.2: Error values for interpolants of Figures 5.18 and 5.19

Model	AEE	MAX
(5.36)	8.8381	48.023

A significant improvement is seen in the error values of this model when compared to those of Table 5.1. The accuracy of this model is strongly de-

pendent on how accurately the LF data represents the HF data. Of course, increasing the number of HF points would lead to an improved model. It is up to the designer to trade off an acceptable amount of computational time required to simulate HF data with an acceptable level of accuracy for the rational models. In the next section, the above method is extended to the multivariate case.

5.6 Multivariate Rational Interpolation

5.6.1 The Barycentric Formula

The extension of the univariate rational interpolation to the multivariate case is straightforward. Firstly, the multivariate case of the barycentric formula of equation (5.14) is defined. Increasing this formula to higher dimensions is simple. The focus is on a grid of interpolation points $f_{i_1 \dots i_n}(x_1, \dots, x_n)$ with $i_j = 0, \dots, m_j$ and $j = 1, \dots, n$, with n being the number of dimensions. The multivariate barycentric formula is then

$$\begin{aligned}
 r_{\mathbf{m}}(\mathbf{x}) &= r_{m_1, \dots, m_n}(x_1, \dots, x_n) \\
 &= \frac{\sum_{i_1=0}^{m_1} \dots \sum_{i_n=0}^{m_n} l_{\mathbf{i}}(\mathbf{x}) w_{\mathbf{i}} f_{\mathbf{i}}(\mathbf{x})}{\sum_{i_1=0}^{m_1} \dots \sum_{i_n=0}^{m_n} l_{\mathbf{i}}(\mathbf{x}) w_{\mathbf{i}}} \\
 &= \frac{\sum_{i_1=0}^{m_1} \dots \sum_{i_n=0}^{m_n} l_{i_1 \dots i_n}(x_1, \dots, x_n) w_{i_1} \dots w_{i_n} f_{i_1 \dots i_n}(x_1, \dots, x_n)}{\sum_{i_1=0}^{m_1} \dots \sum_{i_n=0}^{m_n} l_{i_1 \dots i_n}(x_1, \dots, x_n) w_{i_1} \dots w_{i_n}(x_1, \dots, x_n)} \\
 &= \frac{\sum_{i_1=0}^{m_1} \dots \sum_{i_n=0}^{m_n} \frac{w_{i_1} \dots w_{i_n} f_{i_1 \dots i_n}(x_1, \dots, x_n)}{(x_1 - x_{i_1}) \dots (x_n - x_{i_n})}}{\sum_{i_1=0}^{m_1} \dots \sum_{i_n=0}^{m_n} \frac{w_{i_1} \dots w_{i_n}}{(x_1 - x_{i_1}) \dots (x_n - x_{i_n})}} \tag{5.40} \\
 &= \frac{\sum_{i_1=0}^{m_1} \frac{w_{i_1}}{(x_1 - x_{i_1})} \dots \sum_{i_n=0}^{m_n} \frac{w_{i_n}}{(x_n - x_{i_n})} f_{i_1 \dots i_n}(x_1, x_2, \dots, x_n)}{\sum_{i_1=0}^{m_1} \frac{w_{i_1}}{(x_1 - x_{i_1})} \dots \sum_{i_n=0}^{m_n} \frac{w_{i_n}}{(x_n - x_{i_n})}}
 \end{aligned}$$

where

$$l_{\mathbf{i}} = \frac{l(x_1, \dots, x_n)}{(x_1 - x_{i_1}) \dots (x_n - x_{i_n})} \tag{5.41}$$

$$l(x_1, \dots, x_n) = \prod_{i_1=0}^{m_1} (x_1 - x_{i_1}) \dots \prod_{i_n=0}^{m_n} (x_n - x_{i_n}) \tag{5.42}$$

and the weights w_{i_1}, \dots, w_{i_n} are nonzero and as before must oscillate in sign, since the necessary condition for a pole-free region is

$$w_{i_j} w_{i_{j+1}} < 0, \quad i = 0, \dots, m_n - 1, \quad j = 1, \dots, n. \tag{5.43}$$

The weights $w_{i_j} = (-1)^{i_j}$ for $j = 1, \dots, n$ are known to ensure a pole-free region, as in the univariate case [56].

5.6.2 Using Multi-Fidelity Data with B-Splines

As the benefits of equation (5.36) are known, this is extended immediately to the multivariate case. The multi-dimensional Bèzier interpolant is defined as

$$p_{m_1, \dots, m_n}(x_1, \dots, x_n) = \sum_{i_1=0}^{m_1} \dots \sum_{i_n=0}^{m_n} g(i_1/n_1, \dots, i_n/m_n) \psi_{m_1 i_1, \dots, m_n i_n}(x_1, \dots, x_n) \quad (5.44)$$

with $(m_1, \dots, m_n \geq 1)$ and

$$\psi_{m_1 i_1, \dots, m_n i_n}(x_1, \dots, x_n) = \binom{m_1}{i_1} \dots \binom{m_n}{i_n} x_1^{i_1} (1 - x_1)^{m_1 - i_1} \dots x_n^{i_n} (1 - x_n)^{m_n - i_n}. \quad (5.45)$$

Here $(0 \leq i_1 \leq m_1), \dots, (0 \leq i_n \leq m_n)$ and $g : I := [0, 1] \times \dots \times [0, 1] \rightarrow \mathbb{R}^n$. The Bèzier interpolant $p_{m_1, \dots, m_n}(x_1, \dots, x_n)$ converges pointwise to $g(x_1, \dots, x_n)$ for $m_1, \dots, m_n \rightarrow \infty$. It interpolates at the corners of the $[0, 1] \times \dots \times [0, 1]$ grid for any m_1, \dots, m_N . Figure 5.20 illustrates an example for $n = 2$.

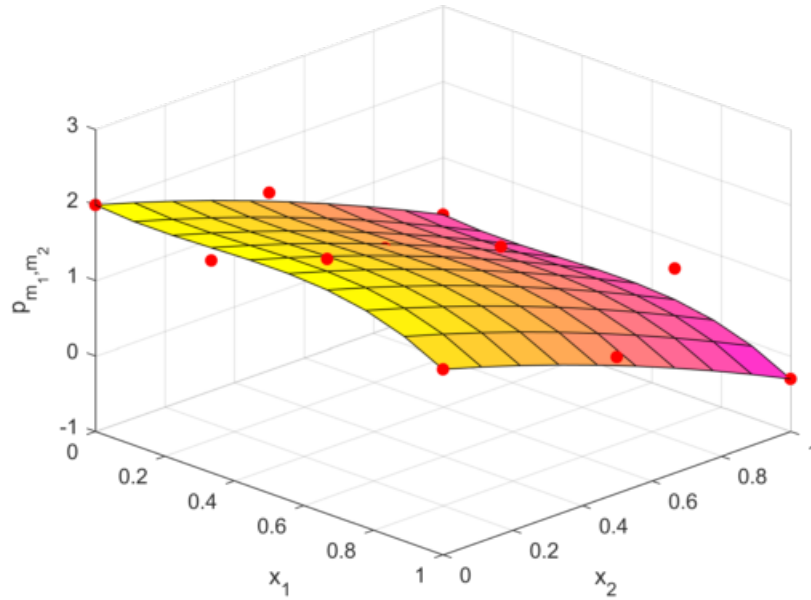


Figure 5.20: Illustration of Bèzier interpolation in two dimensions.

In two dimensions each grid of four HF points with LF points between it is mapped to the region $[0, 1] \times [0, 1]$ so that it can be approximated locally

with a Bèzier interpolant $p_{k_1 k_2}(x_1, x_2)$ on every interval $I_{k_1 k_2} := [f^H(x_{k_1}^H, x_{k_2}^H), f^H(x_{k_1+1}^H, x_{k_2+1}^H)]$.

The rational interpolant which makes use of B-splines to blend the intervals together in two dimensions is defined as

$$\begin{aligned} R(x_1, x_2, \mathbf{w}) &= \frac{P(x_1, x_2, \mathbf{w})}{Q(x_1, x_2, \mathbf{w})} \\ &= \frac{\sum_{k_1=1}^{m_1-1} \sum_{k_2=1}^{m_2-1} w_{k_1} w_{k_2} B_{k_1-1}^2(x_1) B_{k_2-1}^2(x_2) p_{k_1 k_2}(x_1, x_2)}{\sum_{k_1=1}^{m_1-1} \sum_{k_2=1}^{m_2-1} w_{k_1} w_{k_2} B_{k_1-1}^2(x_1) B_{k_2-1}^2(x_2)} \end{aligned} \quad (5.46)$$

and where the number of HF points are $K_H = m_1 m_2$. Once again the only constraint on the weights are that $w_{k_1}, w_{k_2} > 0$. These are solved as before by following the LF data in the LS sense, thus by solving the linearised optimisation problem

$$\underset{\mathbf{w}}{\operatorname{argmin}} \sum_{i=1}^{K_L} |P(x_{i_1}^L, x_{i_2}^L, \mathbf{w}) - f^L(x_{i_1}^L, x_{i_2}^L) Q(x_{i_1}^L, x_{i_2}^L, \mathbf{w})|^2, \quad (5.47)$$

with K_L the number of LF data points.

The grids to be considered in the following examples are listed in Table 5.3.

Table 5.3: Grids on which interpolants are built for every geometric parameter.

x_1	x_2	m_1	m_2	K_H	K_L
$\tau \in [0.75, 0.9]$	Frequency $\in [350, 525]$ (MHz)	11	9	99	1116
$\tau \in [0.75, 0.9]$	Frequency $\in [790, 1050]$ (MHz)	11	12	132	1643
$\delta/\alpha \in [0.4, 0.8]$	Frequency $\in [350, 525]$ (MHz)	8	9	72	1476
$\delta/\alpha \in [0.4, 0.8]$	Frequency $\in [790, 1050]$ (MHz)	8	12	96	2173
$\delta + \alpha \in [28, 44]$ (Degrees)	Frequency $\in [350, 525]$ (MHz)	8	9	72	612
$\delta + \alpha \in [28, 44]$ (Degrees)	Frequency $\in [790, 1050]$ (MHz)	8	12	96	901
$\theta \in [47, 59]$ (Degrees)	Frequency $\in [350, 525]$ (MHz)	3	9	27	468
$\theta \in [47, 59]$ (Degrees)	Frequency $\in [790, 1050]$ (MHz)	3	12	36	689

Figures 5.21 - 5.24 show the results of using equations (5.46) and (5.47) for variations in τ , δ/α , $\delta + \alpha$ and θ respectively, along with the low and high frequency bands. It is used to model the input impedance on a grid which is four times finer than the number of coarse samples in each dimension for every geometric parameter. Thus the input impedance is available on a grid that is sixteen times larger than the number of LF points. The interpolants are applied to the complex data in each case.

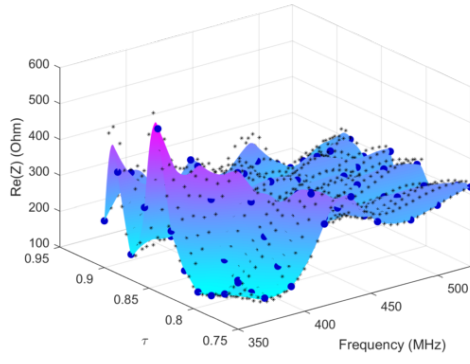
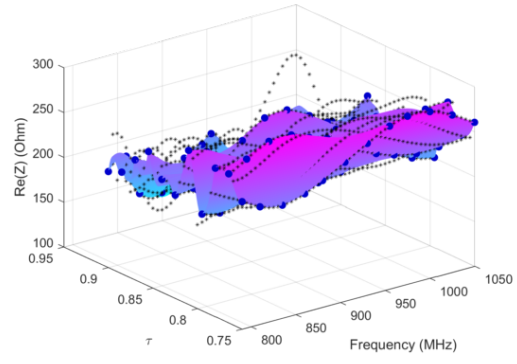
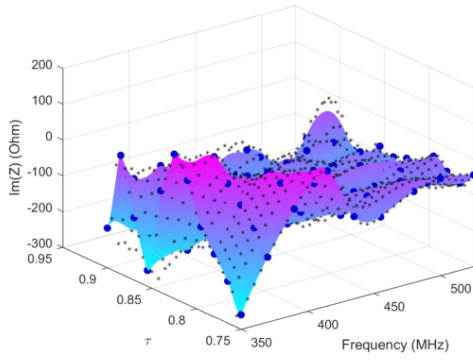
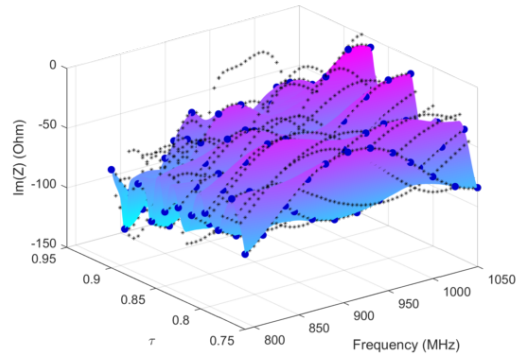
(a) $K_H = 99, K_L = 1116$.(b) $K_H = 132, K_L = 1643$.(c) $K_H = 99, K_L = 1116$.(d) $K_H = 132, K_L = 1643$.

Figure 5.21: Rational interpolants of the input impedance of the pyramidal sinuous antenna for variations in τ and frequency when using equations (5.46) and (5.39) on the complex data. $\delta/\alpha = 0.6$, $\delta + \alpha = 36^\circ$ and $\theta = 53^\circ$.

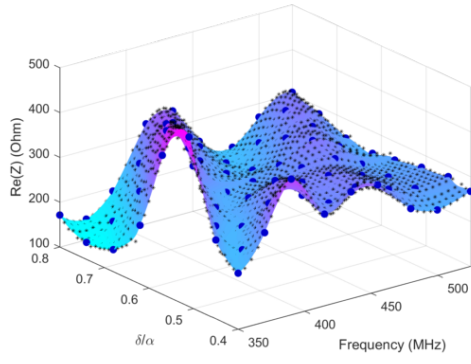
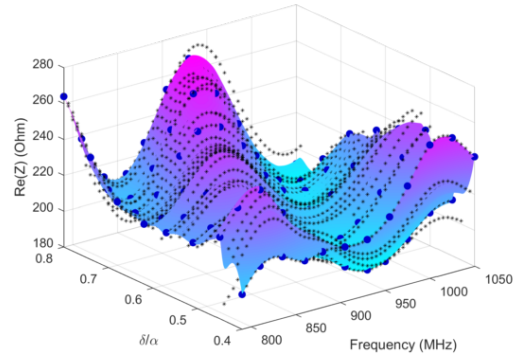
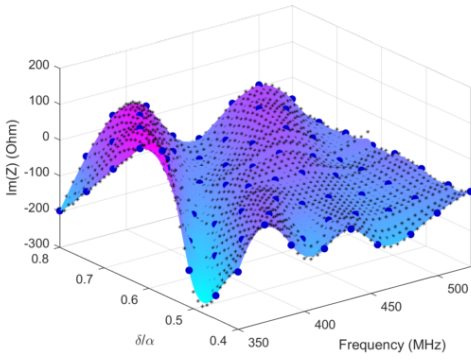
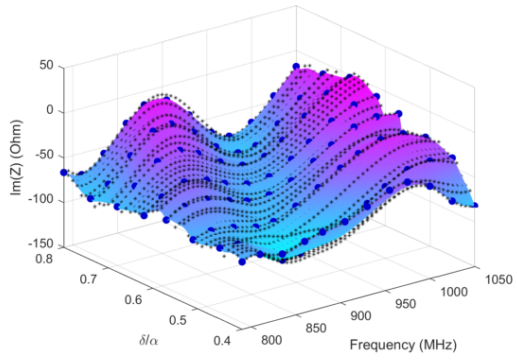
(a) $K_H = 72, K_L = 1476$.(b) $K_H = 96, K_L = 2173$.(c) $K_H = 72, K_L = 1476$.(d) $K_H = 96, K_L = 2173$.

Figure 5.22: Rational interpolants of the input impedance of the pyramidal sinuous antenna for variations in δ/α and frequency when using equations (5.46) and (5.39) on the complex data. $\tau = 0.825$, $\delta + \alpha = 36^\circ$ and $\theta = 53^\circ$.

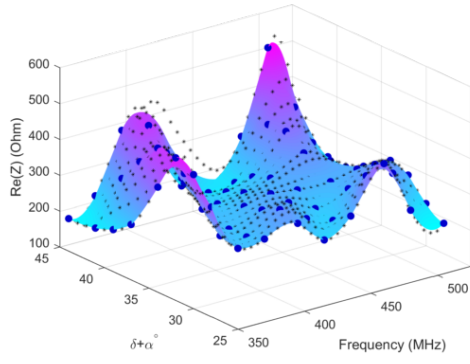
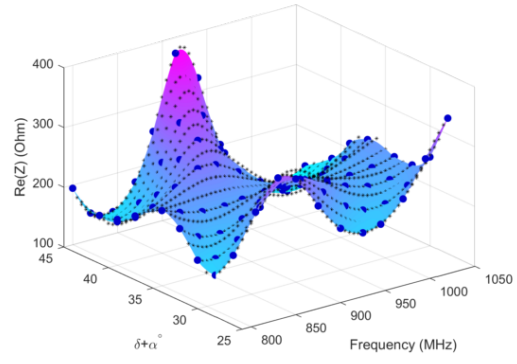
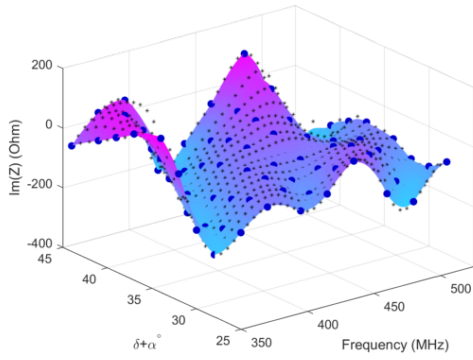
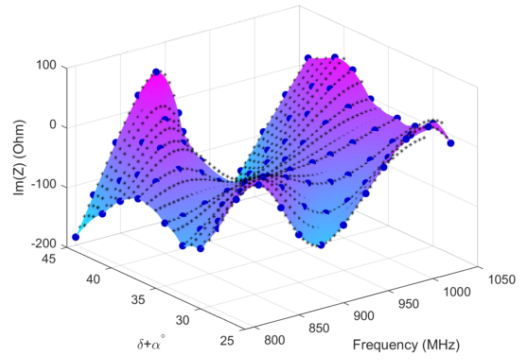
(a) $K_H = 72, K_L = 612$.(b) $K_H = 96, K_L = 901$.(c) $K_H = 72, K_L = 612$.(d) $K_H = 96, K_L = 901$.

Figure 5.23: Rational interpolants of the input impedance of the pyramidal sinuous antenna for variations in $\delta + \alpha$ and frequency when using equations (5.46) and (5.39) on the complex data. $\tau = 0.825$, $\delta/\alpha = 0.6$ and $\theta = 53^\circ$.

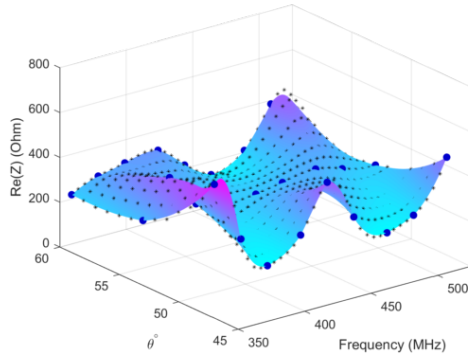
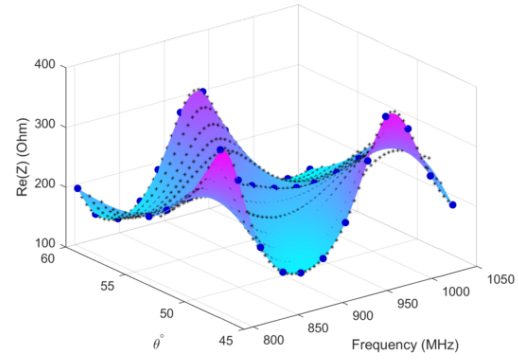
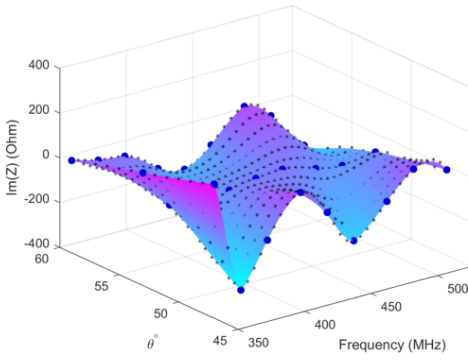
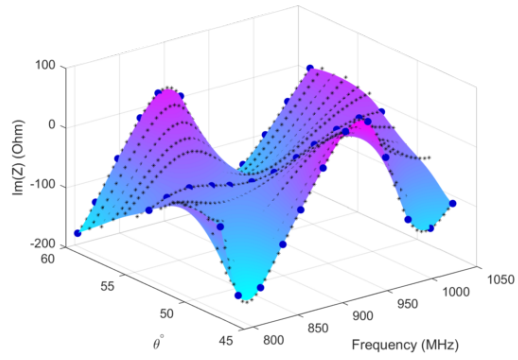
(a) $K_H = 27, K_L = 468$.(b) $K_H = 36, K_L = 689$.(c) $K_H = 27, K_L = 468$.(d) $K_H = 36, K_L = 689$.

Figure 5.24: Rational interpolants of the input impedance of the pyramidal sinuous antenna for variations in θ and frequency when using equations (5.46) and (5.39) on the complex data. $\tau = 0.825$, $\delta/\alpha = 0.6$ and $\delta + \alpha = 36^\circ$.

After the models for the input impedance are available, the reflection coefficients can be calculated according to equation (3.7) and then the worst case for each geometric parameter is determined. It is expected that the worst case is within the available frequency bands for each antenna. The solution is compared to the available validation data, shown in Figures 5.25 - 5.28.

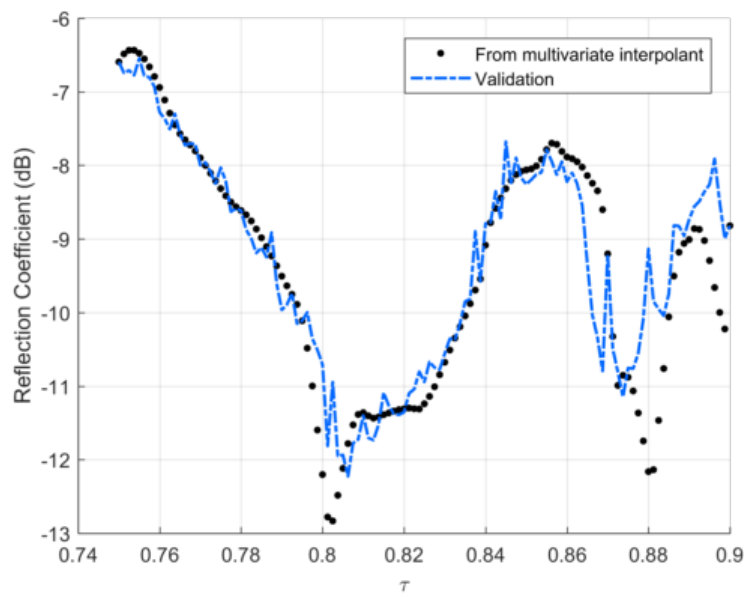


Figure 5.25: Worst case of the reflection coefficient for variations in τ determined from the rational approximants of Figure 5.21.

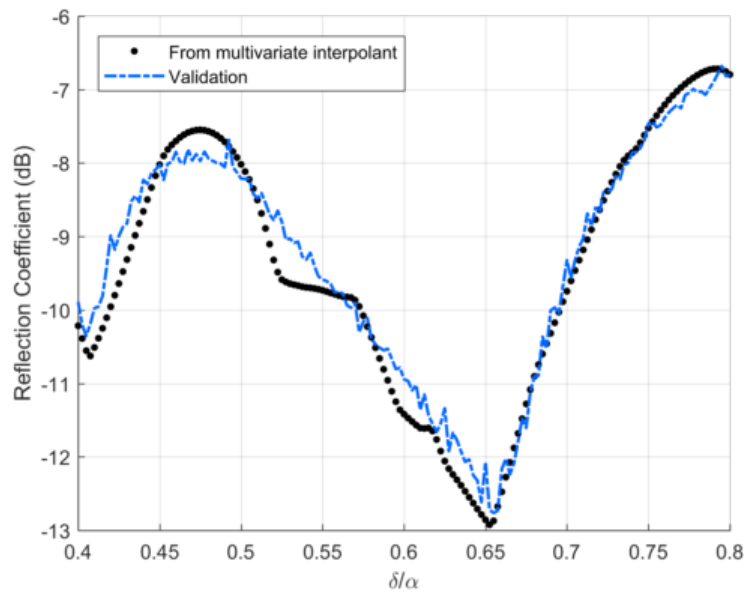


Figure 5.26: Worst case of the reflection coefficient for variations in δ/α determined from the rational approximants of Figure 5.22.

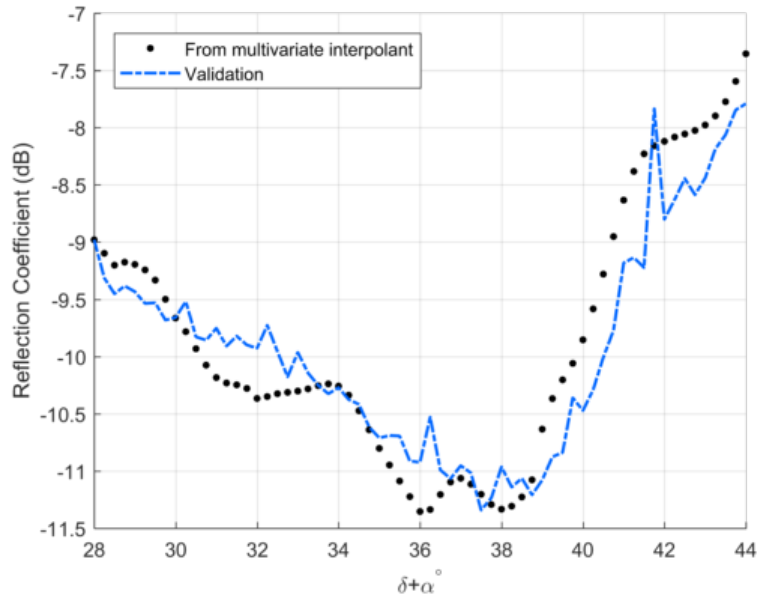


Figure 5.27: Worst case of the reflection coefficient for variations in $\delta + \alpha$ determined from the rational approximants of Figure 5.23.

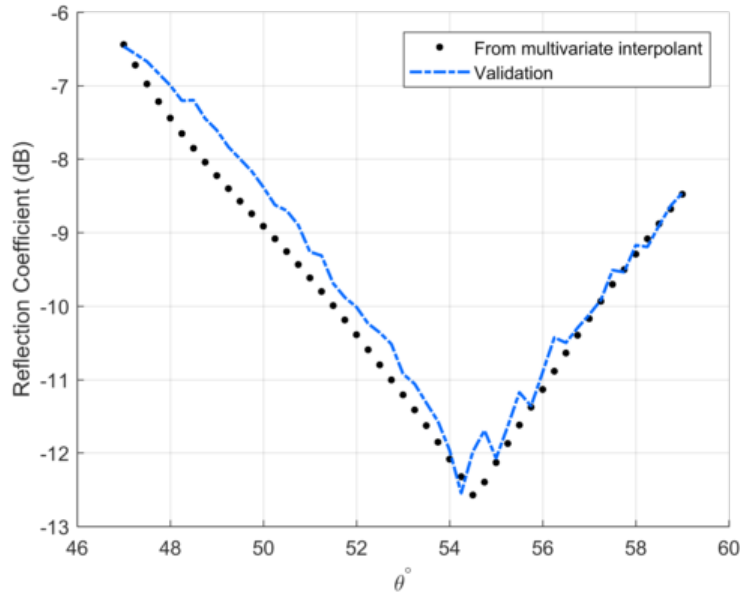


Figure 5.28: Worst case of the reflection coefficient for variations in θ determined from the rational approximants of Figure 5.24.

Error values were calculated for each model of the input impedance from equations (5.28) and (5.29) as well as on the data found for the reflection

coefficient in each case. These are shown in Tables 5.4 and 5.5.

Table 5.4: Error values for interpolants of Figures 5.21 - 5.24.

Model	AEE	MAX
Figure 5.21 (τ)	18.4189	153.3619
Figure 5.22 (δ/α)	9.3188	134.3906
Figure 5.23 ($\delta + \alpha$)	11.0163	115.7045
Figure 5.24 (θ)	10.9438	180.9171

Table 5.5: Error values for the reflection coefficient of Figures 5.25 - 5.28.

Data	AEE	MAX
Figure 5.25 (τ)	0.4181	3.0280
Figure 5.26 (δ/α)	0.2679	0.9674
Figure 5.27 ($\delta + \alpha$)	0.3239	0.9945
Figure 5.28 (θ)	0.3208	0.7041

The validation data in Figures 5.25 - 5.28 are seen to contain a lot of noise (note the rapid variations in the data). This is expected, since solutions in FEKO are evaluated on a discrete number of mesh triangles. This discretisation is a source of noise. However, the rational models are capable of capturing the general trend of the worst case of the reflection coefficient over variations of each geometric parameter quite well. Note, however, that the maximum error for the reflection coefficient over variations in τ is more than three times larger than for the other geometric parameters. This is because of the rapid variations which are observed in the general trend of Figure 5.25 for $\tau > 0.86$ (thus, not the noisy variations). The pyramidal sinuous antenna contains a discrete number of radiating cells which is exponentially dependent on the value of τ . This discretisation introduces an additional source of noise to the antenna's performance as a function of τ and variations in the output vary more and more rapidly as τ increases.

The data from Figures 5.25 - 5.28 can be used to determine the regions in the parameter space where the reflection coefficient is below -10 dB over the entire band. From this parameter space, the antenna with the maximum sensitivity can be identified. Chapters 6 and 7 consider this where models are built in higher dimensional spaces. The next section thoroughly compares the above method with other available surrogate models.

5.7 Comparisons of the B-Spline Blended Rational Interpolant with Other Surrogate Models

In order to assess the quality of the B-Spline blended rational interpolant, it is necessary to compare its modelling capabilities with more obvious or well-known modelling schemes which might be easier to implement than the above method. A thorough investigation was done which compares this model to five other interpolation methods. The most straightforward interpolation scheme is to apply a spline function to the available data. This was considered on the HF data alone, as well as on the calibrated LF data. Comparisons with these models answer the question of whether it is worthwhile to apply a rational interpolant to the available data. It is known that the underlying phenomena of electromagnetic systems takes on the form of a rational function, as was discussed in Section 3.2, thus the assumption is that a rational model would perform better than applying a straightforward spline function to the data. In particular, the error values were compared as the number of HF data points were decreased. Comparisons were also made with the barycentric rational interpolant of equation (5.14) when condition (5.15) is imposed, i.e. a rational interpolant that makes use of HF data only. In addition, two well-established surrogate modelling schemes were considered, namely Kriging and co-Kriging. Kriging makes use of HF data only, whereas co-Kriging is an extension to the Kriging interpolation scheme which makes use of multi-fidelity data. A brief discussion of the basics of these models follow.

Kriging Interpolation

Kriging is a Gaussian process based surrogate modelling technique which is commonly used in geostatistics. It was first described by Krige in his Master's thesis in 1951 [63] with the theoretical basis for the method developed in 1963 by Matheron [64]. The ooDACE MATLAB toolbox [65] was used to implement the Kriging and co-Kriging models in this section. An overview of the mathematical description is provided here - further details can be found in the toolbox's starting guide. For a data set of n function values $\mathbf{y} = \{y^1, \dots, y^n\}$ given at the samples points $X = \{\mathbf{x}^1, \dots, \mathbf{x}^n\}$ in d dimensions, the Kriging model is defined as

$$Y(\mathbf{x}) = f(\mathbf{x}) + Z(\mathbf{x}) \quad (5.48)$$

where $f(\mathbf{x})$ is a regression function and Z is a Gaussian process with mean zero, variance σ^2 and a correlation matrix Ψ . The function $f(\mathbf{x})$ captures the general trend of the data, while the Gaussian process Z is constructed so as to interpolate through the residuals. Ordinary kriging, used here, assumes a constant regression function $f(\mathbf{x}) = \alpha_0$. The $n \times n$ correlation matrix is defined

as

$$\Psi = \begin{pmatrix} \psi(\mathbf{x}^1, \mathbf{x}^1) & \dots & \psi(\mathbf{x}^1, \mathbf{x}^n) \\ \vdots & \ddots & \vdots \\ \psi(\mathbf{x}^n, \mathbf{x}^1) & \dots & \psi(\mathbf{x}^n, \mathbf{x}^n) \end{pmatrix}. \quad (5.49)$$

The choice of correlation function $\psi(\mathbf{x}, \mathbf{x}')$ is a crucial step in building an accurate Kriging model. In this case, a Gaussian correlation function was used, defined as

$$\psi(\mathbf{x}, \mathbf{x}') = \exp \left(- \sum_{i=1}^d \theta_i |x_i - x'_i|^p \right) \quad (5.50)$$

with $p = 2$. A Gaussian correlation function is suitable for a smooth surface response, while an exponential correlation function ($p = 1$) is better suited for a rough response. The correlation function is dependent on the distance between two points - points that are closer together have a greater influence on each other, so the function values are closer together. As the distance between points increase, their correlation goes to zero. The set of hyperparameters, $\theta_1, \dots, \theta_d$, describes a sphere of influence that a point has on nearby points for each dimension. It controls how fast the correlation function drops to zero, with lower values corresponding to a larger sphere of influence and higher values corresponding to a smaller sphere of influence. These are found by Maximum Likelihood Estimation (MLE), details of which can also be found in the ooDACE toolbox's starting guide. Optimisation of the hyperparameters is useful, since they control the amount of variation of the model in its different dimensions, where lower values lead to smoother variations and higher values lead to more rapid variations.

Co-Kriging

Co-Kriging is an extension of Kriging which exploits multi-fidelity data. Essentially, the co-Kriging surrogate modelling technique constructs two Kriging models - first on the LF data and then on the residuals of the HF and LF data. This process increases the accuracy of the model. Some experimentation was done to determine the best correlation function and it was found that the Matérn correlation function [66] provided the best results for the example which was tested. It is defined as

$$\psi(\mathbf{x}, \mathbf{x}')_{v=3/2} = (1 + \sqrt{3}l) \exp(-\sqrt{3}l) \quad (5.51)$$

with

$$l = \sqrt{\sum_{i=1}^d \theta_i (x_i - x'_i)^2}. \quad (5.52)$$

When multiple surrogate modelling experiments were run with the number of HF points varying, the correlation matrix of (5.49) was often ill-conditioned,

and thus a model could not be built. In these cases the error values are not available. This is a disadvantage of using co-Kriging surrogate models - some experimentation or knowledge of the system is needed to determine the best correlation function to be used. Table 5.6 lists the names and details of the different surrogate models which were compared.

Table 5.6: Surrogate models used in the comparison study.

Model Name	Data used	Details
Spline on HF	HF	Fits a spline using only the high-fidelity data which is available.
Spline on LF_c	MF	Fits a spline using the calibrated LF data (which coincides with the available HF data).
Barycentric	HF	Equation (5.40).
B-Spline blended rational interpolant	MF	Equation (5.46).
Kriging	HF	Equation (5.48) with a Gaussian correlation function.
Co-Kriging	MF	Makes use of the Matérn correlation function.

The figures to follow indicates the results of comparisons of the error values of each model, for a varying amount of HF points.

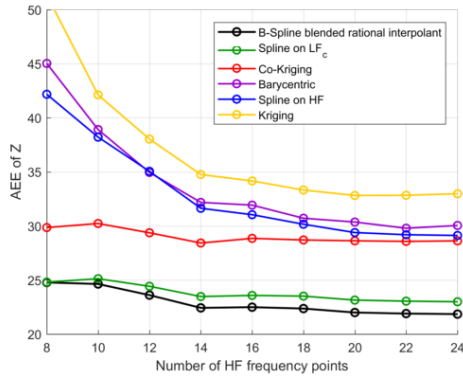
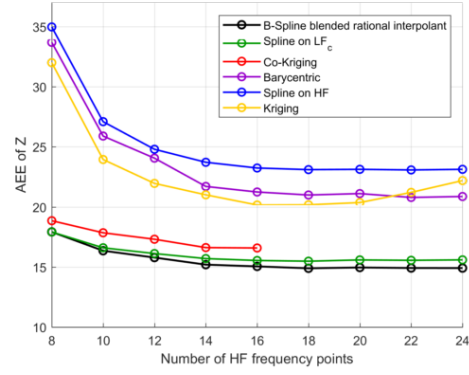
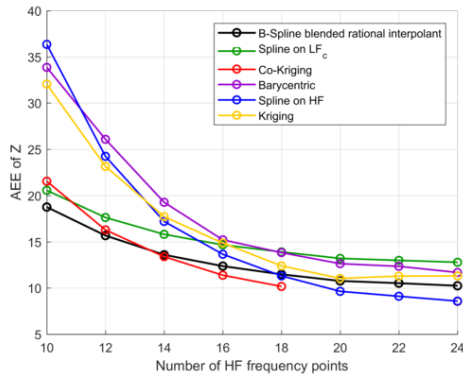
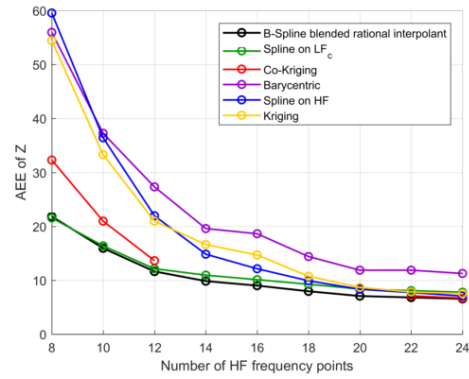
(a) # HF τ points = 9.(b) # HF δ/α points = 4.(c) # HF $\delta + \alpha$ points = 10.(d) # HF θ points = 9.

Figure 5.29: Comparisons of the AEE for the models listed in Table 5.6 as a function of the number of HF frequency points for the different geometric parameters.

Figures 5.29a) and 5.29b) indicates that the B-Spline blended rational interpolant performs better than all other models and Figure 5.29d) shows that the co-Kriging interpolant performs similarly to the B-Spline blended interpolant when the number of frequency points are equal to 22 and 24. However, for many cases the correlation matrix of the co-Kriging model was ill-conditioned and thus no model could be built. In figure 5.29c), it is seen that when the number of frequency points are more than 18, the spline interpolant on the HF data performs the best, but as the number of HF points are decreased, the B-Spline blended interpolant performs significantly better than the spline on HF. Since our goal is to minimise the number of HF points required for an accurate model, in order to reduce computation time, this is a favourable result.

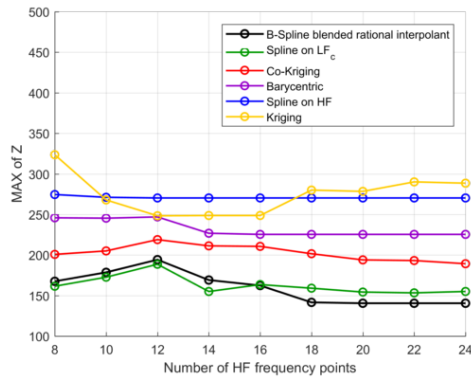
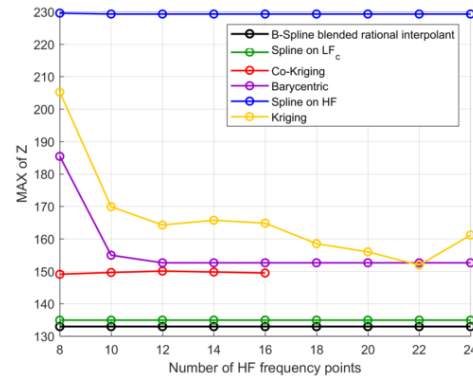
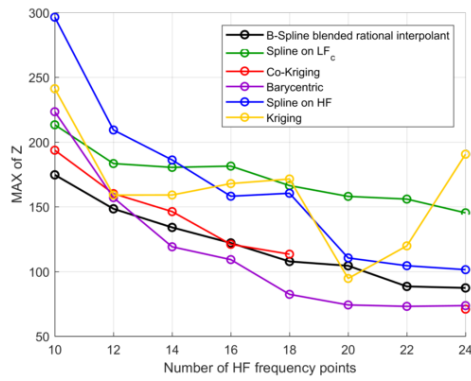
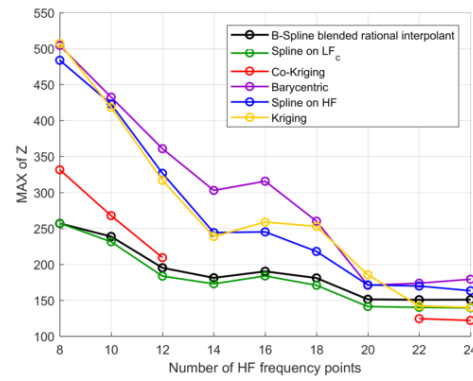
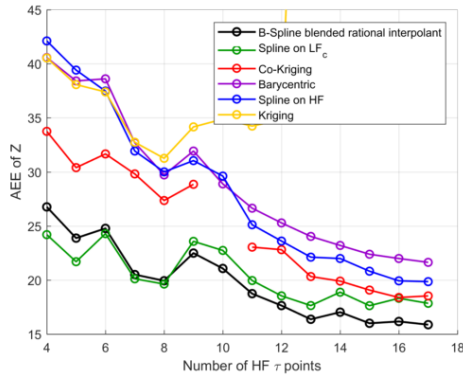
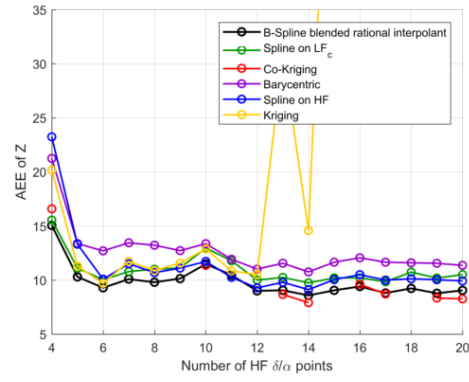
(a) # HF τ points = 9.(b) # HF δ/α points = 4.(c) # HF $\delta + \alpha$ points = 10.(d) # HF θ points = 9.

Figure 5.30: Comparisons of the MAX for the models listed in Table 5.6 as a function of the number of HF frequency points for the different geometric parameters.

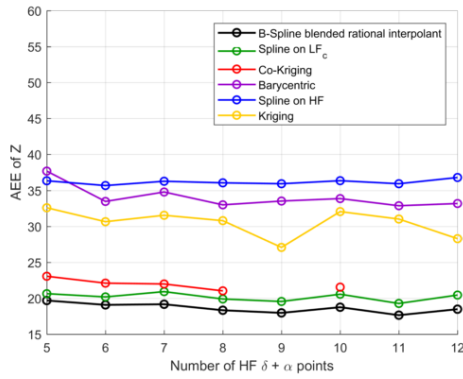
For the maximum errors shown in Figure 5.30, the spline interpolant on the calibrated LF data performs comparatively well to the B-Spline blended interpolant, except in Figure 5.30c) where it is seen that the barycentric interpolant performs the best for the number of HF frequency points higher than 14. This is an unexpected result, but as seen in the other figures, it is not a consistent result. Also, when the number of HF points decrease, once again the B-Spline blended rational interpolant performs the best. It is expected that the B-Spline blended rational interpolant would perform better than the spline interpolant on the calibrated LF data if the number of LF data points were decreased, however, this was not tested.



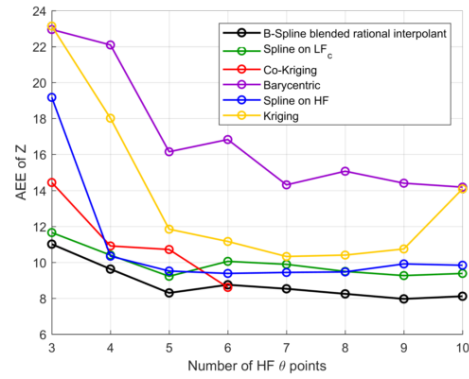
(a) # HF frequency points = 16.



(b) # HF frequency points = 16.



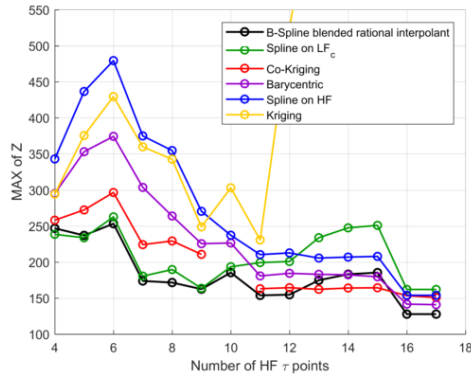
(c) # HF frequency points = 10.



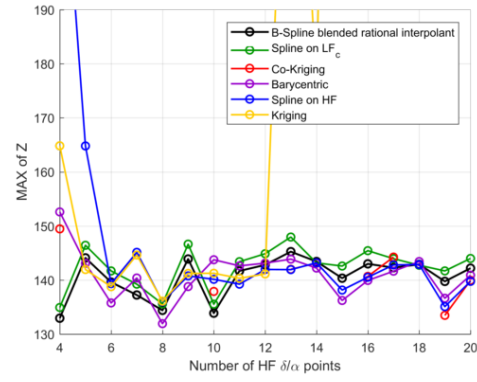
(d) # HF frequency points = 18.

Figure 5.31: Comparisons of the AEE for the models listed in Table 5.6 as a function of the number of HF geometry points for the different geometric parameters.

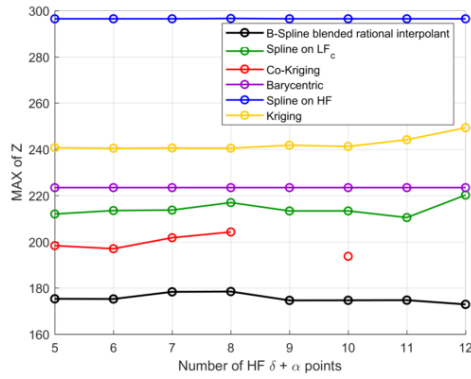
Most of the results in Figure 5.31 indicates that the B-Spline blended rational interpolant performs the best. In figure 5.31a) it is seen that the spline interpolant on the calibrated LF data exceeds the results of the B-Spline blended rational interpolant when the number of HF τ points are less than 8. In general though, since the underlying physical behaviour of the input impedance is known to be well modelled with a rational function, the B-Spline blended rational interpolant is preferred.



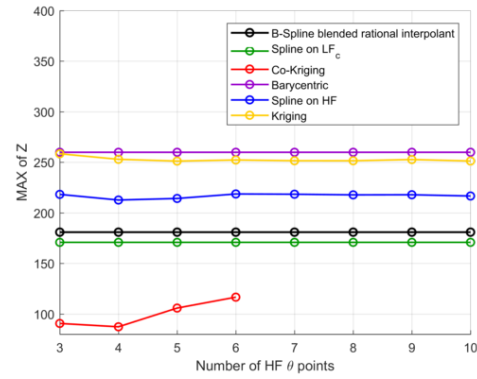
(a) # HF frequency points = 16.



(b) # HF frequency points = 16.



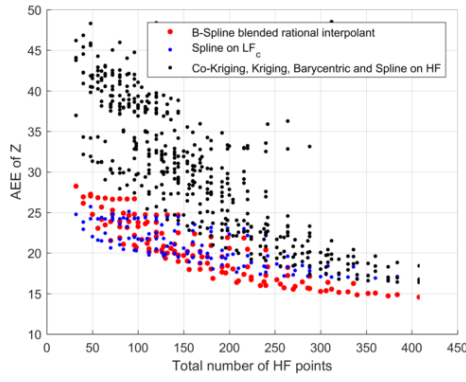
(c) # HF frequency points = 10.



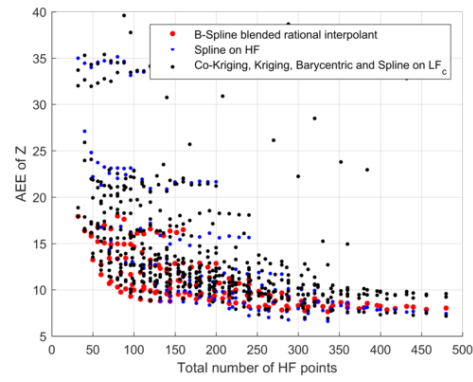
(d) # HF frequency points = 18.

Figure 5.32: Comparisons of the MAX for the models listed in Table 5.6 as a function of the number of HF geometry points for the different geometric parameters.

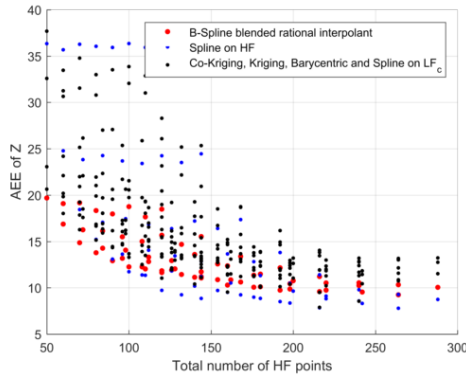
Figure 5.32a) shows the B-Spline blended rational interpolant performing the best in most cases and a significant benefit of this model is seen in figure 5.32c). In figure 5.32b) it is difficult to point to a model which performs the best, however the Kriging interpolant and the spline interpolant on the HF data is seen to have very high errors in certain cases - the specific values are not shown, in order to still be able to see the other error values. Figure 5.32d) show co-Kriging performing very well when the number of HF θ points are below 6, however, once again, in most cases, this model is unreliable.



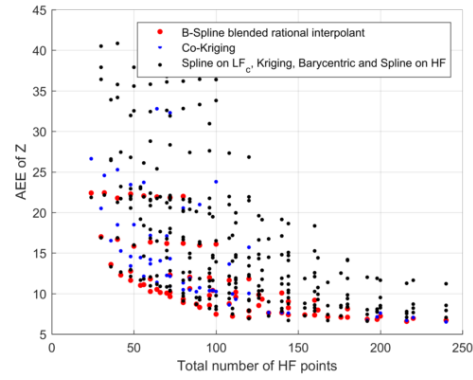
(a) Variations in frequency and τ .
 $\delta/\alpha = 0.6$, $\delta + \alpha = 36^\circ$ and $\theta = 53^\circ$.



(b) Variations in frequency and δ/α .
 $\tau = 0.825$, $\delta + \alpha = 36^\circ$ and $\theta = 53^\circ$.



(c) Variations in frequency and $\delta + \alpha$.
 $\tau = 0.825$, $\delta/\alpha = 0.6$ and $\theta = 53^\circ$.



(d) Variations in frequency and θ .
 $\tau = 0.825$, $\delta/\alpha = 0.6$ and $\delta + \alpha = 36^\circ$.

Figure 5.33: Comparisons of the AEE for the models listed in Table 5.6 as a function of the total number of HF points for the different geometric parameters. For clarity, the B-Spline blended rational interpolant is indicated by the red dots, and the model which compared the best is shown in blue, with all other models shown as black dots.

In Figure 5.33 the benefit of using the B-Spline blended rational interpolant can clearly be seen, especially when the number of HF data points become very few. The spline interpolant on the calibrated LF data performs very well in Figure 5.33a), however this result is not consistent.

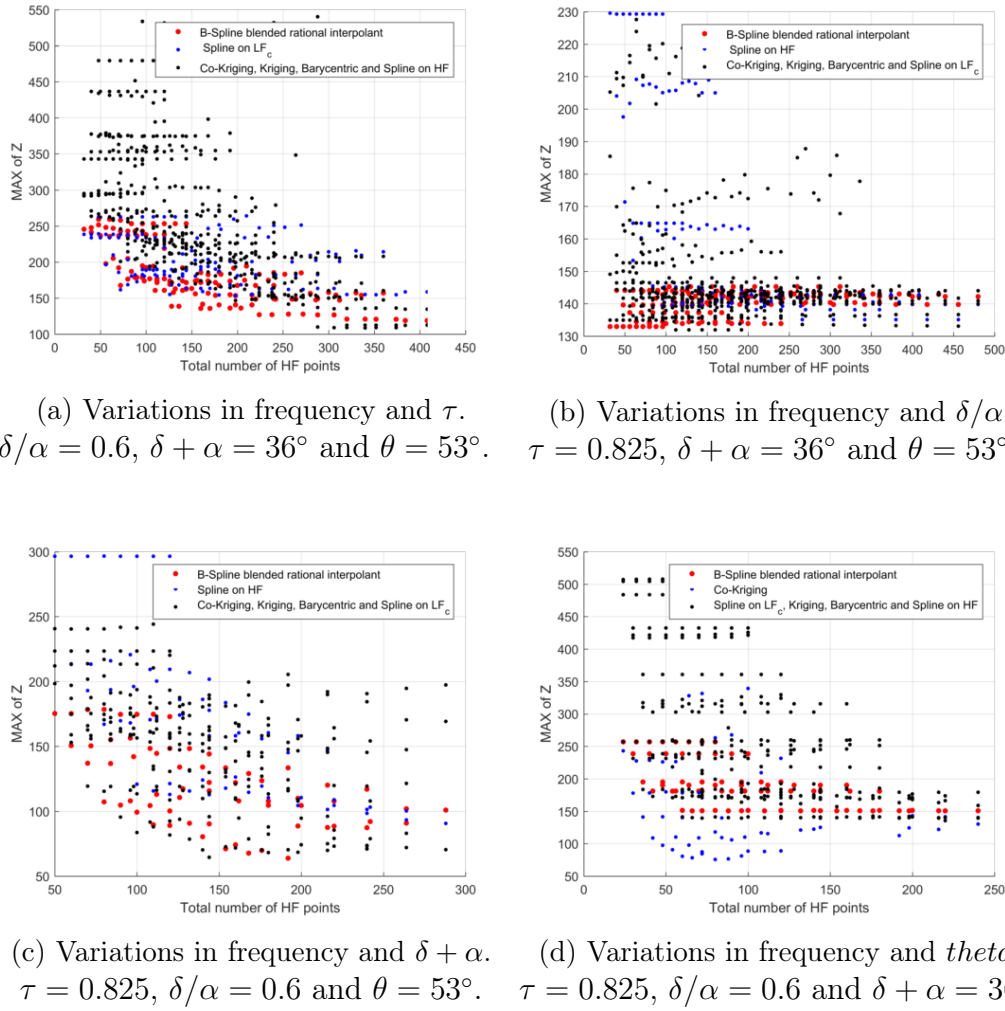


Figure 5.34: Comparisons of the MAX for the models listed in Table 5.6 as a function of the total number of HF points for the different geometric parameters. For clarity, the B-Spline blended rational interpolant is indicated by the red dots, and the model which compared the best is shown in blue, with all other models shown as black dots.

Once again, the benefit of the B-Spline blended rational interpolant is clearly seen in Figures 5.34a) and 5.34b). Note that the black dots come from different models, thus in Figure 5.34c) there is no clear contender to the B-Spline blended rational interpolant. In Figure 5.34d), co-Kriging is seen to perform very well. Careful design of a co-Kriging model could be a suitable substitute for a surrogate model of the input impedance of the pyramidal sinusoidal antenna, however, care must be taken to ensure that the correlation matrix does not become ill-conditioned. The simplicity and general performance of the B-Spline blended rational interpolant leads to the conclusion that this is the most useful model to use.

Chapter 6

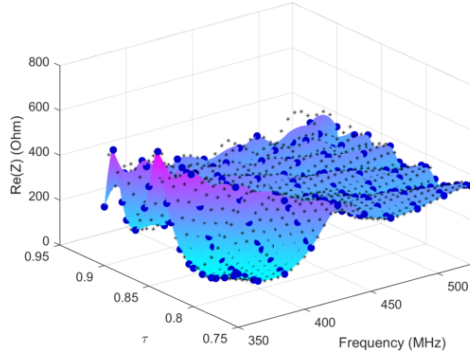
Design Examples

In this chapter, the methods that were developed in the previous two chapters are applied to two different design examples. Firstly, the surrogate models that were constructed are applied to a pyramidal sinuous antenna with a 5:1 bandwidth. This is done to illustrate the significant reduction in design time that is achieved when using these methods. Secondly, a design of the 3:1 bandwidth pyramidal sinuous antenna is considered where two geometric parameters are varied simultaneously. This design utilises very few HF points over the frequency bands of interest. The region where the worst case of the reflection coefficient is below -10 dB is found from three-dimensional rational interpolants. The results are compared to those from the fine model validation data. It was found that only 1.13% of the true region is not covered by the predicted region. It was also seen that these models erroneously predict 10.77% of the domain to be in this region. A surrogate model was built for the sensitivity of the system and the maximum sensitivity was identified from the region of interest.

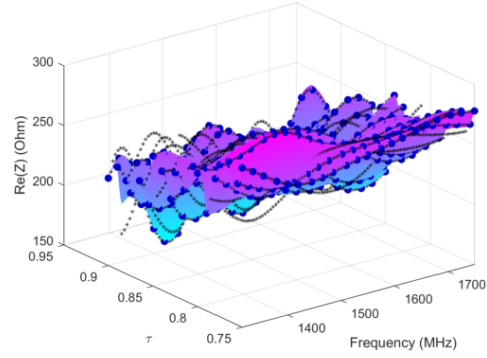
6.1 Surrogate Models of the Performance Metrics of a 5:1 Pyramidal Sinuous Antenna

In order to illustrate the significant speed-up that is possible when designs are done using the surrogate models introduced in Chapters 4 and 5, an example was done on a pyramidal sinuous antenna with a 5:1 bandwidth, from 350 - 1750 MHz. Rational interpolants were built on the band edges, using coarse model data from truncated antenna structures, as described in Section 3.3, with the low frequency band from 350 - 525 MHz and the high frequency band from 1315 - 1750 MHz. This starting value for the high frequency band was once again chosen to simplify sampling of points on a grid for the coarse model LF evaluations. Figure 6.1 illustrates the rational interpolants done

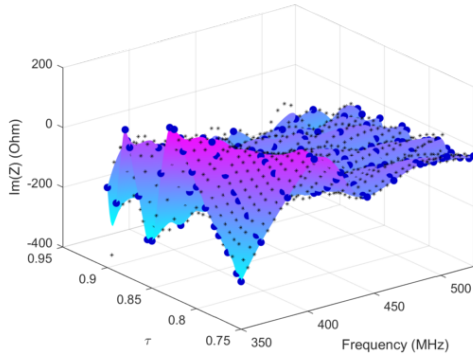
in two dimensions, with variations of the geometric parameter $\tau \in [0.75, 0.9]$. The number of HF and LF points that were used in each case are shown in the figures.



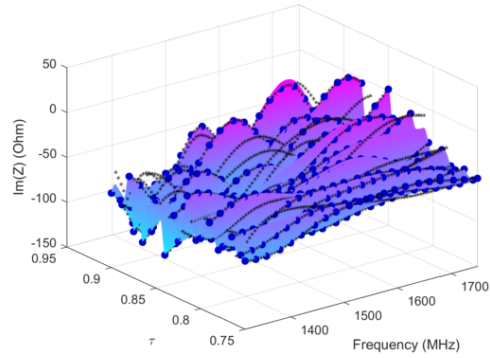
(a) $K_H = 190, K_L = 1116$.



(b) $K_H = 399, K_L = 2728$.



(c) $K_H = 190, K_L = 1116$.



(d) $K_H = 399, K_L = 2728$.

Figure 6.1: Rational interpolants of the input impedance of a 5:1 pyramidal sinuous antenna for variations in τ and frequency when using equations (5.46) and (5.39) on the complex data. $\delta/\alpha = 0.6$, $\delta + \alpha = 36^\circ$ and $\theta = 53^\circ$.

From these interpolants, the worst case of the reflection coefficient can be evaluated. Recall that the worst case is expected to lie in the band edges for a log-periodic antenna. Figure 6.2 shows the results against validation data from the full fine model.

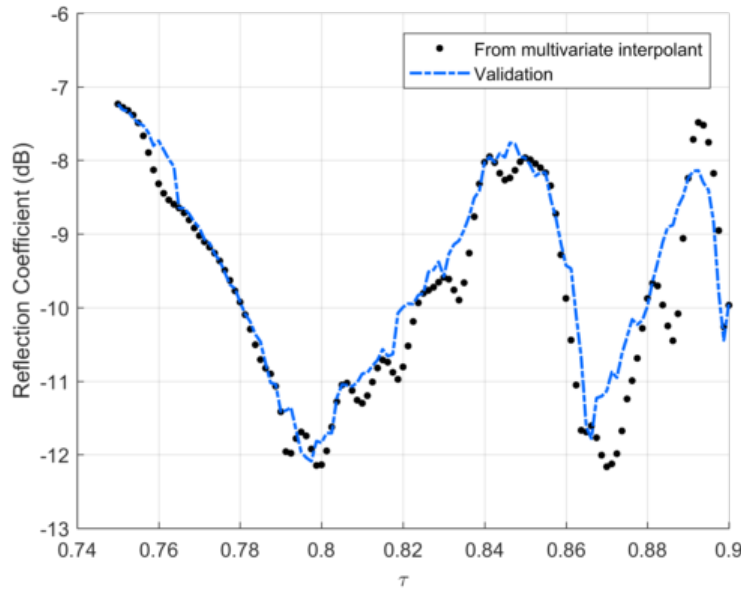


Figure 6.2: Worst case of the reflection coefficient for variations in τ determined from the rational approximants of Figure 6.1.

The error values for the above results are listed in Table 6.1.

Table 6.1: Error values for the rational interpolation model of a 5:1 pyramidal sinuous antenna.

Performance metric	AEE	MAX
Input impedance	15.2	133.3
Reflection coefficient	0.332	1.57

The sensitivity surrogate model described as Model 3 in Section 4.2 was then applied to this 5:1 example for variations in τ , where the radiation patterns of the truncated antenna structures are used in the simplified equation (4.12) to generate the coarse sensitivity model. The radiation pattern of the full antenna structure is evaluated at three points for τ and the sensitivity is evaluated at these points using the main reflector masking technique described in Section 2.4. A surrogate is constructed by fitting a second-order polynomial regression term to the difference between coarse and fine model evaluations at these points. The objective function $U^{(a)}$ is used. Figure 6.3 shows the results from this procedure, with error values listed in Table 6.2.

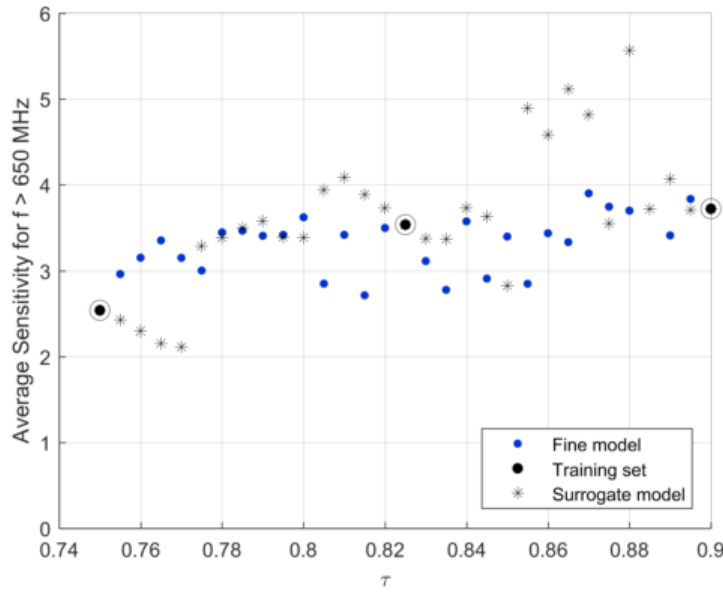
Figure 6.3: Sensitivity surrogate for Model 3a) with variations in τ .

Table 6.2: Error values for the sensitivity surrogate model of a 5:1 pyramidal sinuous antenna.

Performance metric	AEE	MAX
Sensitivity	0.622	2.04

Unfortunately, there are some outliers in the sensitivity surrogate model which are seen not to follow the trend of the fine validation data. Searching for the optimal sensitivity point in the region where the reflection coefficient is -10 dB would lead to one of these outliers being chosen, as it lies above the general trend of the sensitivity model. Once this point is chosen, upon validating the design and seeing that it is largely erroneous, this point can be used as an additional fine model data point, so that the design can be updated and improved.

Table 6.3 lists the time required to build the above models. Specifically, the time that would be required to build the full fine model for each performance metric, namely sensitivity and the reflection coefficient, is compared to the time that was required to build the respective surrogate models. Note that the time is listed in days.

Table 6.3: CPU time required for the different models for of a 5:1 pyramidal sinuous antenna.

Model	CPU time [Days]
Fine sensitivity model	166.6
Surrogate sensitivity model (Model 3)	29.8
Fine S_{11} model	654.5
Rational interpolants used to find the S_{11}	22.8

A total speed up factor of 15.6 is achieved when making use of the surrogate models as opposed to evaluating the full fine models in each case. This is a significant reduction in design time. If, after finding an optimal design from these models, the errors in the results are seen to be too large, the design can be redone to include more fine model evaluations, leading to increased accuracy.

6.2 Multi-Objective Optimisation of a 3:1 Pyramidal Sinuous Antenna

Ideally, the surrogate models that were introduced should be applied to find an optimal design of the pyramidal sinuous antenna over all variations of the geometric input parameters, i.e. for $\mathbf{x} = [\tau, \delta/\alpha, \delta + \alpha, \theta]$. However, since evaluation of the the input impedance with a rational interpolant which makes use of B-Spline blending functions requires evaluation of the coarse model structure on a grid of input parameters, the number of evaluations that are required as the dimensions are increased, rapidly grows. Due to time constraints, it was not possible to evaluate the design space over all parameters. An example was considered in three dimensions, with $\mathbf{x} = [\tau, \delta/\alpha]$ where $\delta + \alpha = 36^\circ$ and $\theta = 53^\circ$ for the same 3:1 bandwidth as in Chapter 5, i.e. from 350 - 1050 MHz, with the low band coarse model from 350 - 525 MHz and the high band coarse model from 790 - 1050 MHz. The grid that was evaluated is listed in Table 6.4, with $\tau \in [0.75, 0.9]$ and $\delta/\alpha \in [0.4, 0.8]$. As it is known that rational interpolants are well-suited to modelling the output behaviour of antenna structures as a function of frequency, it was possible to use very few HF points over the frequency domains. On the other hand, a relatively high value of HF points were required over the domains of the geometric parameters.

Table 6.4: Grid on which interpolants are built in three dimensions.

x_1	x_2	x_3	m_1	m_2	m_3	K_H	K_L
τ	δ/α	Frequency $\in [350, 525]$ (MHz)	22	22	5	2420	60516
τ	δ/α	Frequency $\in [790, 1050]$ (MHz)	22	22	5	2420	89093

The error values for these models are listed in Table 6.5. The maximum error value for the worst case of the reflection coefficient is seen to be quite high. Increasing the number of HF points reduced the average error, but the maximum error remained high. A trade-off exists between the error values and the design time. Figure 6.4 illustrates the absolute errors between the validation data and the predicted reflection coefficients from these rational interpolation models. It is seen that the error values are mostly below 2 dB over the domain of interest, so this design was deemed to be acceptable.

Table 6.5: Error values from the rational interpolation models built on the grid in Table 6.4.

Performance metric	AEE	MAX
Input impedance	17.2	202.8
Reflection coefficient	0.436	2.92

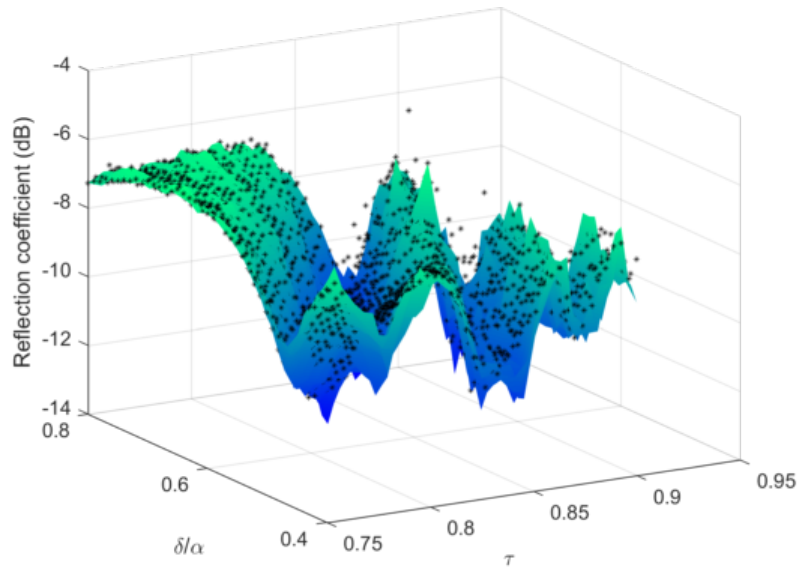


Figure 6.4: Worst case of the reflection coefficient for variations in τ and δ/α determined from the rational approximants.

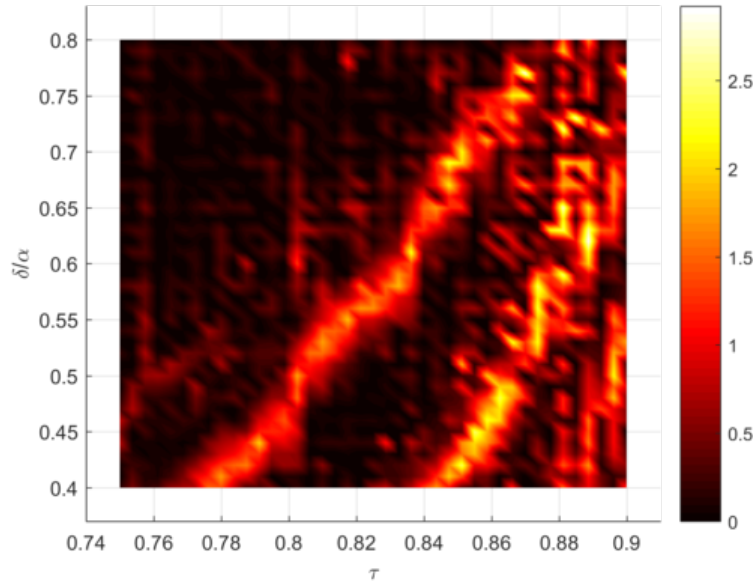


Figure 6.5: Error values for the worst case of the reflection coefficient for variations in τ and δ/α .

Since the design objective in this case is to maintain a reflection coefficient below -10 dB over the entire band, Figure 6.6 shows where the areas where the reflection coefficient is predicted to be less than -10 dB when using these rational interpolation models, as opposed to the area where this is truly the case, found from a set of fine model validation data. Table 6.6 lists the percentage of the areas that are below -10 dB in each case.

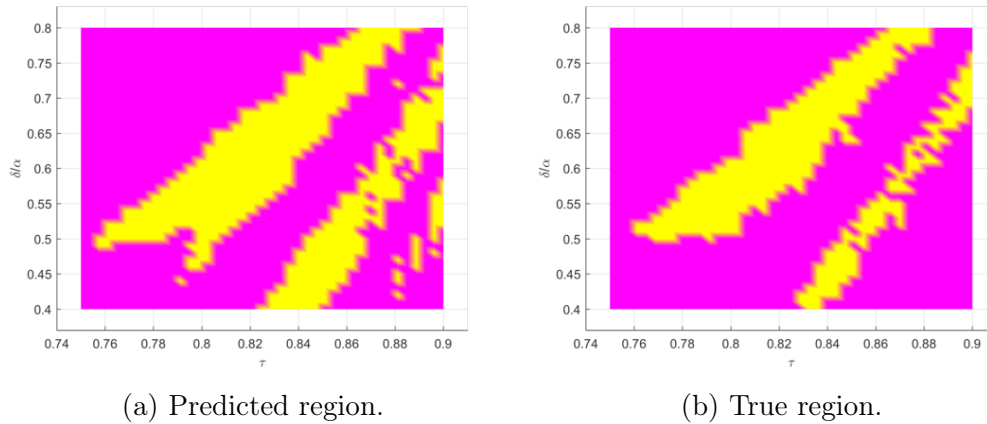


Figure 6.6: Regions where the worst case of the reflection coefficient for variations in τ and δ/α are less than -10 dB.

Table 6.6: Percentage of the area that has a reflection coefficient less than -10 dB.

	Area
Prediction from rational interpolants	33.4%
True evaluation	23.7%

Figure 6.7 illustrates the two areas shown in Figure 6.6 superimposed on each other. It was found that the predicted region nearly encompasses the true region, with only 1.13% of the true region not contained in the predicted region, thus this method includes 98.87% of the viable choices for this design.

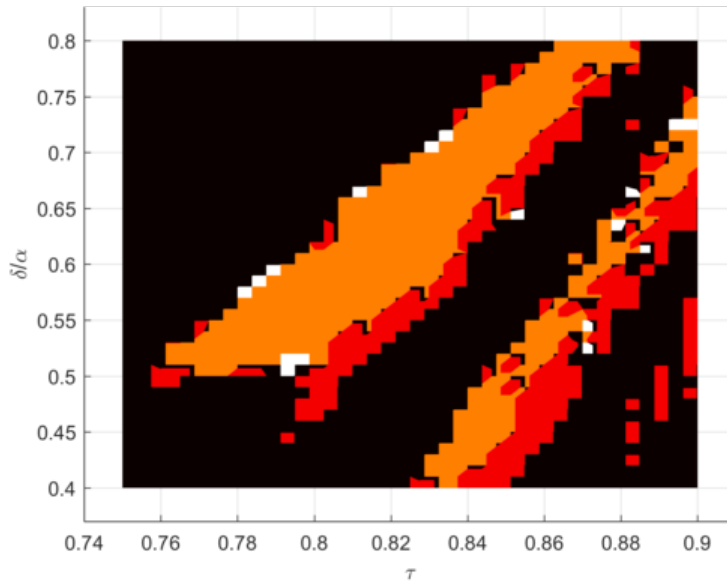


Figure 6.7: Comparison of regions where the worst case of the reflection coefficient for variations in τ and δ/α are less than -10 dB. The orange region indicates the true region below -10 dB and the red region indicates where the prediction is below -10 dB. The white areas are where the true region is below -10 dB, but the predicted value is not.

Since the predicted area is larger than the true area, this method may lead to an erroneous design. The method erroneously predicts 10.77% of the domain to be below -10 dB, leading to a total error in the overall prediction of 11.9%. If a faulty design is arrived at, the validation data found from the design must be used as an additional HF point in an attempt to improve the rational interpolant. This process can be repeated until an adequate design is arrived at.

A sensitivity surrogate model was also built for this domain using Model 3 as described in Section 4.2 with objective function $U^{(a)}$. The results are shown in Figure 6.8 with error values listed in Table 6.7.

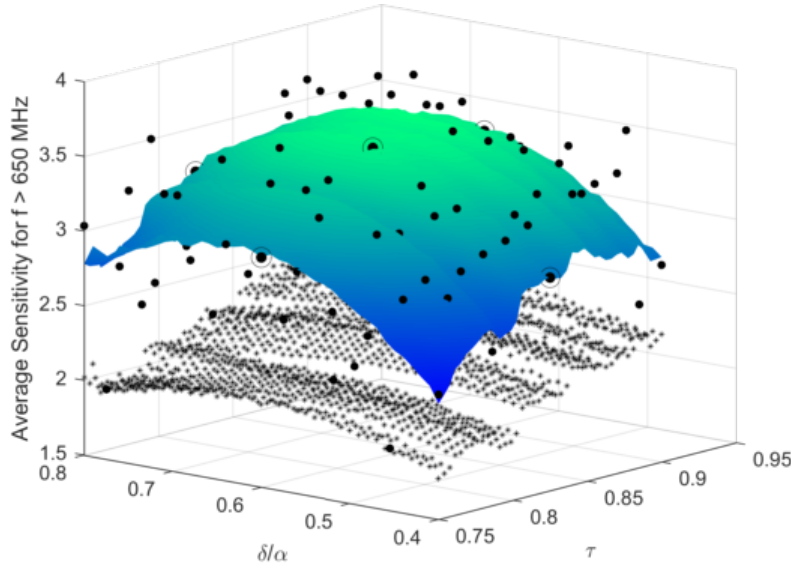


Figure 6.8: Sensitivity surrogate for Model 3a) with variations in τ and δ/α . Fine model validation data is indicated by black dots, coarse model data is indicated by stars and the training set for the regression term is shown encircled over a star distribution. The coloured surface indicates the surrogate model.

Table 6.7: Error values for the sensitivity surrogate models for variations in τ and δ/α .

Performance metric	AEE	MAX
Sensitivity	0.346	2.93

From the above surrogate models, the maximum sensitivity value in the region where the reflection coefficient is predicted to be below -10 dB was found to be an average of $3.651 \text{ m}^2/\text{K}$ at $\tau = 0.87375$, $\delta/\alpha = 0.63$, $\delta + \alpha = 36^\circ$ and $\theta = 53^\circ$. A full wave solution of the fine model structure revealed that this antenna structure's reflection coefficient is indeed below -10 dB over the entire band, as shown in Figure 6.9.

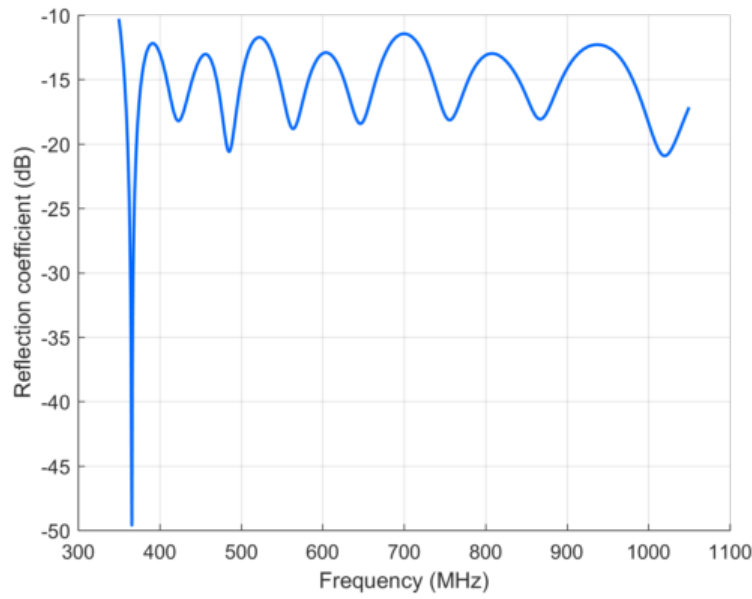


Figure 6.9: Reflection coefficient of the optimal design. $\tau = 0.87375$, $\delta/\alpha = 0.63$, $\delta + \alpha = 36^\circ$ and $\theta = 53^\circ$.

The reflection coefficient can be renormalised to an optimal input impedance. The results of doing this is shown in Figure 6.10. The optimal input impedance was found to be 237Ω . This makes the reflection coefficient less than -10.52 dB over the entire band.

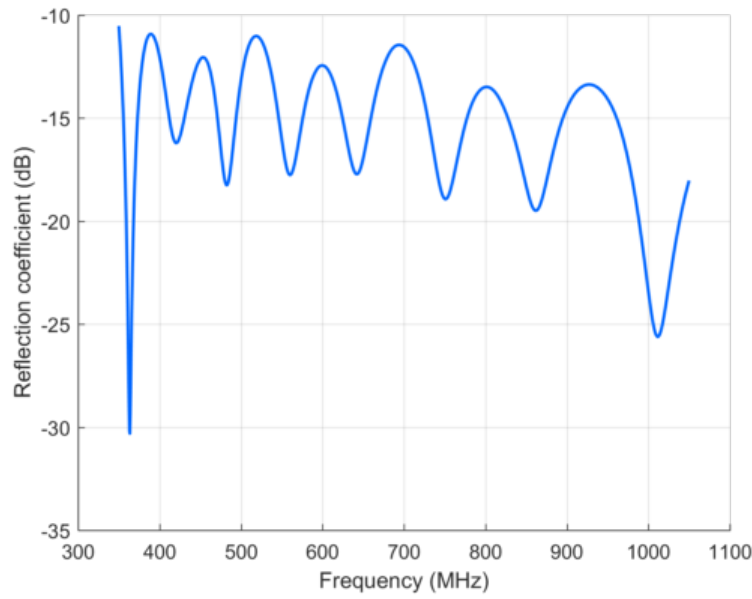


Figure 6.10: Reflection coefficient of the optimal design when renormalised to an input impedance of 237Ω . $\tau = 0.87375$, $\delta/\alpha = 0.63$, $\delta + \alpha = 36^\circ$ and $\theta = 53^\circ$.

The sensitivity of the antenna was validated and is shown in Figure 6.11 with the average sensitivity over the band equal to $3.7139 \text{ m}^2/\text{K}$, which exceeds the predicted value of $3.651 \text{ m}^2/\text{K}$.

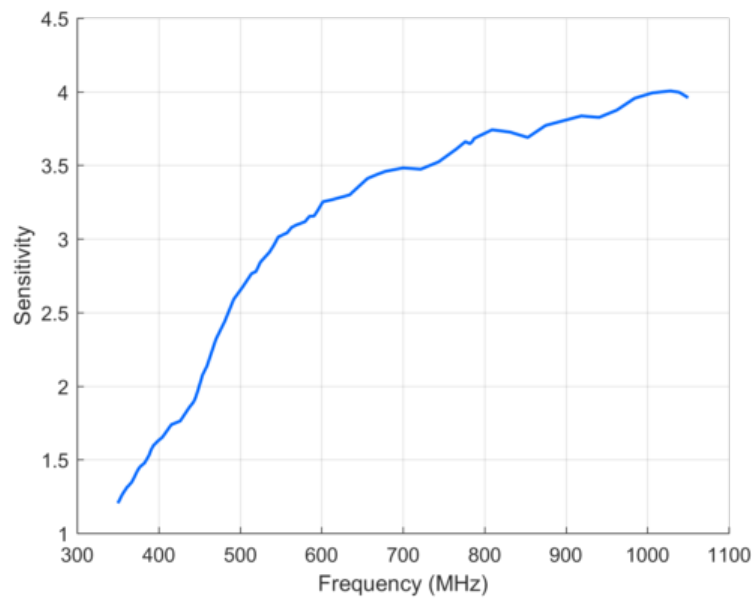


Figure 6.11: Sensitivity as a function of frequency for the optimal design. $\tau = 0.87375$, $\delta/\alpha = 0.63$, $\delta + \alpha = 36^\circ$ and $\theta = 53^\circ$. The average sensitivity is $3.7139 \text{ m}^2/\text{K}$.

Chapter 7

Conclusion and Further Recommendations

In this thesis the design of a pyramidal sinuous antenna for use as a feed in a reflector antenna system, such as the SKA, was considered. The focus was on creating accurate and efficient surrogate modelling techniques that are able to model the sensitivity as well as the reflection coefficient of the antenna structure. For this purpose, coarse models of the structure are required that are faster to evaluate than conventional full wave electromagnetic solver techniques. These coarse models contain inaccuracies, but it provides information about the performance of the antenna. Since the pyramidal sinuous antenna belongs to the class of log-periodic antennas, truncated models of the antenna structure that operate at the band edges of the full fine model are well-suited for this purpose. These structures are electromagnetically smaller than the fine model. Additionally, the operating bandwidth is reduced, leading to a significant speed-up in the simulation time of these structures.

An approximation of the noise temperature model of the system that makes use of a main reflector masking technique was used. The idea here is to remove the main reflector from the calculation domain, leading to a reduced electromagnetic size of the system and a consequent reduction in evaluation time. This method was used in the fine model of the sensitivity calculation. For the coarse model of the sensitivity calculation, the radiation patterns from the truncated antenna structures were used in an approximate equation of the efficiency of the system, which derives from the geometrical optics technique (equation (4.13)), along with a noise temperature equation that is dependent only on frequency (equation (4.14)). Thus there is no need to do a simulation of the dishes in GRASP. A surrogate model was then found from a simple output space mapping technique, where a corrective second-order polynomial regression term is applied to the differences between the fine and coarse model data points, with the fine model data points sampled over a star distribution.

Rational interpolation was used to model the input impedance of the pyramidal sinuous antenna, from which the reflection coefficient is calculated. Rational interpolants that make use of high-fidelity data only (acquired from the fine model structure) was considered first. As the number of these evaluations need to be minimised, in order to improve the accuracy of the models, multi-fidelity data was subsequently utilised. A weighted barycentric rational interpolant, which solves the weights by following the low-fidelity data (acquired from the coarse model structures) in a least squares sense was considered. To ensure that all interpolation points are attainable, it is necessary to have pole-free rational interpolation models. The condition which guarantees a pole-free region was seen to restrict the barycentric weights too much to be able to give useful results. A method was then constructed which makes use of Bèzier curves as local models that follow the trend of the LF data in the interval between each consecutive high-fidelity data points. These local models are then blended into a global rational interpolant by making use of quadratic B-spline blending functions. These interpolants were seen to perform well in one dimension. It was then extended to multiple dimensions, with examples in two dimensions where one dimension is a geometric parameter and the other is frequency. Using relatively few HF points, it was possible to predict the worst case of the reflection coefficient over the bandwidth of interest for each geometric parameter variation, with average error values below 0.42 dB in each case.

An in-depth study was done which compares the accuracy of this rational B-spline blending interpolation method to other well-known methods. Three models which make use of HF data points only were considered, namely spline interpolants, the barycentric rational interpolant and Kriging. Comparisons were made with multi-fidelity data models of spline interpolants and co-Kriging. The results from this study showed that the blended rational B-spline interpolant performed better than the other methods overall. Its simplicity also makes this model attractive.

An example of a 5:1 bandwidth design was shown in order to illustrate the significant speed-up that can be achieved using the surrogate models suggested in this thesis. A speed-up factor close to 16 was observed.

An optimisation example was shown where two of the geometric parameters were varied simultaneously - requiring a three-dimensional rational interpolant for the variation in frequency to be included. A good prediction of the region where the reflection coefficient is below -10 dB was found, with a total error of 11.9% over the domain. This was achieved by using only 5 HF points over each frequency band edge for every variation of the geometric parameters. From this predicted region, the geometric parameters of the antenna that led to the maximum average sensitivity value was identified as $3.651 \text{ m}^2/\text{K}$ at $\tau = 0.87375$, $\delta/\alpha = 0.63$, $\delta + \alpha = 36^\circ$ and $\theta = 53^\circ$. Validation of the sensitivity

at this point showed the average sensitivity to be equal to $3.7139 \text{ m}^2/\text{K}$ and the reflection coefficient was seen to be below -10.52 dB over the entire band.

Thus, in conclusion, the blended rational B-spline interpolation method looks promising, especially for predictions of antenna outputs as a function of frequency. A disadvantage of this method is that it requires the coarse model to be evaluated over a grid. As the dimensions of the domain increase, the number of evaluations that are required for accurate predictions increases exponentially, making the use of this model unattractive. A variant of this method that uses local models that do not require a grid of samples, as opposed to the local Bèzier curve models, could be explored in order to overcome this limitation. Additionally, an adaptive sampling technique that efficiently selects the position of the HF data points over the domain of interest could lead to improved accuracy of the model using fewer HF points. Since this method depends on the reliability of the coarse model data, it is important for the coarse model to be based on the physics of the problem. The truncated coarse model antenna structures are well-suited for modelling the behaviour of log-periodic structures in general, thus this interpolation method could easily be applied to other wideband log-periodic antenna structures.

As was discussed, rational interpolation functions are well-suited to model antenna behaviour in the frequency domain, so it is recommended to use as little as possible HF points over the frequency ranges of interest, while supplementing the method with more HF points in the domains of the geometric parameters. Furthermore, it is expected that this method would be able to accurately predict the output of other frequency-dependent performance metrics of the antenna, in addition to the input impedance.

A useful expansion of this work would be to include a realistic feed network to the antenna structure. In a concurrent study, it was seen that adding a feed network to the structure significantly complicates the design. Therefore, a simplified approach would be to optimise the structure of the pyramidal sinuous antenna first and then do a separate optimisation to find an appropriate feeding network. A large study would be required to properly explore this problem.

Lastly, if it is required that the antenna be optimised for additional performance metrics, then a formal multi-objective optimisation approach would be beneficial.

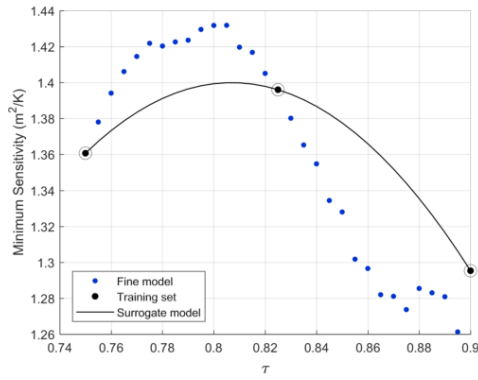
Appendices

Appendix A

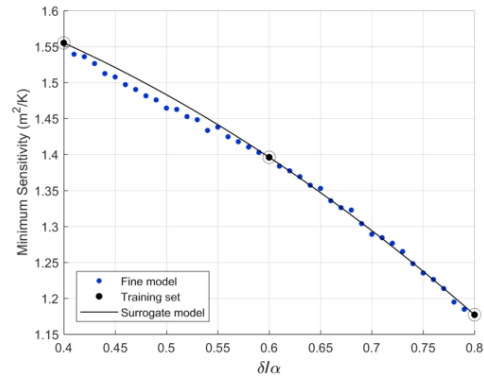
Results for Sensitivity Models

Results for the objective functions $U^{(b)}$ and $U^{(c)}$ of Chapter 4 are given below.

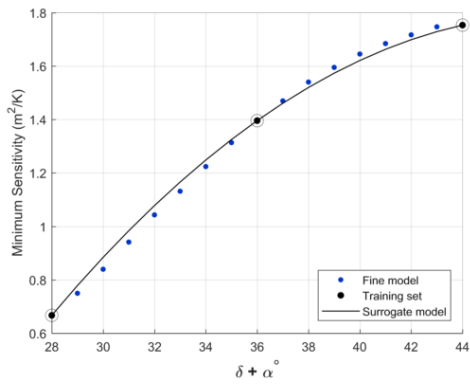
A.1 Model 1



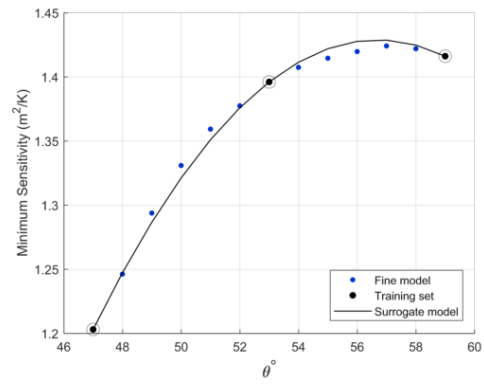
(a) Variations in τ .



(b) Variations in δ/α .



(c) Variations in $\delta + \alpha$.



(d) Variations in θ .

Figure A.1: Sensitivity surrogates for Model 1 of the objective function $U^{(b)}$.

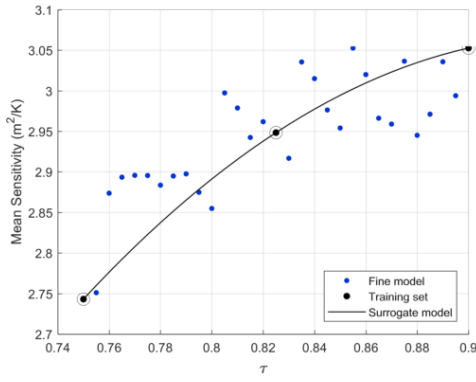
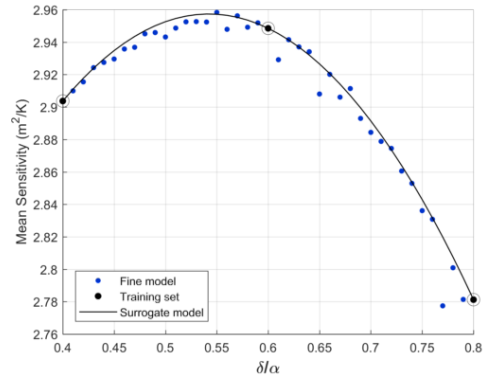
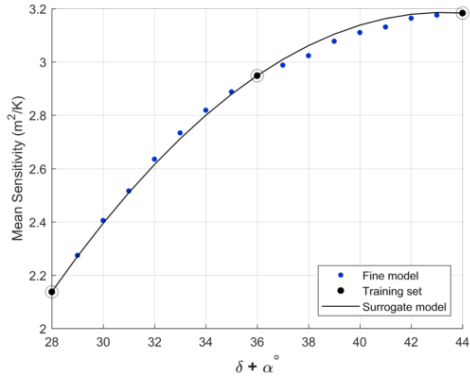
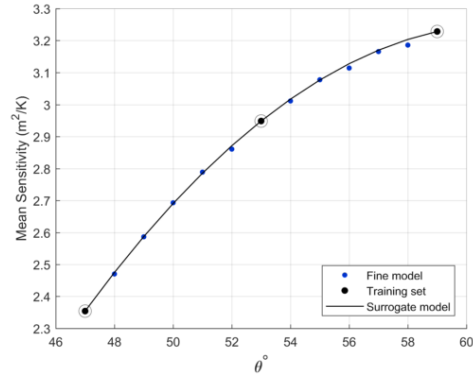
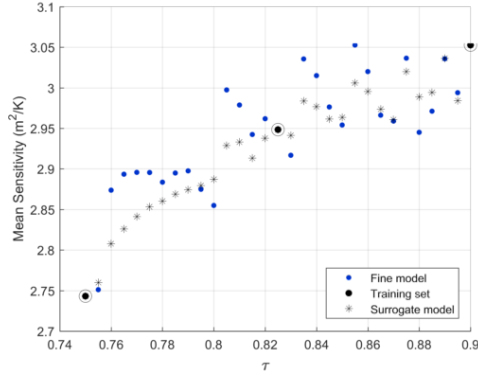
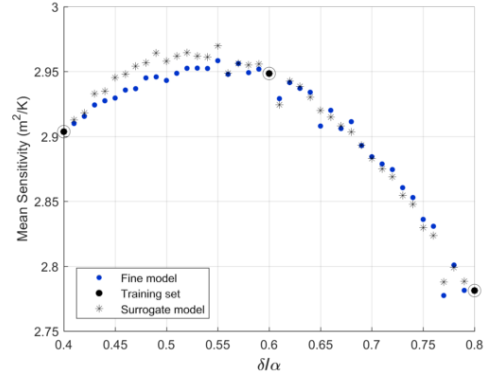
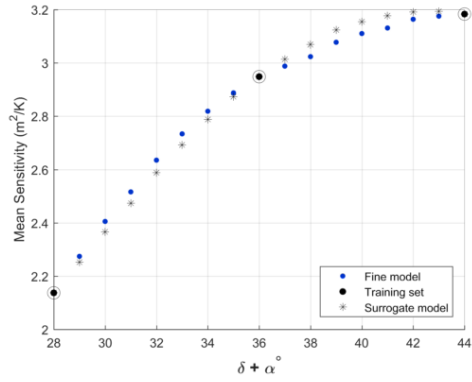
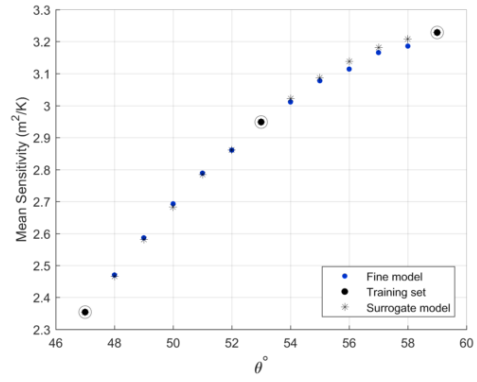
(a) Variations in τ .(b) Variations in δ/α .(c) Variations in $\delta + \alpha$.(d) Variations in θ .Figure A.2: Sensitivity surrogates for Model 1 of the objective function $U^{(c)}$.

Table A.1: Percentage errors for Model 1.

Model	Parameter	ARE [%]	MRE [%]
b)	τ	1.46	3.50
	δ/α	0.18	1.53
	$\delta + \alpha$	0.53	1.24
	θ	0.17	0.56
c)	τ	2.54	6.03
	δ/α	0.45	1.27
	$\delta + \alpha$	1.83	5.29
	θ	0.31	0.73

A.2 Model 2

(a) Variations in τ .(b) Variations in δ/α .(c) Variations in $\delta + \alpha$.(d) Variations in θ .Figure A.3: Sensitivity surrogates for Model 2 of the objective function $U^{(b)}$.

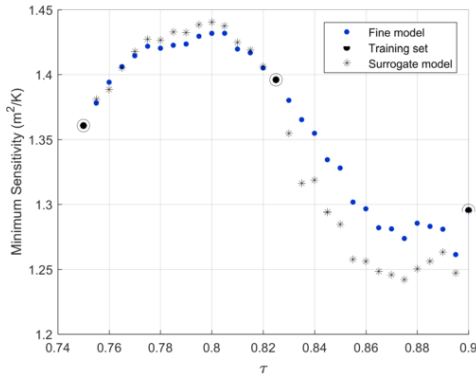
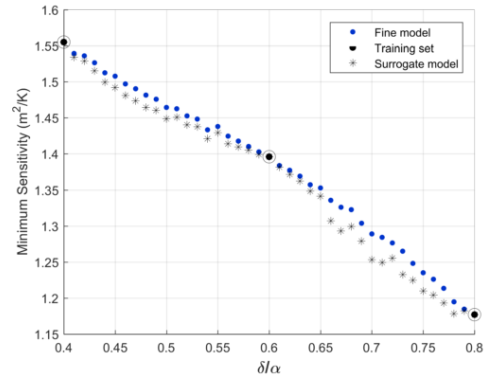
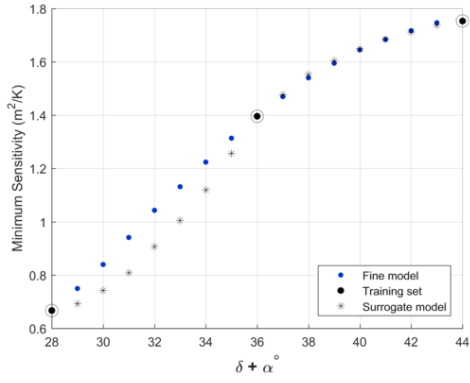
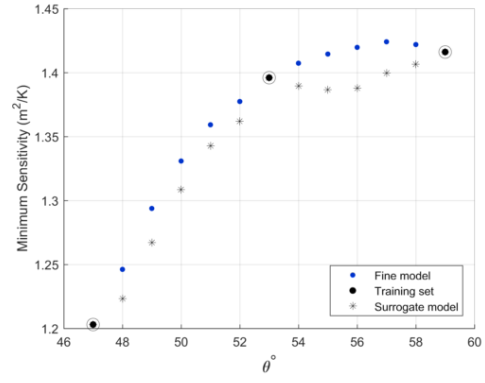
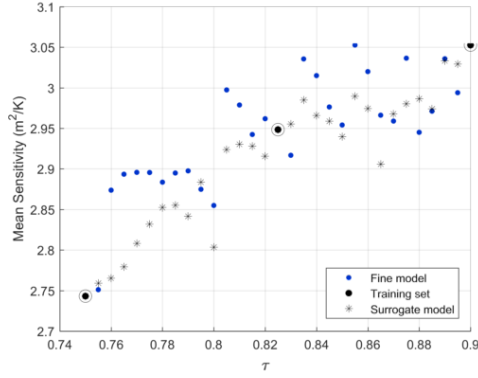
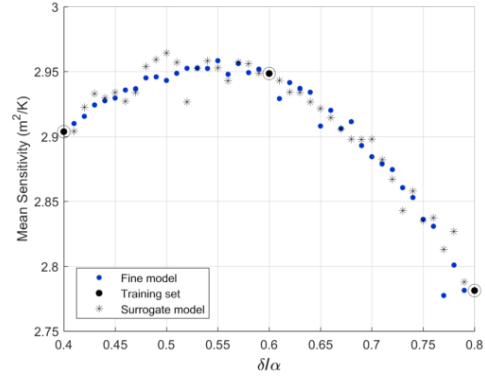
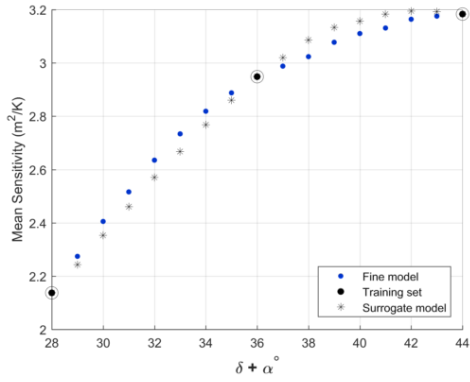
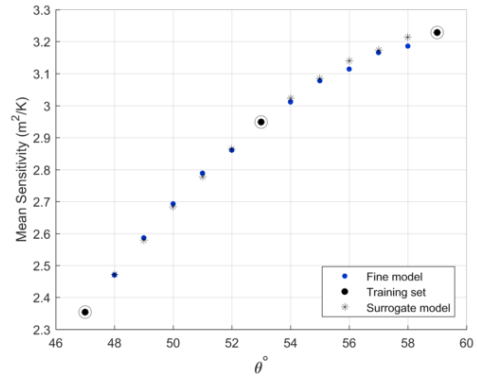
(a) Variations in τ .(b) Variations in δ/α .(c) Variations in $\delta + \alpha$.(d) Variations in θ .Figure A.4: Sensitivity surrogates for Model 2 of the objective function $U^{(c)}$.

Table A.2: Percentage errors for Model 2.

Model	Parameter	ARE [%]	MRE [%]
b)	τ	0.91	2.33
	δ/α	0.23	0.62
	$\delta + \alpha$	1.02	1.80
	θ	0.27	0.75
c)	τ	1.33	3.59
	δ/α	1.08	2.78
	$\delta + \alpha$	4.32	14.15
	θ	1.25	2.25

A.3 Model 3

(a) Variations in τ .(b) Variations in δ/α .(c) Variations in $\delta + \alpha$.(d) Variations in θ .Figure A.5: Sensitivity surrogates for Model 3 of the objective function $U^{(b)}$.

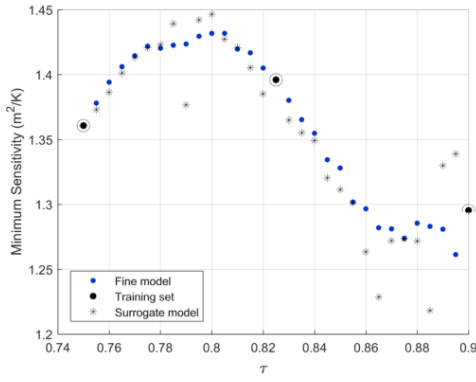
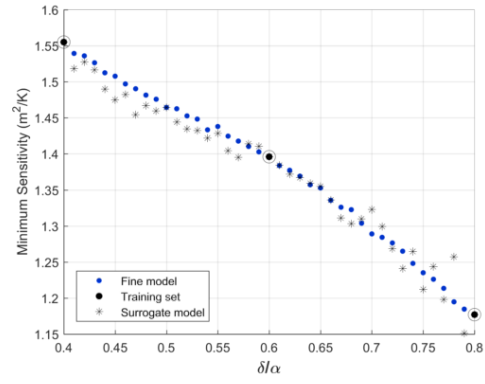
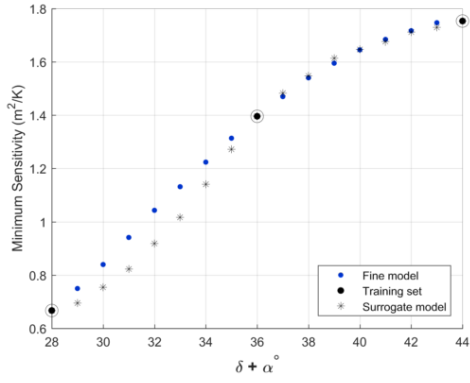
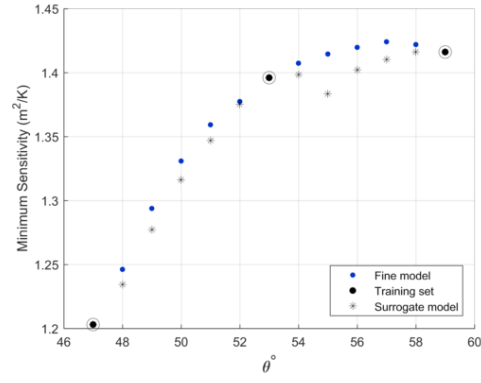
(a) Variations in τ .(b) Variations in δ/α .(c) Variations in $\delta + \alpha$.(d) Variations in θ .Figure A.6: Sensitivity surrogates for Model 3 of the objective function $U^{(c)}$.

Table A.3: Percentage errors for Model 3.

Model	Parameter	ARE [%]	MRE [%]
b)	τ	1.36	3.94
	δ/α	0.28	1.28
	$\delta + \alpha$	1.35	2.45
	θ	0.29	0.88
c)	τ	1.25	6.16
	δ/α	1.09	5.22
	$\delta + \alpha$	3.92	12.63
	θ	0.76	2.21

Bibliography

- [1] A. R. Taylor, “The Square Kilometre Array,” in *Proceedings of the International Astronomical Union*, vol. 8, no. S291, Aug 2012, pp. 337–341. [Online]. Available: <http://www.journals.cambridge.org>
- [2] P. E. Dewdney, W. Turner, R. Millenaar, R. McCool, J. Lazio, and T. J. Cornwell, “SKA1 system baseline design,” SKA, Tech. Rep. SKATEL-SKO-DD-001, March 2013. [Online]. Available: <http://www.skatelescope.org>
- [3] J. L. Jonas, “MeerKAT - The South African array with composite dishes and wide-band single pixel feeds,” *Proceedings of the IEEE*, vol. 97, no. 8, pp. 1522–1530, Aug 2009.
- [4] I. P. Theron, R. Lehmensiek, and D. I. L. de Villiers, “The design of the MeerKAT dish optics,” in *2012 International Conference on Electromagnetics in Advanced Applications*, Sept 2012, pp. 539–542.
- [5] P. G. Wiid and H. C. Reader, “Towards electromagnetic characterization of MeerKAT Telescope,” in *2014 XXXIth URSI General Assembly and Scientific Symposium (URSI GASS)*, Aug 2014, pp. 1–4.
- [6] R. Lehmensiek and I. P. Theron, “The design of the MeerKAT L-band feed,” in *2012 International Conference on Electromagnetics in Advanced Applications*, Sept 2012, pp. 321–324.
- [7] —, “Minimizing the MeerKAT system noise temperature,” in *2014 XXXIth URSI General Assembly and Scientific Symposium (URSI GASS)*, Aug 2014, pp. 1–4.
- [8] R. Olsson, P. S. Kildal, and S. Weinreb, “The eleven antenna: a compact low-profile decade bandwidth dual polarized feed for reflector antennas,” *IEEE Transactions on Antennas and Propagation*, vol. 54, no. 2, pp. 368–375, Feb 2006.
- [9] A. H. Akgiray, “New technologies driving decade-bandwidth radio astronomy: quad-ridged flared horn and compound-semiconductor LNAs,” Ph.D. dissertation, California Institute of Technology (Caltech), 2013.
- [10] G. Engargiola, “Non-planar log-periodic antenna feed for integration with a cryogenic microwave amplifier,” in *IEEE Antennas and Propagation Society International Symposium*, vol. 4, 2002, pp. 140–143.

- [11] G. C. Medellín, “Non-planar quasi-self-complementary ultra-wideband feed antenna,” *IEEE Transactions on Antennas and Propagation*, vol. 59, no. 6, pp. 1935–1944, June 2011.
- [12] R. Gawande and R. Bradley, “Towards an ultra wideband low noise active sinusoidal feed for next generation radio telescopes,” *IEEE Transactions on Antennas and Propagation*, vol. 59, no. 6, pp. 1945–1953, June 2011.
- [13] J. Yang, M. Pantaleev, P. S. Kildal, B. Klein, L. Helldner, and H. Raza, “Review of recent developments of the eleven feed for future decade bandwidth radio telescopes,” in *2011 XXXth URSI General Assembly and Scientific Symposium*, Aug 2011, pp. 1–4.
- [14] B. Billade, J. Flygare, M. Dahlgren, B. Wästberg, and M. Pantaleev, “A wide-band feed system for SKA band 1 covering frequencies from 350 - 1050 MHz,” in *2016 10th European Conference on Antennas and Propagation (EuCAP)*, April 2016, pp. 1–3.
- [15] E. K. Miller, “Model-based parameter estimation in electromagnetics,” *IEEE Antennas and Propagation Magazine*, vol. 40, no. 1, pp. 42–52, February 1998.
- [16] D. H. Werner and R. J. Allard, “Creating accurate multivariate rational interpolation models of microwave circuits by using efficient adaptive sampling to minimize the number of computational electromagnetic analyses,” *IEEE Transactions on Antennas and Propagation*, vol. 48, no. 3, pp. 383–392, March 2000.
- [17] R. Lehmensiek and P. Meyer, “Creating accurate multivariate rational interpolation models of microwave circuits by using efficient adaptive sampling to minimize the number of computational electromagnetic analyses,” *IEEE Transactions on Microwave Theory and Techniques*, vol. 49, no. 8, pp. 1419–1430, August 2001.
- [18] C. A. Balanis, *Antenna Theory: Analysis and Design*, 3rd ed. John Wiley & Sons, Inc., 2005, ch. 15.
- [19] C. Granet, “Designing classical offset cassegrain or gregorian dual-reflector antennas from combinations of prescribed geometric parameters,” *IEEE Antennas and Propagation Magazine*, vol. 44, no. 3, pp. 114–123, Jun 2002.
- [20] Y. Mizugutch, M. Akagawa, and H. Yokoi, “Offset dual reflector antenna,” in *1976 Antennas and Propagation Society International Symposium*, vol. 14, Oct 1976, pp. 2–5.
- [21] R. Collin, “Aperture efficiency for paraboloidal reflectors,” *IEEE Transactions on Antennas and Propagation*, vol. 32, no. 9, pp. 997–1000, Sep 1984.
- [22] TICRA, “GRASP10,” 2015, Version 10.5.0. [Online]. Available: <http://www.ticra.com>

- [23] J. Yang, S. Pivnenko, and P. S. Kildal, "Comparison of two decade-bandwidth feeds for reflector antennas: The eleven antenna and quadridge horn," in *Proceedings of the Fourth European Conference on Antennas and Propagation*, April 2010, pp. 1–5.
- [24] P. S. Kildal, "Factorization of the feed efficiency of paraboloids and cassegrain antennas," *IEEE Transactions on Antennas and Propagation*, vol. 33, no. 8, pp. 903–908, Aug 1985.
- [25] P. S. Kildal and Z. Sipus, "Classification of rotationally symmetric antennas as types BOR0 and BOR1," *IEEE Antennas and Propagation Magazine*, vol. 37, no. 6, pp. 114–, Dec 1995.
- [26] A. Ludwig, "The definition of cross polarization," *IEEE Transactions on Antennas and Propagation*, vol. 21, no. 1, pp. 116–119, Jan 1973.
- [27] D. I. L. de Villiers, "Offset dual-reflector antenna system efficiency predictions including subreflector diffraction," *IEEE Antennas and Wireless Propagation Letters*, vol. 10, pp. 947–950, 2011.
- [28] D. I. L. de Villiers and R. Lehmensiek, "Rapid calculation of antenna noise temperature in offset gregorian reflector systems," *IEEE Transactions on Antennas and Propagation*, vol. 63, no. 4, pp. 1564–1571, April 2015.
- [29] G. C. Medellín, "Antenna noise temperature calculation," in *SKA Memo 95*, July 2007, pp. 1–13.
- [30] W. A. Imbriale, "Faster antenna noise temperature calculations using a novel approximation technique," in *2010 IEEE Antennas and Propagation Society International Symposium*, July 2010, pp. 1–4.
- [31] D. I. L. de Villiers and R. Lehmensiek, "Noise temperature approximations for offset gregorian reflector systems," *IEICE Transactions on Communications*, vol. E101-B, no. 2, February 2018.
- [32] R. DuHamel, "Dual polarized sinuous antennas," April 1987, U.S. Patent 4 658 262.
- [33] T. Milligan, *Modern Antenna Design*. New York, NY, USA: McGraw-Hill, Inc., 1985.
- [34] V. Rumsey, "Frequency independent antennas," in *1958 IRE International Convention Record*, vol. 5, March 1957, pp. 114–118.
- [35] J. D. Kraus and R. J. Marhefka, *Antennas for All Applications*. Berlin, Germany: Springer, 2003.
- [36] J. Yang, M. Pantaleev, P. S. Kildal, and L. Helldner, "Design of Compact Dual-Polarized 1.2 - 10 GHz Eleven Feed for Decade Bandwidth Radio Telescopes," *IEEE Transactions on Antennas and Propagation*, vol. 60, no. 5, pp. 2210–2218, May 2012.

- [37] Y. Musiake, "Self-complementary antennas," *IEEE Antennas and Propagation Magazine*, vol. 34, no. 6, pp. 23–29, December 1992.
- [38] G. Deschamps, "Impedance properties of complementary multiterminal planar structures," *IRE Transactions on Antennas and Propagation*, vol. 7, no. 5, pp. 371–378, December 1959.
- [39] G. Engargiola and W. J. Welch, "Log-periodic antenna," January 2004, U.S. Patent 6 677 913 B2.
- [40] N. Mutoonkole, "Study of a wideband sinuous feed for reflector antenna applications," Master's thesis, Electronic Engineering, Stellenbosch University, December 2013.
- [41] Altair Development S.A. (Pty) Ltd, "FEKO," version 14.0.410. [Online]. Available: www.feko.info
- [42] N. Steenkamp, "Design of a wideband sinuous antenna for radio telescope applications," Master's thesis, Electronic Engineering, Stellenbosch University, December 2017.
- [43] J. W. Bandler, R. M. Biernacki, S. H. Chen, P. A. Grobelny, and R. H. Hemmers, "Space mapping technique for electromagnetic optimization," *IEEE Transactions on Microwave Theory and Techniques*, vol. 42, no. 12, pp. 2536–2544, Dec 1994.
- [44] M. H. Bakr, J. W. Bandler, N. Georgieva, and K. Madsen, "A hybrid aggressive space-mapping algorithm for EM optimization," *IEEE Transactions on Microwave Theory and Techniques*, vol. 47, no. 12, pp. 2440–2449, Dec 1999.
- [45] J. W. Bandler, R. M. Biernacki, and S. H. Chen, "Parameterization of arbitrary geometrical structures for automated electromagnetic optimization," in *1996 IEEE MTT-S International Microwave Symposium Digest*, vol. 2, June 1996, pp. 1059–1062 vol.2.
- [46] J. W. Bandler, R. M. Biernacki, S. H. Chen, R. H. Hemmers, and K. Madsen, "Electromagnetic optimization exploiting aggressive space mapping," *IEEE Transactions on Microwave Theory and Techniques*, vol. 43, no. 12, pp. 2874–2882, Dec 1995.
- [47] S. Koziel and S. Ogurtsov, *Antenna design by simulation-driven optimization*. Springer Publishing Company, Incorporated, 2014.
- [48] J. Zhu, J. W. Bandler, N. K. Nikolova, and S. Koziel, "Antenna optimization through space mapping," *IEEE Transactions on Antennas and Propagation*, vol. 55, no. 3, pp. 651–658, March 2007.
- [49] D. I. L. de Villiers and S. M. Koziel, "Multi-objective optimization of cassegrain reflector feeds using space mapping surrogate models," in *2015 IEEE-APS Topical Conference on Antennas and Propagation in Wireless Communications (APWC)*, Sept 2015, pp. 813–816.

- [50] D. I. L. de Villiers, M. V. Ivashina, and R. Maaskant, “Fast prediction of aperture efficiency and sidelobe levels in shaped reflector systems through model based output space mapping,” in *2015 9th European Conference on Antennas and Propagation (EuCAP)*, May 2015, pp. 1–5.
- [51] D. I. L. de Villiers, “Fast parametric modeling of radio astronomy reflector antenna noise temperature,” *IEEE Transactions on Antennas and Propagation*, vol. 64, no. 6, pp. 2522–2526, June 2016.
- [52] I. C. Dirk Gorissen, Eric Laermans and T. Dhaene, “Multiobjective global surrogate modeling, dealing with the 5-percent problem,” *Engineering with Computers*, vol. 26, no. 1, pp. 81–98, February 2010.
- [53] Y. Lin, “An efficient robust concept exploration method and sequential exploratory experimental design,” Ph.D. dissertation, Georgia Institute of Technology, 2004.
- [54] A. Cuyt, R. B. Lenin, S. Becuwe, and B. Verdonk, “Adaptive multivariate rational data fitting with applications in electromagnetics,” *IEEE Transactions on Microwave Theory and Techniques*, vol. 54, no. 5, pp. 2265–2274, May 2006.
- [55] The MathWorks, Inc, “MATLAB,” r2017a.
- [56] J. P. Berrut, “Rational functions for guaranteed and experimentally well-conditioned global interpolation,” *Computers and Mathematics with Applications*, vol. 15, no. 1, pp. 1–16, 1988.
- [57] J.-P. Berrut and L. Trefethen, “Barycentric Lagrange interpolation,” *SIAM Review*, vol. 46, no. 3, pp. 501–517, 2004.
- [58] H. T. Nguyen, A. Cuyt, and O. S. Celis, “Comonotone and coconvex rational interpolation and approximation,” *Numerical Algorithms*, vol. 58, no. 1, pp. 1–21, September 2011.
- [59] M. S. Floater and K. Hormann, “Barycentric rational interpolation with no poles and high rates of approximation,” *Numerische Mathematik*, vol. 107, no. 2, pp. 315–331, 2007.
- [60] E. R. Samuel, D. Deschrijver, L. Knockaert, T. Dhaene, and A. Cuyt, “Rational Modeling of Multivariate Multi-Fidelity Data,” in *VII European Congress on Computational Methods in Applied Sciences and Engineering*, June 2016, pp. 5–10.
- [61] A. Cuyt, R. Louw, C. Segers, and D. I. L. de Villiers, “Towards blended rational interpolation of multi-fidelity antenna data,” in *International Conference on Electromagnetics in Advanced Applications*, September 2017.
- [62] E. W. Cheney and D. R. Kincaid, *Numerical mathematics and computing*, 6th ed. Pacific Grove, CA, USA: Brooks/Cole Publishing Co., 2007.

- [63] D. G. Krige, “A statistical approach to some mine evaluations and allied problems at the witwatersrand,” Master’s thesis, University of Witwatersrand, Johannesburg, South Africa, 1951.
- [64] G. Matheron, “Principles of geostatistics,” *Economic Geology*, vol. 58, pp. 1246–1266, 1963.
- [65] P. D. I. Couckuyt, T. Dhaene, “ooDACE Toolbox: A Flexible Object-Oriented Kriging Implementation,” *Journal of Machine Learning Research*, vol. 15, pp. 3183–3186, Oct. 2014. [Online]. Available: <http://sumo.intec.ugent.be/ooDACE>
- [66] M. Stein, *Interpolation of Spatial Data: Some Theory for Kriging*. Springer-Verlag, 1999.